

**REPORT DOCUMENTATION PAGE****Form Approved**  
**OMB No. 0704-0188**

Public reporting burden for this collection of information is estimated to average 1 hour per response, including the time for reviewing instructions, searching data sources, gathering and maintaining the data needed, and completing and reviewing the collection of information. Send comments regarding this burden estimate or any other aspect of this collection of information, including suggestions for reducing this burden to Washington Headquarters Service, Directorate for Information Operations and Reports, 1215 Jefferson Davis Highway, Suite 1204, Arlington, VA 22202-4302, and to the Office of Management and Budget, Paperwork Reduction Project (0704-0188) Washington, DC 20503.

**PLEASE DO NOT RETURN YOUR FORM TO THE ABOVE ADDRESS.**

|   |                    |                                       |                                   |   |  |
|---|--------------------|---------------------------------------|-----------------------------------|---|--|
| <b>1. REPORT DATE (DD-MM-YYYY)</b><br>10/31/2014  |                    | <b>2. REPORT TYPE</b><br>Final Report |                                   | <b>3. DATES COVERED (From - To)</b><br>June 2011-July 2014    |  |
| <b>4. TITLE AND SUBTITLE</b><br>Development of Attribute Maps for Grain-Boundary Transport in Doped Alumina   |                    |                                       |                                   | <b>5a. CONTRACT NUMBER</b><br>N00014-11-1-0858                |  |
|   |                    |                                       |                                   | <b>5b. GRANT NUMBER</b><br>12.300                             |  |
|   |                    |                                       |                                   | <b>5c. PROGRAM ELEMENT NUMBER</b>                             |  |
| <b>6. AUTHOR(S)</b><br>Martin P Harmer - PI<br>Helen M Chan - CoPI<br>Jeffrey M Rickman - CoPI  |                    |                                       |                                   | <b>5d. PROJECT NUMBER</b><br>13PRO03350-00                    |  |
|   |                    |                                       |                                   | <b>5e. TASK NUMBER</b>  |  |
|   |                    |                                       |                                   | <b>5f. WORK UNIT NUMBER</b>                                   |  |
| <b>7. PERFORMING ORGANIZATION NAME(S) AND ADDRESS(ES)</b><br>Lehigh University<br>Office of Research and Sponsored Programs<br>526 Brodhead Avenue<br>Bethlehem, PA 18015-3008  |                    |                                       |                                   | <b>8. PERFORMING ORGANIZATION REPORT NUMBER</b>               |  |
| <b>9. SPONSORING/MONITORING AGENCY NAME(S) AND ADDRESS(ES)</b><br>Office of Naval Research<br>875 North Randolph Street<br>Arlington, VA 22203-1995   |                    |                                       |                                   | <b>10. SPONSOR/MONITOR'S ACRONYM(S)</b><br>DOD Navy Arlington |  |
|   |                    |                                       |                                   | <b>11. SPONSORING/MONITORING AGENCY REPORT NUMBER</b>         |  |
| <b>12. DISTRIBUTION AVAILABILITY STATEMENT</b><br>"Approved for Public Release; Distribution is Unlimited."   |                    |                                       |                                   |   |  |
| <b>13. SUPPLEMENTARY NOTES</b>  |                    |                                       |                                   |   |  |
| <b>14. ABSTRACT</b><br>In this work we investigate the effect of doping levels of HfO2 on oxygen grain boundary transport in alumina in order to elucidate the mechanisms for anionic boundary diffusion. In particular, we employ a novel system comprising doped alumina with a dispersion of Ni markers particles, with the oxidation of the latter highlighting oxygen penetration in a sample. By varying the Hf4+ concentration we explore the dependence of the oxidation rate, and thereby the diffusivity, on dopant concentration to infer diffusion mechanisms. We find two diffusive regimes, the first for small dopant concentration in which the boundary diffusivity decreases with dopant concentration and the second for larger concentrations in which the diffusivity is relatively independent of dopant concentration. This first regime is found to be consistent with site-blocking models by comparison with simulation studies in idealized systems. We also investigate the temperature dependence of the oxidation rate to extract an activation energy for diffusion and to identify any deviation from classical Arrhenius behavior. From this analysis we find evidence for a complexion transition in this system. |                    |                                       |                                   |   |  |
| <b>15. SUBJECT TERMS</b>  |                    |                                       |                                   |   |  |
| <b>16. SECURITY CLASSIFICATION OF:</b>  |                    |                                       | <b>17. LIMITATION OF ABSTRACT</b> | <b>18. NUMBER OF PAGES</b>                                    | <b>19a. NAME OF RESPONSIBLE PERSON</b><br>Martin P. Harmer       |
| <b>a. REPORT</b>  | <b>b. ABSTRACT</b> | <b>c. THIS PAGE</b>                   |                                   |   | <b>19b. TELEPHONE NUMBER (include area code)</b><br>610-758-4227 |

## INSTRUCTIONS FOR COMPLETING SF 298

**1. REPORT DATE.** Full publication date, including day, month, if available. Must cite at least the year and be Year 2000 compliant, e.g., 30-06-1998; xx-08-1998; xx-xx-1998.

**2. REPORT TYPE.** State the type of report, such as final, technical, interim, memorandum, master's thesis, progress, quarterly, research, special, group study, etc.

**3. DATES COVERED.** Indicate the time during which the work was performed and the report was written, e.g., Jun 1997 - Jun 1998; 1-10 Jun 1996; May - Nov 1998; Nov 1998.

**4. TITLE.** Enter title and subtitle with volume number and part number, if applicable. On classified documents, enter the title classification in parentheses.

**5a. CONTRACT NUMBER.** Enter all contract numbers as they appear in the report, e.g. F33615-86-C-5169.

**5b. GRANT NUMBER.** Enter all grant numbers as they appear in the report, e.g. 1F665702D1257.

**5c. PROGRAM ELEMENT NUMBER.** Enter all program element numbers as they appear in the report, e.g. AFOSR-82-1234.

**5d. PROJECT NUMBER.** Enter all project numbers as they appear in the report, e.g. 1F665702D1257; ILIR.

**5e. TASK NUMBER.** Enter all task numbers as they appear in the report, e.g. 05; RF0330201; T4112.

**5f. WORK UNIT NUMBER.** Enter all work unit numbers as they appear in the report, e.g. 001; AFAPL30480105.

**6. AUTHOR(S).** Enter name(s) of person(s) responsible for writing the report, performing the research, or credited with the content of the report. The form of entry is the last name, first name, middle initial, and additional qualifiers separated by commas, e.g. Smith, Richard, Jr.

**7. PERFORMING ORGANIZATION NAME(S) AND ADDRESS(ES).** Self-explanatory.

**8. PERFORMING ORGANIZATION REPORT NUMBER.** Enter all unique alphanumeric report numbers assigned by the performing organization, e.g. BRL-1234; AFWL-TR-85-4017-Vol-21-PT-2.

**9. SPONSORING/MONITORS AGENCY NAME(S) AND ADDRESS(ES).** Enter the name and address of the organization(s) financially responsible for and monitoring the work.

**10. SPONSOR/MONITOR'S ACRONYM(S).** Enter, if available, e.g. BRL, ARDEC, NADC.

**11. SPONSOR/MONITOR'S REPORT NUMBER(S).** Enter report number as assigned by the sponsoring/ monitoring agency, if available, e.g. BRL-TR-829; -215.

**12. DISTRIBUTION/AVAILABILITY STATEMENT.** Use agency-mandated availability statements to indicate the public availability or distribution limitations of the report. If additional limitations/restrictions or special markings are indicated, follow agency authorization procedures, e.g. RD/FRD, PROPIN, ITAR, etc. Include copyright information.

**13. SUPPLEMENTARY NOTES.** Enter information not included elsewhere such as: prepared in cooperation with; translation of; report supersedes; old edition number, etc.

**14. ABSTRACT.** A brief (approximately 200 words) factual summary of the most significant information.

**15. SUBJECT TERMS.** Key words or phrases identifying major concepts in the report.

**16. SECURITY CLASSIFICATION.** Enter security classification in accordance with security classification regulations, e.g. U, C, S, etc. If this form contains classified information, stamp classification level on the top and bottom of this page.

**17. LIMITATION OF ABSTRACT.** This block must be completed to assign a distribution limitation to the abstract. Enter UU (Unclassified Unlimited) or SAR (Same as Report). An entry in this block is necessary if the abstract is to be limited.

**Role of  $\text{Hf}^{4+}$  Doping on Oxygen Grain Boundary Diffusion in Alumina**

by

**Qian Wu**

A Dissertation

Presented to the Graduate and Research Committee

of Lehigh University

in Candidacy for the Degree of

**DOCTORATE OF PHILOSOPHY**

in

Materials Science & Engineering

Lehigh University

September 2014

20141110097

© 2014 Copyright  
Qian Wu

Approved and recommended for acceptance as a dissertation in partial fulfillment of the requirements for the degree of Doctor of Philosophy.

---

Date

---

Dissertation Director

---

Accepted Date

Committee:

---

Martin P. Harmer

---

Helen. M. Chan

---

Jeffery. M. Rickman

---

Edmund Webb III

Dedicated to

*Jinjiang Wu, Yihua Weng and Xinyun Lu*

## *Acknowledgements*

First, I would like to express my great appreciations to my advisors and committee member, Prof. Chan, Prof. Harmer, Prof. Rickman and Prof. Webb for their great help on the way to my Ph.D. Especially, I want to thank Prof. Chan, Prof. Harmer and Prof. Rickman for their continuous guidance, patience and encouragement through my research. I really appreciated and enjoyed working with all of you, which bring me into this interesting ceramic world and inspire me think both practically and philosophically. It reminds of an old Chinese saying that one-time teacher, lifetime credit a parent deserves. As for seven years, I would like to say; thanks again for your understanding and support of all the work and “trouble” I have done in Lehigh (Research, TA, Volunteer, etc).

Special thanks to Dr. Zhiyang Yu, who greatly help me with all the high-resolution electron microscopy utilized in my research and for useful discussion. Moreover, as a close friend and roommate, his accompany made my stay in Lehigh so wonderful.

During my stay in Lehigh, there are so many people helping and supporting me. Thanks Mr. William Mushock for all the SEM work and sharing basketball experience with me. Thanks Dr. Robert Keyse for all the TEM work, especially being patient during my training and provide great help during my job application. Thanks Sam. Lawrence and Arlan Benscoter teach me everything I need to know about metallography and never complain about the trouble I created. Thanks Suxing Wu and Gene Kozma fixing the furnace that I can keep my experiment running all the time. Many thanks to Sue Stelter,

whom I considered as my American Mom, always remind me of eating vegetables and become my American-life-Wikipedia. Thanks to Katrina Kraft to maintain my documents valid and never complain about the complicated case I bring to her. Thanks Gene Lucadamo to introduce me working in the consulting project and being the only one enjoy trying the durian. Thanks to Andrea Harmer to provide me great opportunity to teach middle school kids nanotechnology and I really enjoyed it. Thanks to Marie Ann for her creative idea in my cermographic contest. Thanks to Deanne Hoenscheid, Xiaoli Zhao, Maxine Mattie, Anne Marie Lobley, Janie Carlin and Lisa Arechiga for reminding me different deadlines and helping me with all the details related to my graduate studies in Lehigh. With all these support from the department staffs, I feel warmth and happiness especially as an international student.

Moreover, many thanks should to given to my previous and current group members. It is my great pleasure to talk and work with all of you: Shen Dillon, Animesh Kundu, Sreya Dutta, Patrick Cantwell, James Teevan, Jae Jin Kim, Donald Carpenter, Gerge Ferko, Yan Wang, Michael Kracum, Denise Yin, Abigail Lawrence, Chris Marvel, Qin Gao and Stephanie Bojarski (Carnegie Mellon University). And I also benefit a lot from current and previous fellow graduate students including: Mark Mclean, Jeffrey Farren, Kylan McQuaig, Daniel Bechetti, Andrew Stockdale, Brett Lesiter, Andrew Thome, J.C. Sabol, Anthony Ventura, Austin Wade, Donghui Zhao, Shaojie Wang, Wanjun Cao, Weihao Weng, Qian He, Kai Song, Wu Zhou, Li Lv, Bu Wang, Chao Zhao, Yilin Chen, Ling Ju, Fiona Cui. Special thanks should be given to Huikai Cheng and Shuailei Ma for their consistent help from the beginning of my research to final job interview opportunities.



Moreover, with the support for all my officemate, the journey to the Ph.D becomes more joyful. Thanks Binay Patel, Charles McLaren, Kevin Anderson, Onthida Kosasang, Chatree Saiyasombat, Mayhar Mohebimoghadam, and Adam Stone for creating office golf/basketball, learning different language and making fun with each other. The traditional of being cool in this office should be maintained.

Most of all, I would like to thank my parents and wife for their consistent support and encouragement during my study. Even far away in the distance, I can strongly feel their love and caring. And finally, the financial supports from the office of naval research are gratefully acknowledged.

## *Table of Contents*

|   |           |
|---|-----------|
| Certification of Approval.....  | iii       |
| Acknowledgments.....  | v         |
| Table of Contents.....  | viii      |
| List of Figures.....  | xi        |
| List of Tables.....   | xviii     |
| Abstract.....   | 1         |
| <b>Chapter 1. Background</b>  | <b>3</b>  |
| 1.1 The Growth of Alumina Scales.....   | 3         |
| 1.2 The Effect of Reactive Elements Additions on Growth of Alumina Scales           | 11        |
| 1.2.1 Studies on Hafnium's Effect.....  | 11        |
| 1.2.2 Proposed Mechanisms.....  | 20        |
| <b>Chapter 2. Grain Boundary Diffusion Studies in Polycrystalline Alumina</b>       | <b>22</b> |
| 2.1 Theoretical Background of Grain Boundary Diffusion in Polycrystals.....         | 23        |
| 2.1.1 Diffusion Kinetics in Polycrystals.....                                       | 23        |
| 2.1.2 Mathematical Solution in the Type B Regime.....                               | 25        |
| 2.2 Experimental Method of Obtaining Grain Boundary Diffusion in Polycrystals.....  | 29        |
| 2.2.1 Diffusivity Calculation from Secondary Ion Mass Spectrometry Analysis.....    | 29        |
| 2.2.2 Diffusivity Calculation from Gravimetrically Determined Growth Rate Data..... | 32        |
| 2.2.3 Studies of Grain Boundary Diffusion by Other Groups.....                      | 34        |
| 2.3 Grain Boundary Complexions.....   | 40        |

|   |           |
|---|-----------|
| 2.3.1 Definitions of Grain Boundary Complexions.....              | 40        |
| 2.3.2 Characterization of Complexions.....                        | 47        |
| 2.3.2.1. Direct Characterization of Complexions by using TEM..... | 47        |
| 2.3.2.2. Indirect Characterization of Complexions by using AFM... | 52        |
| <b>Chapter 3. Statement of Purpose</b>                            | <b>56</b> |
| <b>Chapter 4. Experimental Procedure</b>                          | <b>57</b> |
| 4.1 Powder Processing.....  | 57        |
| 4.1.1 HfO <sub>2</sub> -doped Alumina.....                        | 59        |
| 4.1.2 Other Alumina/Ni Composites.....                            | 60        |
| 4.2 Hot-pressing/ Spark Plasma Sintering.....                     | 60        |
| 4.3 Sample-cutting.....   | 65        |
| 4.4 Sample-polishing.....   | 65        |
| 4.5 Sample-cleaning.....  | 67        |
| 4.6 Oxidation of Samples.....                                     | 67        |
| 4.7 TEM Sample Preparation.....                                   | 68        |
| 4.8 Grain Size Measurement.....                                   | 73        |
| 4.9 Diffusion Depth Measurement.....                              | 75        |
| 4.10 Texture Analysis.....  | 75        |
| 4.11 Grain Boundary Characterization by Using TEM.....            | 76        |
| 4.12 Thermal Grooving Measurement by Using AFM.....               | 76        |
| <b>Chapter 5. Results and Discussions</b>                         | <b>80</b> |
| 5.1 The Effect of HfO <sub>2</sub> Doping Concentrations.....     | 80        |

|  |            |
|--|------------|
| 5.1.1 Microstructure.....  | 80         |
| 5.1.2 Oxidation Kinetics.....  | 87         |
| 5.2 The Effect of Oxidation Temperature.....   | 98         |
| 5.2.1 Microstructure.....  | 98         |
| 5.2.2 Oxidation Kinetics.....  | 99         |
| 5.2.3 Grain Boundary Characterization by HAADF-STEM.....   | 105        |
| 5.2.3.1 Grain Boundaries Oxidized at 1400°C.....   | 105        |
| 5.2.3.2 Grain Boundaries Oxidized at 1250°C.....   | 116        |
| 5.2.3.3 Grain Boundaries Oxidized at 1150°C.....   | 119        |
| 5.2.3.4 Grain Boundaries for As-Hot Pressed.....   | 120        |
| 5.3 Discussions.....   | 124        |
| 5.3.1 The Effect of HfO <sub>2</sub> Doping Levels.....  | 124        |
| 5.3.2 The Effect of Nickel.....  | 132        |
| 5.3.3 The Effect of Oxidizing Temperature.....   | 134        |
| <b>Chapter 6. Conclusions and Suggested Future Work</b>  | <b>146</b> |
| <b>Chapter 7. Contributions</b>  | <b>149</b> |
| <b>Appendices</b>  | <b>150</b> |
| <b>Appendix A. Calculating The Effect of Nickel Outward Diffusion on Oxidation Penetration Depth</b> | <b>150</b> |
| <b>Appendix B. Hf and La-codoped sample</b>  | <b>152</b> |
| <b>Bibliography</b>  | <b>160</b> |
| <b>Vita</b>  | <b>171</b> |

## *List of Figures*

|  |    |
|--|----|
| Figure 1.1: Normal alloying elements presented in Ni-based superalloys [84].....   | 8  |
| Figure 1.2: Cross section view of thermal barrier coating system [3].....  | 9  |
| Figure 1.3: Schematic illustration of the experimental technique used to observe the outward growth due to Al grain boundary diffusion: a) typical scale structure after oxidation b) the outer scale layer is removed by polishing c) re-oxidation produces oxide ridges of different size depending on the thickness of the remaining scale. [18]..... | 10 |
| Figure 1.4: Isothermal weight gains for various alloys doped with REs oxidized at 1200°C plotted as a function of square root of time to show the parabolic rate growth kinetics. [74].....  | 17 |
| Figure 1.5: Average parabolic rate constants for various commercial and laboratory FeCrAl doped with different REs oxidized at 1200°C. [78].....   | 18 |
| Figure 1.6: Optical microscopy of polished cross-sections of the alumina scale formed on various castings of NiAl+Hf after 10, 100h cycles at 1200°C. [77].....  | 19 |
| Figure 2.1: Schematic illustration of types A, B and C diffusion kinetics in a single crystal material containing uniformly spaced planar fast diffusion paths.....  | 27 |
| Figure 2.2: Schematic plot for Fisher's model [109].....   | 28 |
| Figure 2.3: $^{18}\text{O}$ concentration profile plot against depth x (cm) (68).....  | 31 |
| Figure 2.4: Oxygen grain boundary diffusion in $\alpha\text{-Al}_2\text{O}_3$ summarized by Heuer. [71].....   | 38 |
| Figure 2.5: $^{18}\text{O}$ TOF-SIMS image with ~100nm spatial resolution for fully dense sintered $\text{Al}_2\text{O}_3$ polycrystal with about 10 $\mu\text{m}$ grain size. The contrast is due to  | 39 |

|  |    |
|--|----|
| differences in grain boundary diffusivities. [114].....  |    |
| Figure 2.6: Grain boundary mobility as a function of inverse temperature for undoped and doped alumina [32].....   | 43 |
| Figure 2.7: High angle annular dark-field scanning transmission electron micrographs of six discrete Dillon-Harmer complexions in undoped and doped alumina (CaO, MgO, SiO <sub>2</sub> , Nd <sub>2</sub> O <sub>3</sub> ) (a) Clean. (b) Monolayer. (c) Bilayer. (d) Trilayer. (e) Nanolayer. (f) Wetting. [32].....  | 44 |
| Figure 2.8: STEM HAADF images show 2 layers of Bi absorbed along the general GBs of a Ni polycrystal quenched from 700°C. (C) Weakly bonded Bi atoms could cause the boundaries to easily fracture between layers and thus embrittle the material. Presumably, decohesion of this GB occurred during TEM specimen preparation. (D) A bilayer interfacial phase similar character was observed in specimens quenched from 1100°C. [54]..... | 45 |
| Figure 2.9: Schematic diagrams showing different types of complexion transitions and different ways of categorizing complexions. [46].....   | 46 |
| Figure 2.10: Schematic illustrations of HAADF-STEM imaging. [53] .....   | 50 |
| Figure 2.11: Sketch of the basic principle for focal series imaging. [61] .....  | 51 |
| Figure 2.12: Section showing profile of ideal thermal groove (vertical exaggeration~5X) [35] .....   | 54 |
| Figure 2.13: Cumulative distribution of dihedral angles in neodymia-doped alumina annealed at 1400°C with normal (monolayer complexions) and abnormal (bilayer complexions) grain boundaries. [64, 65].....  | 55 |
| Figure 4.1: Basic configuration of a Spark Plasma Sintering (SPS) Machine [49].  | 63 |
| Figure 4.2: Spark Plasma Sintering (SPS) Model 10-4 used in the current study [50].....  | 64 |

|  |    |
|--|----|
| Figure 4.3: FIB image at different steps: a) Pt layer deposition b) Trench on one side c) Trench on the other side d) Edges cut off and small connections with the bulk sample remained [51].....  | 70 |
| Figure 4.4: Alumina sample lifted out by manipulator before attached to the middle column of the Mo grid .....   | 71 |
| Figure 4.5: Fischione's Model 1040 NanoMill TEM specimen preparation system [52].....  | 72 |
| Figure 4.6: Free surface of 500ppm HfO <sub>2</sub> doped alumina/Ni oxidized at 1400 for 5h.....  | 74 |
| Figure 4.7: AFM image showing surface topography of undoped alumina sample annealed for 3 h at 1500°C (LHS). Depth profile for selected grain boundary section as indicated by green arrow (RHS). .....  | 79 |
| Figure 5.1: Scanning electron microscope showing the cross section of the 500ppm HfO <sub>2</sub> -doped Alumina with 0.5vol%Ni after oxidation for 60hrs at 1400°C .....  | 83 |
| Figure 5.2: Scanning electron microscope showing representative features of the oxidized region of HfO <sub>2</sub> -doped Ni/ Alumina oxidized at 1400°C for various time with a doping level of a) 100ppm for 5h b) 200ppm for 20h c) 300ppm for 5h d) 500ppm for 5h e) 2000ppm for 20h .....  | 84 |
| Figure 5.3: Free surface comparison between a) 500ppm Hf doped oxidized at 1300°C for 24h with an average grain size 3.6µm b) undoped alumina oxidized at 1300°C for 6h with an average grain size 1.9µm.....  | 85 |
| Figure 5.4: Graphs of the average of the square of the thickness of the oxidized layer, $x^2$ , versus annealing time, $t$ , for HfO <sub>2</sub> – doped Ni/Alumina oxidized at 1400°C with various doping levels. The results are averaged over 10 areas, with the error bars representing the standard deviation in $x^2$ . The straight lines are least-square fits to the data for each doping content..... | 92 |

Figure 5.5: Graphs of the ratio after grain size correction ( $k_{\text{undoped}}^c/k_{\text{doped}}^c$ ) as a 94  
function of doping levels. Two regions can be identified clearly. The solid straight  
line is least-square fit to the doping levels including undoped, 100ppm, 200ppm.  
(Region I) The dashed straight line is an average of the value for doping levels  
higher than 200ppm. (Region II) .....

Figure 5.6: Plot of the corrected ratio ( $k_{\text{doped}}^c/k_{\text{undoped}}^c$ ) as a function of grain 95  
boundary coverage ratio. The solid straight line is least-square fit to the doping  
levels including undoped, 100ppm, 200ppm, and 300ppm.....

Figure 5.7: The logarithm of corrected rate constant,  $k_c$ , plotted versus reciprocal 97  
temperature for undoped [15], 100ppm and 500ppm HfO<sub>2</sub> - doped alumina  
oxidized from 1250°C to 1400°C.....

Figure 5.8: Graphs of the average of the square of the thickness of the oxidized 102  
layer,  $x^2$ , versus annealing time,  $t$ , for 500ppm HfO<sub>2</sub> – doped Ni/Alumina oxidized  
at a) 1320 ~1400°C b) 1150 ~1250°C. The results are averaged over 10 areas,  
with the error bars representing the standard deviation in  $x^2$ . The straight lines are  
least-square fits to the data at each temperature.....

Figure 5.9: The logarithm of corrected rate constant,  $k_c$ , plotted versus reciprocal 104  
temperature for 500ppm HfO<sub>2</sub> - doped alumina oxidized from 1150°C to 1400°C.  
The dashed line is least-square fit including three temperatures: 1250°C, 1320°C,  
and 1400°C. The dashed line was extended to show the deviation of the 1150°C  
data point. The error bar has calculated based on the method described before.....

Figure 5.10: Low magnification HAADF image of 500ppm Hf-doped sample 109  
oxidized at 1400°C extracted from oxidized region is shown on the left. EDX  
analysis collected for grain boundary and grain respectively are shown on the  
right. Void, HfO<sub>2</sub> second phase particles and nickel aluminate spinel can be  
observed as indicated by the arrow point to the left.....

Figure 5.11: Cs-corrected HAADF-STEM image of 500ppm HfO<sub>2</sub>-doped GB 110



|  |     |
|--|-----|
| oxidized at 1400°C with the left crystal orientated in the $[0\ 0\ 0\ 1]$ direction.....   |     |
| Figure 5.12: Focal series images of the grain boundary in Figure 5.11.....   | 111 |
| Figure 5.13 A schematic model shows the multi-dimensional steps of single-atom-height decorated with Hf. Note that the interval of faceting in both dimensions has been reduced for easier presentation.....   | 112 |
| Figure 5.14 (a,b) Side view and plane view atomic model for HAADF simulation to interpret the contrast formation of lower contrast Hf layer. For each layer, the supercells are shown in one unit cell (1.3nm) and the symbol, 'X' denotes the supercells will be extended by the number after the symbol in the image calculation. (c) Simulated HAADF-STEM images reproduce the image contrast observed in the experiment..... | 113 |
| Figure 5.15 HAADF-STEM images of grain boundaries oxidized at 1400°C within the oxidized region (a) blue dotted line shows facets parallel to $\{2\ -1\ -1\ 0\}$ (b) zone axis and yellow dotted line shows facets parallel to $\{1\ 0\ -1\ 2\}$ .....   | 114 |
| Figure 5.16 HAADF-STEM images of grain boundaries oxidized at 1400°C outside the oxidized region and blue dotted line shows facets parallel to $\{2\ -1\ -1\ 0\}$ .....  | 115 |
| Figure 5.17 HAADF-STEM images of grain boundaries oxidized at 1250°C within the oxidized region. (a) Blue dotted line shows facets parallel to $\{2\ -1\ -1\ 0\}$ (b) Yellow dotted line shows facets parallel to $\{1\ 0\ -1\ 2\}$ .....  | 117 |
| Figure 5.18: HAADF-STEM images of grain boundaries oxidized at 1250°C outside the oxidized region. (a) Blue dotted line shows facets parallel to $\{2\ -1\ -1\ 0\}$ (b) Yellow dotted line shows facets parallel to $\{1\ 0\ -1\ 2\}$ .....  | 118 |
| Figure 5.19: HAADF-STEM images of grain boundaries oxidized at 1150°C within the oxidized region. (a) Blue dotted line shows long facets parallel to $\{2\ -1\ -1\ 0\}$ and green dotted line shows short facets parallel to $\{2\ -1\ -1\ 3\}$ (b) Blue dotted line shows part of the facets parallel to $\{2\ -1\ -1\ 0\}$ and red dotted line   | 121 |

shows the other parallel to  $\{0\ 0\ 0\ 6\}$  (c) Green dotted line shows the facets parallel to  $\{2\ -1\ -1\ 3\}$ .....

Figure 5.20: Pie Chart for percentage of plane that facets parallel to at each oxidation temperature is plotted. From Left to right, the samples are oxidized at 1150°C, 1250°C and 1400°C respectively. Blue portion stands for miscellaneous planes including  $\{0\ 0\ 0\ 6\}$  and  $\{2\ -1\ -1\ 3\}$ . Yellow and green portion stand for  $\{1\ 0\ -1\ 2\}$  and  $\{2\ -1\ -1\ 0\}$  respectively.....

Figure 5.21: HAADF-STEM images of grain boundaries as sintered at 1400°C. (a) Blue dotted line shows facets parallel to  $\{2\ -1\ -1\ 0\}$  (b) Yellow dotted line shows facets parallel to  $\{1\ 0\ -1\ 2\}$ .....

Figure 5.22: Diffusion coefficients  $D^*$  ( $C$ ,  $\alpha$ ) as a function of  $C/C_p$  for three different geometries: hexagonal obstacles of unit radius on the triangular lattice (HEX), point obstacles on the triangular lattice (TRI), and point obstacles on the square lattice (SQ).....

Figure 5.23: Reduced boundary mobility of 100 ppm of Zr doped alumina, indicating two regimes of growth; At temperatures  $<1550^\circ\text{C}$ , it is reduced as compared to undoped alumina, whereas it is higher than undoped alumina above  $1600^\circ\text{C}$ ; Zr-doped data courtesy: Shantanu Behera, PhD Dissertation, 2010, Lehigh University; Mg-doped and undoped data courtesy: Shen Dillon, PhD Dissertation, 2007, Lehigh University.....

Figure 5.24: Graphs of the Rate Constant Ratio as a function of temperature for (Left) 500ppm Hf doped samples. Two sets of data have been included in the plot besides the current work, which are Pint et al. [7, 42, 43] and Gleeson et al. [41] (Right) 500ppm Y doped samples. Three sets of data have been included in the plot, which are Cheng et al. [15], Pint et al. [7, 42] and Gleeson et al. [41].....

Figure 5.25: Influence of dopant on cumulative grain boundary dihedral angle.....

distribution in alumina: blue line is undoped alumina; red line is 500ppm HfO<sub>2</sub>-doped.....

Figure 5.26: Influence of dopant on cumulative grain boundary dihedral angle distribution in alumina: blue line is undoped alumina; purple line is 500ppm Y<sub>2</sub>O<sub>3</sub>-doped.....

Figure A.1: (Left) Free surface for 500ppm Hf doped oxidized at 1400°C for 5h (right) 8-bit image with white and black contrast created by ImageJ [32]

Figure B.1: Free surface of bilayer sample composed of 500 ppm La doped alumina bonded to 500ppm Hf-doped alumina. The sample was subjected to an oxidation heat-treatment of 5h at 1400 °C. The dashed lines designate the interfacial region where the density of spinel is lower. (SEM, secondary electron contrast).

Figure B.2 (LHS) Scanning electron microscope image showing the cross section of 500ppm Hf and 500ppm La co-doped alumina after oxidation for 60h at 1400°C (backscattered electron contrast) (RHS) Enlarged image of dotted box in Figure 1 showing Hf rich particles, nickel aluminate spinel and La hexaaluminates within the oxidation zone (backscattered electron contrast)

Figure B.3 Graph of the average of the square of the thickness of the oxidized layer,  $x$ , versus oxidation time  $t$  for different samples oxidized at the same temperature 1400°C, including 500ppm Hf doped, 500ppm La doped, 500ppm Hf and 500ppm La codoped. The results are averaged over 10 areas, with the error bars representing the standard deviation in  $x^2$ . The straight lines are least-squares fits to the data.

## *List of Tables*

|   |     |
|---|-----|
| Table 1.1 Effect of Reactive Element Addition on Oxidation Rates [1].....   | 16  |
| Table 2.1 Arrhenius parameters, $D_0$ and $Q$ , for diffusive processes in $\alpha$ - $\text{Al}_2\text{O}_3$ ( $D = D_0 \exp(-Q/RT)$ ) from [71].....  | 37  |
| Table 5.1: Summary of Grain Size for Samples with Different $\text{Hf}^{4+}$ Dopant Levels Oxidized at $1400^\circ\text{C}$ .....   | 87  |
| Table 5.2: Comparison between Values of the parabolic rate constants determined for all compositions of $\text{HfO}_2$ – doped alumina oxidized at $1400^\circ\text{C}$ . Data adapted from Cheng et al. [15] for undoped Alumina/Ni also included.....             | 94  |
| Table 5.3: Comparison between Values of the parabolic rate constants determined for 100ppm and 500ppm $\text{HfO}_2$ – doped alumina oxidized at three different temperatures. Average grain size $d$ for each sample is also included.....                         | 97  |
| Table 5.4. Summary of Average Grain Size for 500ppm $\text{HfO}_2$ -doped Alumina/Ni Oxidized at Different Temperatures.....  | 102 |
| Table 5.5. Comparison between Values of the parabolic rate constants determined for 500ppm $\text{HfO}_2$ – doped Alumina/Ni oxidized at different temperature. Rate constant and grain size data for undoped Alumina/Ni can be adapted from Cheng et al. [15]..... | 104 |
| Table 5.6. Comparison of values of activation energy derived from different transport-related experiments in alumina.....   | 132 |
| Table B.1 Comparison of values of the parabolic rate constants for different samples.....   |     |

## ***Abstract***

The growth of protective alumina scales in  $\text{Al}_2\text{O}_3$ -forming alloys can be affected by the addition of reactive elements, such as  $\text{Hf}^{4+}$ , which has been considered one of the most effective dopants to slow down the scale growth rate. While a number of theories concerning the “reactive element effect” have been proposed, a full explanation of this phenomenon is not yet available. The overall objective for this study was to conduct a systematic series of model experiments in order to elucidate the effect of  $\text{HfO}_2$  on oxygen grain boundary transport in alumina. The key questions to focus in the current work are: How do the doping levels of  $\text{HfO}_2$  / oxidizing temperature affect oxygen grain boundary diffusion in alumina?

First part of this work investigated the effect of doping levels of  $\text{HfO}_2$  on oxygen grain boundary transport in alumina, which contains uniformly distributed Ni metallic particles. The doping levels spanned the solubility limit ranging from 100ppm to 2000ppm. The plot of the ratio  $k_{\text{undoped}}/k_{\text{doped}}$  (grain-size corrected) as a function of dopant level clearly shows two behavior regimes: namely a regime I that encompasses doping levels below and near the solubility limit and a regime II where second-phase  $\text{HfO}_2$  particles were well present in the microstructure. A clearer understanding of the influence of  $\text{HfO}_2$  doping on the transport behavior can be achieved by plotting the data with respect to the fractional grain boundary coverage ( $f$ ), as opposed to overall  $\text{HfO}_2$  content. The linear relationship can be rationalized with a site-blocking model, in which the  $\text{Hf}^{4+}$  ions obstruct the diffusive paths at the grain boundary.

The second part of the work is focused on the temperature dependence of the oxidation kinetics in  $\text{HfO}_2$  doped  $\text{Al}_2\text{O}_3$ . The activation energy and rate constant ratio plot from our work and alloys studies indicated that multiple diffusion mechanisms might be operative at grain boundaries owing to boundary transitions that modify local structure and chemistry. Results of ARM characterization of samples oxidized at  $1150^\circ\text{C}$  have revealed that boundary structures that differ from those observed in samples oxidized at  $1250^\circ\text{C}$  and  $1400^\circ\text{C}$ . Specifically, new types of boundary structures are present at the lower temperature that are more atomic rough structure, and exhibit high energy facet planes such as  $\{0\ 0\ 0\ 6\}$  and  $\{2\ -1\ -1\ 3\}$  different from relative low energy facet plane such as  $\{2\ -1\ -1\ 0\}$  and  $\{1\ 0\ -1\ 2\}$  for samples oxidized at higher temperature. These high-energy facet planes maybe occupied with high Hf segregation level and resulted in a much better oxidation resistance. The current results highlight the significant role of complexion transition in the oxidation area, which is traditionally being neglected.

## ***Chapter 1. Background***

### ***1.1. The Growth of Alumina Scales***

Gas turbines, which are widely used in aircraft, marine and power transmission area, have progressed greatly over the last several decades based on extensive research efforts to increase the operating temperature of the engine and therefore, increase the efficiency of the engine with the development of internally cooled components and thermal barrier coatings. [2, 3, 84, 86] However, as the application temperature rises, oxidation resistance will be a primary degradation mode, especially for turbine blades, which experiences the most severe environment such rapid temperature transients, oxidizing gases, contaminants such as chlorides and sulphates.

Among various commercial alloys, Nickel-based superalloys are the widely used turbine blade materials with an exceptional combination of high temperature strength, toughness, and resistance to degradation in corrosive or oxidizing environments, which can tolerate temperature as high as 1200°C that is approximately 90% of the melting point of the material. [84, 87] Besides the FCC Nickel as the major superalloy constituent, there is a combination of five to ten other elements alloyed with nickel to achieve a significant improvement in properties such as creep, oxidation and so on, as listed in Figure 1.1.

In order to realize greater efficiency, the next generation of gas turbine systems will operated at increasingly higher temperature, which is even above the melting point of superalloys from which they are comprised. With the deposition of a multilayer and multicomponent thermal barrier coatings (TBCs), the turbine blades can survive up to 40,000 hours before failing. [3, 84, 85, 88] Figure 1.2 shows a typical cross section view of turbine blades with TBC coating. The topmost layer is typically a 6~8wt% yttria stabilized Zirconia (YSZ), which act mainly as a heat shield to provide major reduction in the surface temperature. ( $100^{\circ}\text{C} \sim 300^{\circ}\text{C}$ ) Moreover, YSZ has a lower density and well-matched thermal expansion coefficient with the underlying alloy, which resulted in a lighter weight and minimize the stress build-up during the thermal expansion mismatch. However, YSZ is transparent to oxygen diffusion due to its high oxygen vacancies and oxidation from underlying superalloys resulted in fast growing Ni-rich oxides, which are not thermodynamically stable with YSZ [86] and hence cause failure of the coating. Therefore, a bond coat alloy ( $\text{MCrAlY}$ ,  $\text{M}=\text{Ni, Co}$ ) is usually placed between YSZ and superalloys. During the service, oxidation of the bond coat results in the formation of thin alumina layer between the bond coat and YSZ, which can provide oxidation resistance by slowing further oxygen diffusion through this thermal grown alumina. And compared with other protective oxides such as  $\text{Cr}_2\text{O}_3$  or  $\text{SiO}_2$ , alumina is widely used due to its relative ease to form a continuous layer, its slow growth rate and long-term chemical stability since  $\text{Cr}_2\text{O}_3$  has volatility issues at temperature higher than  $800^{\circ}\text{C}$  and  $\text{SiO}_2$  has volatility issues with  $\text{H}_2\text{O}$ . [2] However, with the alumina growing thicker and thicker, various failure mechanisms could initiate such as stress-induced delamination of the thick alumina due to thermal



expansion mismatches and reduced interface adhesion between alumina and bond coat due to the presence of interfacial voids, which will expose the substrate alloys directly to oxidizing environment. [2, 3, 85, 89] Since there is no practical strategy for preventing the high-temperature oxidation, it is essential to reduce the alumina growth rate to maximize the use temperature and extend underlying superalloy's lifetime. Considering the growth of the alumina protective layer is a diffusion controlled-process, understanding the transport mechanisms of Al and O in the oxide layer will be essential.

Various methods have been used to elucidate the growth mechanism of this thermal grown alumina. One way to investigate the mechanism is by placing inner markers on the non-oxidized metal surface. After oxidation, the location of the inner markers could indicate the alumina is formed by either inward O diffusion or outward Al diffusion, or both. Ramanarayan et al. [90] used tiny droplets of Pt markers in FeCrAl alloys. The results showed that the Pt marker was placed at the gas-alumina interface, which strongly indicated that the growth mechanism is occurred by O inward diffusion. While results from Mrowec et al. [91] by using nano-size Au markers showed that the alumina was grown by simultaneously O inward and Al outward diffusion. Moreover, the reliability of these marker experiments has been questioned to have misleading results. In Young et al [92] study, Pt Markers remained on the surface of the NiAl alloys after oxidation at 900°C suggesting inward oxygen transport, while  $^{18}\text{O}$  tracer study in the same alloy showed the contribution of Al outward diffusion cannot be neglected.

Another way to study the growth mechanism of alumina scales is by using Secondary Ion Mass Spectrometry (SIMS) techniques combined with  $^{18}\text{O}$  tracer experiments. The basic principle can be described below: The alloys are first oxidized in the  $^{16}\text{O}$  atmosphere to form a thin layer of  $^{16}\text{O}$ -containing alumina scales. Then the alloy was oxidized again in an  $^{18}\text{O}$ -rich gas. By using SIMS, the depth profile of  $^{18}\text{O}$  concentrations as a function of locations through the alumina and alloy systems will give information on the alumina growth mechanism. Various transport mechanisms have been proposed by Reddy et al. [93] and Quadakkers et al. [94] based on the distribution of the isotopes. It is reasonable to speculate that four possible transport mechanisms from different  $^{18}\text{O}$  concentration profiles. If outward Al diffusion is the dominant mechanism, the  $^{18}\text{O}$ -containing alumina will be formed at the gas-oxide interface and the tracer concentration will be a step function. If inward O diffusion is the primary mechanism through pores or microcracks, then the  $^{18}\text{O}$ -containing oxide will be formed at the oxide-alloy interface and the tracer concentration will also be a step function. Moreover, if the alumina is mainly grown through grain boundary diffusion, most of the  $^{18}\text{O}$ -containing alumina will be formed at the oxide-alloy interface while minor amount will be formed at the gas- $^{16}\text{O}$ -containing oxide interface due to exchange of  $^{18}\text{O}$  with  $^{16}\text{O}$  at the grain boundaries. If the diffusion mechanism is a combination of outward Al and inward O grain boundary transport, the  $^{18}\text{O}$ -containing oxide will be formed at both gas-oxide and oxide-alloy interface. It should be pointed out that the dominant growth mechanisms could be changed by varying oxidation temperatures. Mitchell et al [95] found the Al outward diffusion is

the primary mechanism for NiAl oxidized at 1100°C, while the contribution of the O inward diffusion becomes more significant with increasing oxidation time and temperature. Similar trends have been observed by Young et al. [96] that NiAl oxidized at 900°C indicated a mainly Al outward diffusion, while increased inward O diffusion at 1150°C.

The third method is based on the microstructural evidence during the growth of alumina scales proposed by Tolpygo and Clarke. [18, 97] The outward Al diffusion can be analyzed by measuring the oxide ridges growing on the alumina surface, while the inward O diffusion was inferred from the columnar structure of the alumina grains. The schematic illustration of the experiments is shown in the Figure 1.3. The basic procedures can be described below: The alloy was first oxidized to form a thin and adherent alumina layer. Then the top surface was mechanically polished to remove the oxide layer at a small angle to the sample surface. After oxidation again, the surface morphology can be analyzed by using SEM. The newly formed oxide ridges at the alumina grain boundaries on the top surface were grown mainly by Al outward grain boundary diffusion. By knowing the outward diffusion flux, the thickening of the oxide by inward O diffusion can be obtained from weight-gain measurements. Therefore, the outward Al flux can be quantified as a function of oxide thickness and information about the ratio of outward diffusion of Al to inward diffusion of O can be obtained.

| IIA | IIIA        | IVB         |             |             |             |             |             |             |
|-----|-------------|-------------|-------------|-------------|-------------|-------------|-------------|-------------|
|     | B<br>0.097  | C<br>0.077  |             |             |             |             |             |             |
|     | Al<br>0.143 |             | IVA         | VA          | VIA         | VIIA        | VIIIA       | VIIIA       |
|     |             | Ti<br>0.147 | V<br>0.132  | Cr<br>0.125 |             | Fe<br>0.124 | Co<br>0.125 | Ni<br>0.125 |
|     | Y<br>0.181  | Zr<br>0.158 | Nb<br>0.143 | Mo<br>0.136 |             | Ru<br>0.134 |             |             |
|     |             | Hf<br>0.159 | Ta<br>0.147 | W<br>0.137  | Re<br>0.138 |             |             |             |




Consid   $\gamma'$  former  Minor alloying additions   $\gamma$  former

Figure 1.1: Normal alloying elements presented in Ni-based superalloys [84].

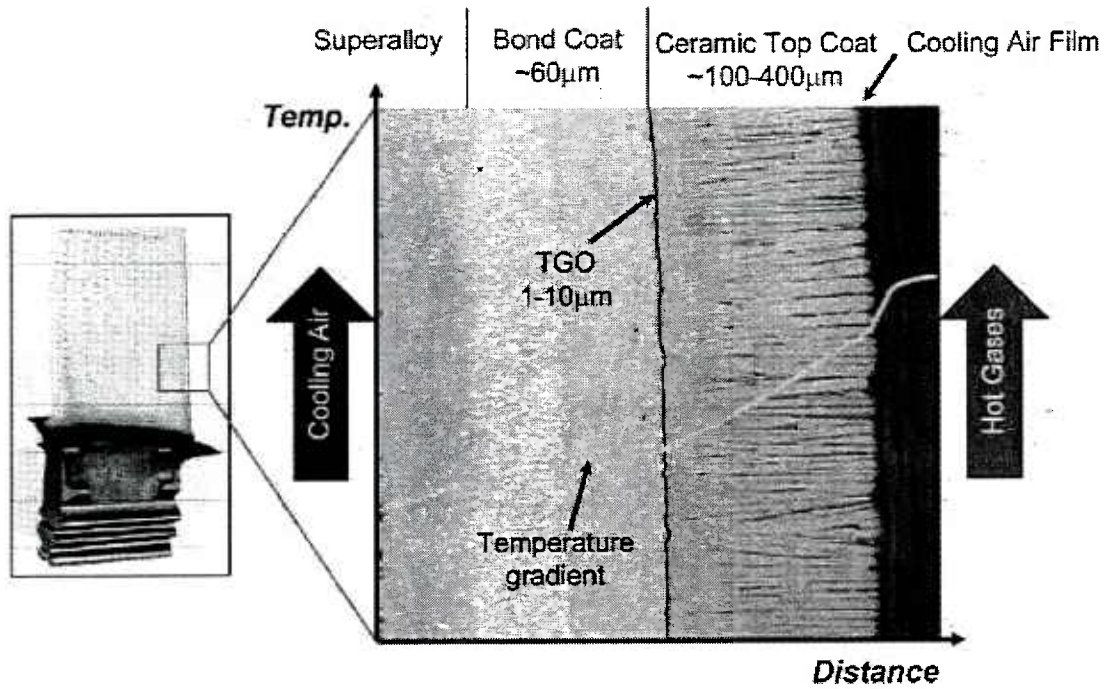


Figure 1.2: Cross section view of thermal barrier coating system [3]

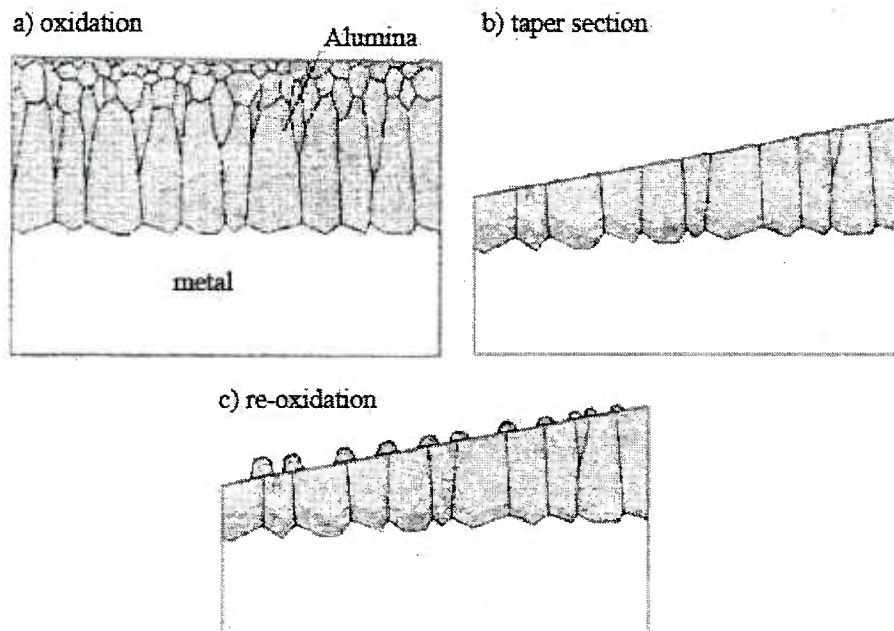


Figure 1.3: Schematic illustration of the experimental technique used to observe the outward growth due to Al grain boundary diffusion: a) typical scale structure after oxidation b) the outer scale layer is removed by polishing c) re-oxidation produces oxide ridges of different size depending on the thickness of the remaining scale. [18]

## ***1.2. The Effect of Reactive Elements Additions on Growth of Alumina Scales***

Over the years, it is well known that the rate of oxidation can be further reduced through the incorporation of “reactive” elements (REs) such as Y, La, Hf or Zr into the alumina scale. [1, 98] However, the complexity that the distribution and concentrations of REs in alloys, the alloys compositions and the oxidation temperature range can result in different REs effects. Studies have shown that REs can decrease or increase or have no effect on the oxidation rate, and even the same REs can generate different results if underlying alloy is different. [99, 100, 101]

### ***1.2.1 Studies on Hafnium’s Effect***

Hou et al. [1] compared the oxidation rate of alloys with or without RE additions from various groups, as summarized in Table 1.1. The results clearly showed consistent reduction of the oxidation rate by RE and the magnitude of reduction depends on types of REs. Among these dopants, hafnium is considered as one of the most effective REs in many studies.

Pint et al. [4, 5, 6, 7] studied various REs in different underlying alloys and found that 500ppm Hf doping in NiAl result in the lowest parabolic rate constant, in other words, the best observed oxidation performance at 1100°C -1200°C in Ni or Fe based alloy. Figure 1.4 depicted isothermal weight gains for various alloys doped with REs

in NiAl oxidized at 1200°C as a function of square root of time to show the parabolic rate growth kinetics. [74] Figure 1.5 listed the parabolic rate constant for various dopants in FeCrAl. [43] The results clearly showed that 500ppm Hf doping can lower the parabolic rate constant by almost factor of ten compared with 2~4 for other REs such as Y, Zr. Pint suggested that the better oxidation resistance for Hf than Y was due to Hf being more soluble in NiAl and therefore, fewer Hf-rich precipitates formed than Y-rich precipitates, which were considered as fast oxygen conductors. This hypothesis was partially supported by Tatlock et al., where high spatial resolution imaging was conducted to study Y and Hf distributions in the alumina grain boundaries in Y and Hf codoped-Fe-20Cr-5Al alloy oxidized at 1250°C for up to 100h in laboratory air. Two major findings can be concluded as below: First, Strong segregation of both Y and Hf to the alumina grain boundaries have been found; Second, the level of Hf in the grain boundary were measured to up to 1.5 wt%, which is higher than 0.3 wt% of Y. Therefore, it is reasonable to speculate based on the site-blocking mechanism that more Hf segregation in the grain boundary resulted in a improved oxidation resistance than Y.

However, recent work by Matsudaira et al. [28] conducted oxygen permeation experiment of Y- and Hf-doped alumina wafers under steep oxygen potential gradients at very high temperature above 1500°C. It found that Y-doping suppressed mainly the oxygen mobility and had no significant effect on aluminum mobility, while Hf-doping has the opposite effect. Based on the derived diffusivity equations, the extent Y-doping reduced prefactor of the oxygen permeation by a factor about 3



and Hf-doping reduced prefactor of the aluminum permeation by a factor about 2. Both dopants did not affect the activation energy compared with undoped. These results indicated that the effect of Hf and Y on reducing oxidation rate was similar, which seemed to be contrary to the studies on alloys. It is noteworthy that study on alumina grown on alloys was mainly conducted at lower temperature range from 900°C to 1200°C, while oxygen diffusion study in polycrystalline alumina was performed at relative temperature higher than 1400°C. Could the discrepancy that Hf-doping has better oxidation resistance than Y-doping is due to grain boundary structure transition at lower temperature regime?

Moreover, based on Pint's results, it was difficult to explain the additional benefit of Hf compared to Zr since both dopants were expected to have similar ionic radii, charge and oxygen affinity. One assumption is that Hf has a higher "effective" ionic radius due to its higher atomic number and hence larger Hf ion segregating in the alumina grain boundaries can be less mobile and more effectively reduce Al and O grain boundary diffusion. Naumenko et al. [9] studied the effect of Zr or Hf additions on the alumina scale formed on a high purity FeCrAlY model alloy oxidized at 1200°C -1300°C by using two-stage oxidation with  $^{18}\text{O}$ . The results showed that a great suppressed Y segregation in the scale grain boundaries and extensive incorporation of  $\text{ZrO}_2$  precipitates in the alumina scale resulted in an enhanced oxidation rate, while  $\text{HfO}_2$  precipitates were smaller and more homogeneously distributed in the alumina scale resulted in no such accelerative effect on the oxidation rate. These findings suggested that Hf might have a slower mobility than

Zr. However, the possible interaction between Hf/Zr with Y cannot be ruled out and complicated underlying mechanisms. Moreover, 500ppm Hf-doping was considered be the optimum doping levels with the best-observed oxidation resistance in NiAl by Pint. If the Hf content is too low, little or no benefit will be observed, whereas higher than optimum Hf levels would accelerate the alumina scale growth rate by oxidizing internally and forming  $\text{HfO}_2$  pegs, which could transport oxygen rapidly. By comparing Pint and Naumenko's results, it may be argued that whether the presence of Hf-rich precipitates could affect the oxidation rate.

Moreover, it has been recognized that the optimal amount of dopant to add to alumina-formers seemed to depend on other impurities in the alloy, particularly S and C. [75, 76, 77] In Hf-doped NiAl, the Hf/C ratio has been observed to be essential in optimizing the scale adhesion since Hf likes to getter C to form carbides. Figure 1.6 depicted polished cross-sections of the alumina scale formed on various castings of NiAl+Hf after 10, 100h cycles at 1200°C. [77] The results clearly showed that with decreasing Hf/C ratios, in other words, more C content, the scale became more convoluted and more subject to spallation. Pint et al. also found that by either decreasing the C addition into the alloy or by replacing Zr with Hf, the oxidation lifetime was increased by a factor of two or six in the wrought Fe- 40Al. One possible explanation for the improved lifetime with lower C content is due to removal of C weakened the alloy, which resulted in more easily accommodating stress from growing oxide and hence, less spallation. The other explanation is lower C content indicating less Hf tied up as  $\text{HfC}$ ; in other words, more Hf can diffuse to the scale

grain boundary to reduce the growth rate. Since stress is proportional to the scale thickness, a large Hf/C ratio would increase the alloy's lifetime.

In summary of above discussions, due to so many variables for the traditional oxidation study of alumina grown on alloys such as underlying alloy type, dopant levels, impurity levels, oxidation temperature, a more controlled and system with minimized mutual impurity interaction is essential to truly uncover the underlying mechanism of REs such as Hf.

Table 1.1 Effect of Reactive Element Addition on Oxidation Rates [1]

| Alloy system       | Oxidation condition (°C) | Rate without RE                 | RE type                               | Rate with RE                    |
|--------------------|--------------------------|---------------------------------|---------------------------------------|---------------------------------|
| NiAl               | 1200                     | $(1.4 \pm 0.4) \times 10^{-11}$ | Ti, La, Zr, Hf, Y                     | $(8.0 \pm 4.1) \times 10^{-12}$ |
| Ni <sub>3</sub> Al |                          | $7.1 \times 10^{-12}$           | Y                                     | $(4.3 \pm 3.1) \times 10^{-12}$ |
| Fe <sub>3</sub> Al |                          | $(1.3 \pm 0.2) \times 10^{-11}$ | Hf, Zr, Y                             | $(4.9 \pm 2.4) \times 10^{-12}$ |
| FeCrAl             |                          | $(1.8 \pm 0.6) \times 10^{-11}$ | Nb, Ti, Sc, Hf, Gd, Ba, Nd, La, Zr, Y | $(7.1 \pm 2.8) \times 10^{-12}$ |
| PtAl               |                          | $(1.6 \pm 0.4) \times 10^{-11}$ | Zr                                    | $4.1 \times 10^{-12}$           |
| FeCrAl             | 1200                     | $7.8 \times 10^{-12}$           | Y                                     | $4.1 \times 10^{-12}$           |
| FeCrAl             | 1150                     | $8.5 \times 10^{-12}$           | Ti                                    | $2 \times 10^{-13}$             |
| NiCrAl             | 1100                     | $1.1 \times 10^{-12}$           | Y, Hf                                 | $(4.5 \pm 2.1) \times 10^{-13}$ |

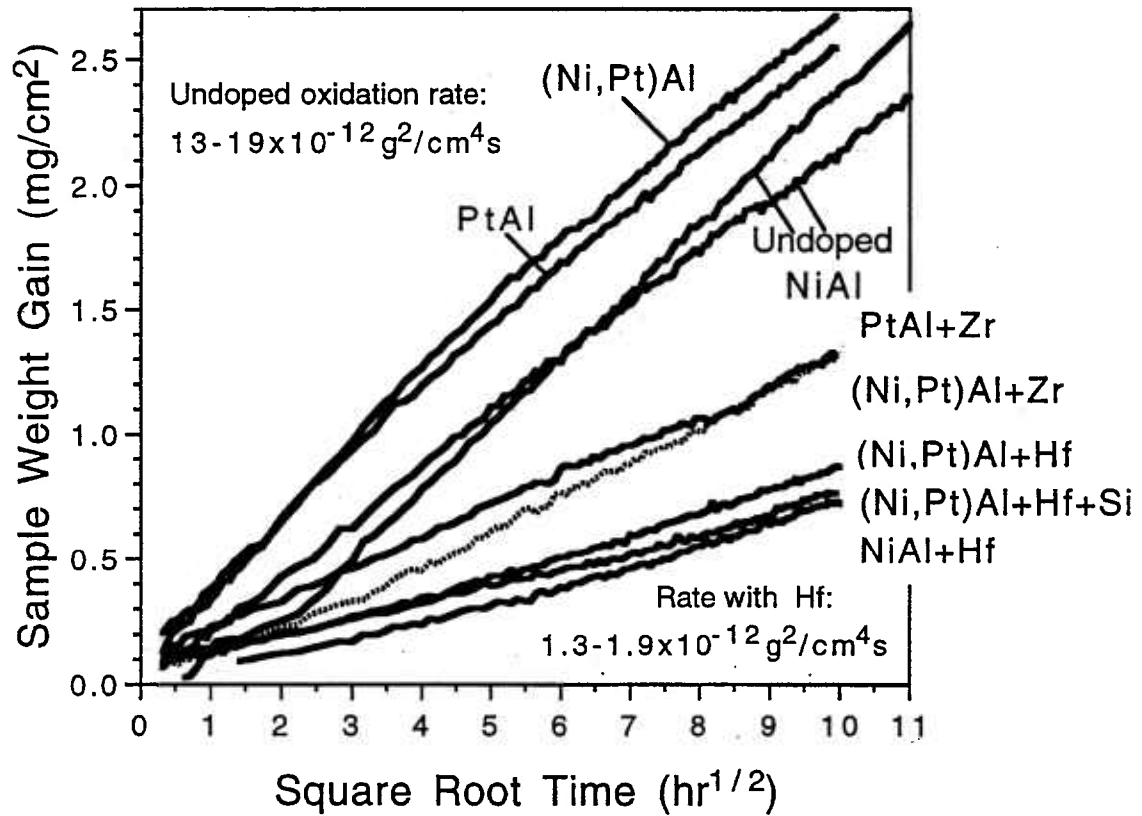


Figure 1.4: Isothermal weight gains for various alloys doped with REs oxidized at 1200°C plotted as a function of square root of time to show the parabolic rate growth kinetics. [74]

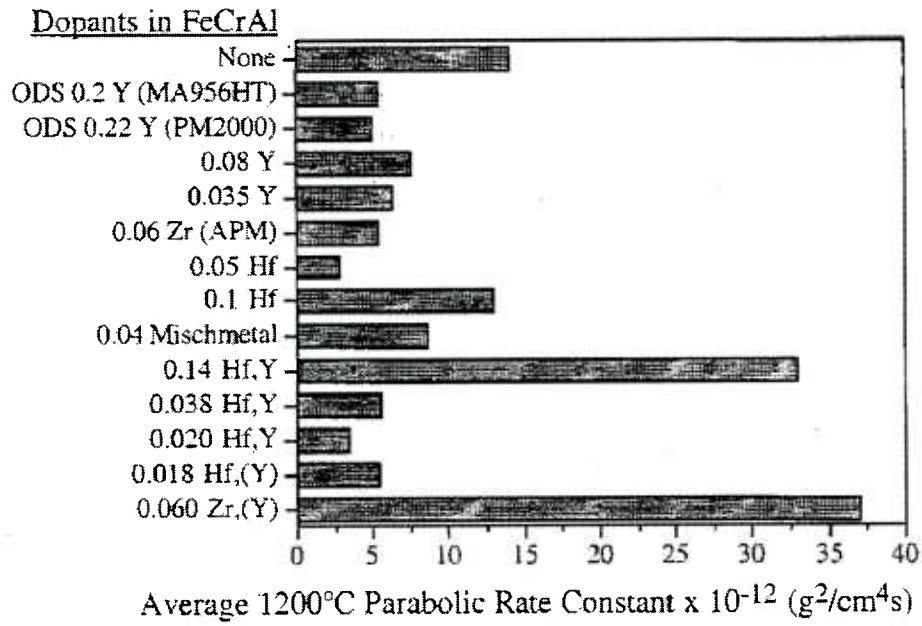


Figure 1.5: Average parabolic rate constants for various commercial and laboratory FeCrAl doped with different REs oxidized at 1200°C. [78]

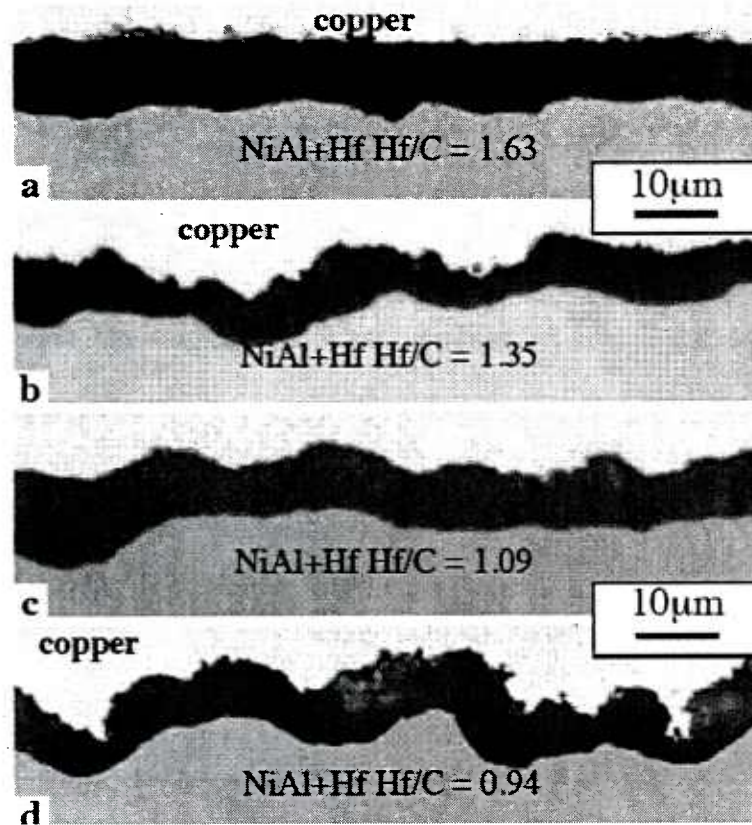


Figure 1.6: Optical microscopy of polished cross-sections of the alumina scale formed on various castings of NiAl+Hf after 10, 100h cycles at 1200°C. [77]

### ***1.2.2 Proposed Mechanisms***

As described earlier, many researchers have studied the influence of reactive elements on the oxidation rate on the commercial alloys to elucidate the underlying mechanisms, however, a full explanation of this phenomenon is not yet available. But it is essential to briefly review some of the major mechanisms proposed from various groups.

The “site blocking” mechanism was originally based on a series of studies focused on dopant’s effect on creep resistance in polycrystalline alumina. [10, 11, 15, 24, 25, ] The results suggested that REs having relatively larger ionic radii ( $\text{Hf}^{4+}$ , 0.71Å;  $\text{Zr}^{4+}$ , 0.72Å;  $\text{Y}^{3+}$ , 0.9Å;  $\text{La}^{3+}$ , 1.06Å) than  $\text{Al}^{3+}$  (0.56Å) would change the grain-boundary environment by “blocking” nominal fast paths and therefore, reduced the diffusional creep rate. It is reasonable to speculate that the segregation of REs in the alumina grain boundaries will block some of the O and Al diffusion path, therefore achieving a better oxidation resistance. This mechanism was supported by Carter et al.’s [13]work by using DFT calculation of diffusion pathways of REs on the  $\alpha\text{-Al}_2\text{O}_3$  (0 0 0 1) surface to simulate diffusion of Al and O along the alumina grain boundaries. The calculation found that REs such as Hf or Y diffuse via almost the same pathway as Al across the surface, while only part of the pathway as O across the surface. The results also suggested that Hf and Y readily segregate to oxide grain boundaries and mainly block the sites along the Al diffusion pathway, thereby slowing down the oxide growth rate.



Another possible mechanism is that REs segregating in the alumina grain boundaries could increase the bond-strength of RE-O compared with Al-O. [12, 13] Buban et al. [12] conducted atomic resolution microscopy and high-precision calculations in alumina grain boundaries doping with yttrium. The results suggested that Y ions are energetically more stable at the grain boundaries and increased the number of bonds with O, and the bond strength is increased as well due to the higher covalency of the Y-O bonds. Similar effects are expected for other REs such as Zr or La. In the case of oxidation, the stronger RE-O bonds could increase the adhesion between alumina and alloy, which resulted in a longer lifetime. It should be pointed out that whether the stronger RE-O bond could affect the O and Al transport in the alumina grain boundary is not clear.

Complicated thing further, recent work by Heuer et al. [14] suggested that the REs may affect the oxidation behavior not by geometric /structural site blocking effects at grain boundaries due to segregation but by modifying grain-boundary donor and acceptor states to the extent that Al ionization at the substrate/scale interface is reduced, which in turn reduces the extent of Al vacancy injection into the scale. This has the effect of causing the doped  $\text{Al}_2\text{O}_3$  scale to grow in a predominantly inward direction, due to migrating oxygen ions reacting with Al at the  $\text{Al}_2\text{O}_3$  /alloy interface. In summary, due to the complexity of experimental conditions, it is essential to study separate effect of reactive elements on oxygen and aluminum diffusion in alumina scales in a purer environment to minimize the interfering factors.

## ***Chapter 2. Grain Boundary Diffusion Studies in Polycrystalline Alumina***

Understanding grain-boundary diffusion is essential to better control the evolution of the microstructure and properties of materials. As described in the earlier chapter, the growth of alumina scale is mainly formed by simultaneously oxygen outward diffusion and inward aluminum diffusion. Therefore, figuring out how the influence of REs on the transport behavior is essential to high temperature oxidation, as well as other scientific and technological areas such as sintering or diffusional creep of alumina when grain boundary diffusion plays an important role.

Early studies [103, 104] on aluminum diffusion in alumina have been performed by using  $^{26}\text{Al}$  radioactive isotope involving serial mechanical sectioning of a sample. However, due to the inconvenience of long lifetime of the  $^{26}\text{Al}$  isotope,  $\text{Cr}^{3+}$  has been used as the substitute for  $\text{Al}^{3+}$  given their similar ionic radii, isovalency and the mutual solubility of chromia and alumina at temperatures exceeding  $900^\circ\text{C}$ . [102] In the current work, we will mainly focused on the anion grain boundary diffusion in alumina instead of cation diffusion, therefore, the oxygen grain boundary diffusion. Before reviewing the results of oxygen grain boundary diffusion by other groups, it is vital to briefly explain the classic theory behind the experimental methods and discuss some of the common solutions.

## ***2.1 Theoretical Background of Grain Boundary Diffusion in Polycrystals***

### ***2.1.1 Diffusion Kinetics in Polycrystals***

A grain boundary is traditionally viewed as the thin interfacial transition region between two adjacent grains with different crystallographic orientation. On the macroscopic view, grain boundaries have 5 degrees of freedom, which can be described by the orientation of the boundary plane to the two grains and the 3-dimensional rotation required to bring the grains into coincidence, or usually called misorientation. Within the few atomic layers thick, the grain boundary has a higher atomic mobility than the corresponding crystal lattice due to the interruption of the periodic arrangement of atoms, reduction of the average coordination number or different bond length from the bulk lattice. When temperature is high enough that atoms are mobile in both the crystal lattice and the grain boundaries, a variety of diffusion situations may exist, depending on the heat treatment time, grain sizes, geometrical arrangement of the boundaries and the diffusion rates in the boundaries and lattices. Harrison [105] proposed a three class of grain boundary diffusion

kinetics that depends on the relationship between the lattice diffusion distance and grain size of the materials (distance between adjacent grain boundaries) considered. A schematic plot has been shown in Figure 2.1. If total diffusion time is  $t$ , lattice diffusivity is  $D$ , grain boundary diffusivity is  $D_b$ , therefore, the diffusion distance of atoms in the lattice and along the grain boundaries are given by  $(Dt)^{1/2}$  and  $(D_b t)^{1/2}$  respectively. The Type A regime is observed mainly at high temperatures, and/or long anneals. Under such condition, the lattice diffusion length,  $(Dt)^{1/2}$ , is greater than the spacing  $d$  between the grain boundaries, which suggests that the diffusion front covers many grains and grain boundaries during the time  $t$ . An effective diffusion coefficient  $D_{\text{eff}}$  can be used to describe the overall the diffusion based on Hart's equation:

$$D_{\text{eff}} = fD_b + (1-f)D \quad (2.1)$$

Where  $f$  is defined as the volume fraction of grain boundaries in the material. If the temperature is lower, and/or the diffusion anneal is shorter than that of Type A, the diffusion kinetic region is called Type B. Contrary with Type A, the lattice diffusion of neighboring grain boundaries do not overlap with each other since lattice diffusion could not diffuse as far as large distances as the boundaries spacings, although there is significant diffusant leakage to the lattice as well, which means the atoms can penetrates along the grain boundaries much deeper than in the lattice and grain boundaries can be treated to be isolated. For reasonable anneal times, Type B

comprises the widest and the most convenient temperature range. In the third condition, when annealing at even lower temperature or shorter anneal times than that of Type B; grain boundary diffusion is much faster than the lattice diffusion. Therefore, diffusion takes place only along the grain boundaries without any leakage to the lattice. This kinetic region is called Type C, which is usually very difficult to measure.

### ***2.1.2 Mathematical Solution in the Type B Regime***

Fisher [106] published the classic paper presenting the first theoretical model of grain boundary diffusion based on Fick's laws. The grain boundary is pictured in Figure 2.2 as a thin slab with thickness  $\delta$  placed into a semi-infinite perfect crystal, normal to the surface that a constant diffusion source applied. It is assumed that the coefficient of grain boundary diffusion  $D_b$  is much greater than the lattice diffusion  $D$ , which means the diffusant penetrates much deeper along the grain boundary than in the grains.

One common used solution was proposed by Whipple and Le Claire [107, 108], assuming the diffuser concentration kept constant at the surface and zero everywhere inside the sample at the beginning. The product of grain boundary width  $\delta$  and grain boundary diffusivity  $D_b$ , can be described as below:

$$\delta D_b = \frac{D^{\frac{1}{2}}}{t} (0.78)^{\frac{5}{3}} \left( -\frac{\partial \ln \bar{C}}{6 \partial y \bar{y}} \right)^{-\frac{5}{3}} \quad (2.2)$$

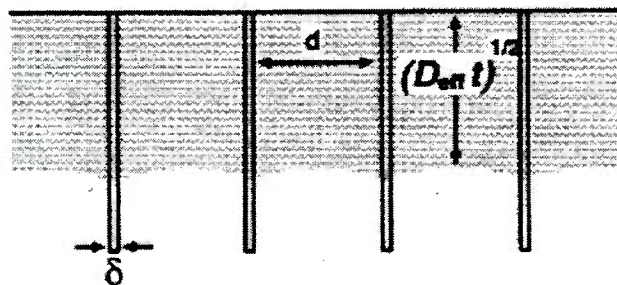
Where the slope of the diffusion depth profile can be easily obtained from a SIMS study. It should be noted that this equation is valid for the region far from the diffusion source and the larger the value of  $\beta$ , which is defined in equation 2.3, the more pronounced is the lateral diffusion along the grain boundary. Therefore, for an accurate determination of  $D_b$  from experiments, the annealing conditions must be chosen that  $\beta$  is greater than 10.

$$\beta = \frac{(\frac{D_b}{D} - 1) \delta}{2 D t^{\frac{1}{2}}}$$

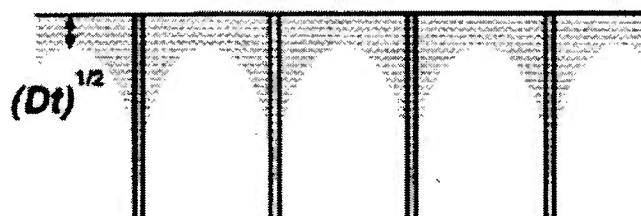
(2.3)

Besides the constant source solution, Suzuoka [110] worked out a solution for an instantaneous source, where the initial diffuser layer can be completely consumed during the diffusion experiment. The exact expression for this solution can be found in [110] in detail. By comparing between these two types of diffusion source, it can be found that for instantaneous source, near the surface region, grain boundary acts as a sink for the diffuser. Beyond a certain depth, the grain boundary behaves as a source for the diffuser. While for the constant source solution, the grain boundary always acts as sink for the diffuser.

**Type A**



**Type B**



**Type C**

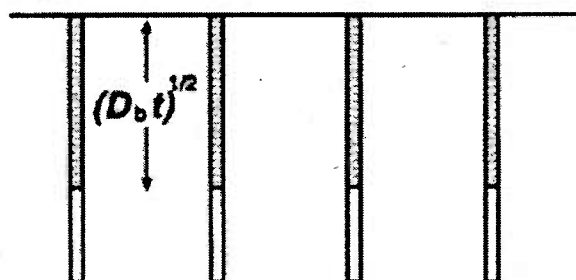


Figure 2.1: Schematic illustration of types A, B and C diffusion kinetics in a single crystal material containing uniformly spaced planar fast diffusion paths.

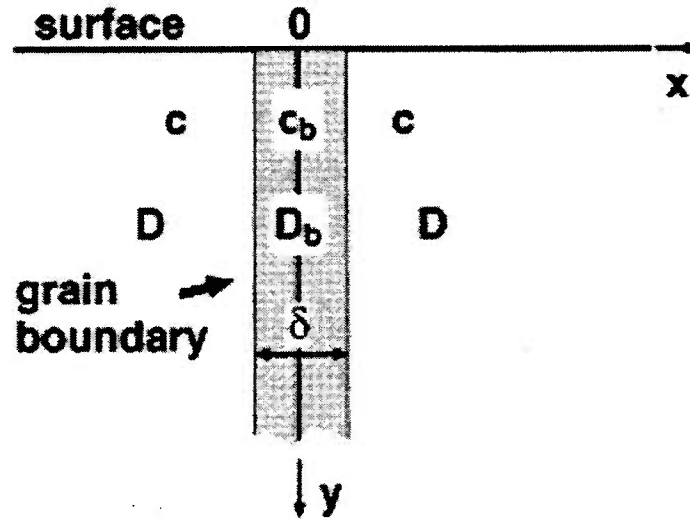


Figure 2.2: Schematic plot for Fisher's model [109]



## ***2.2. Experimental Method of Obtaining Grain Boundary Diffusion in Polycrystals***

### ***2.2.1 Diffusivity Calculation from Secondary Ion Mass Spectrometry Analysis***

Secondary ion mass spectroscopy (SIMS) is a major analytical technique for surface characterization utilizing ion beam such as  $\text{Ar}^+$  knocking away atoms from the surface, producing neutral atoms and ions, which the latter can be analyzed in a mass spectrometer. Different ions can be differentiate due to chosen mass/charge ratios and are delivered to the detector for counting. [111] Therefore, by controlling where the primary ion beam strikes the sample surface, continuous analysis while sputtering away certain atomic layers produced information used for depth profiles by monitoring the secondary ion count rate of interested elements as a function of distance away from the surface.

For example, in the case of studying oxygen grain boundary diffusion in alumina, a two-stage oxidation method was used. The alloys were first oxidized in a  $^{16}\text{O}$  atmosphere for a certain time with a certain scale thickness. Then the sample was

annealed in an  $^{18}\text{O}$  atmosphere. By using SIMS,  $^{18}\text{O}$  concentration can be calculated by using Equation 2.4:

$$\bar{C}(^{18}\text{O}) = \frac{\rho(^{18}\text{O})}{\rho(^{18}\text{O}) + \rho(^{16}\text{O})} = \frac{I(^{18}\text{O})}{I(^{18}\text{O}) + I(^{16}\text{O})} \quad (2.4)$$

Where  $^{18}\text{O}$  atom density  $\rho = \text{RSF} \frac{I_s}{I_m}$ . RSF is called relative sensitivity factor, which is determined by measuring ion collection efficiencies from known matrices and recording them as a ratio to a reference element that is usually the most abundant metallic atom in the matrix. [112]  $I_s$  and  $I_m$  are defined as the mass selected impurity isotope secondary ion intensity in counts/s and the matrix isotope secondary ion intensity in counts/s respectively. A typical SIMS acquired  $^{18}\text{O}$  concentration profile is shown in Figure 2.3. The initial strong decrease of  $^{18}\text{O}$  concentration is due to both bulk and grain boundary diffusion and is followed by long-range diffusion where only grain boundary diffusion plays an important role. By plotting  $\ln \bar{C}(^{18}\text{O})$  as a function of  $x^{6/5}$ , grain boundary diffusivity can be calculated by using Equation 2.2. It should be pointed out that the ion probe size in the SIMS ( $\sim \mu\text{m}$ ) is usually much larger than the grain boundary region ( $\sim \text{nm}$ ), which means that sample needs a large volume fraction of grain boundaries in order to obtain an appreciable signal.

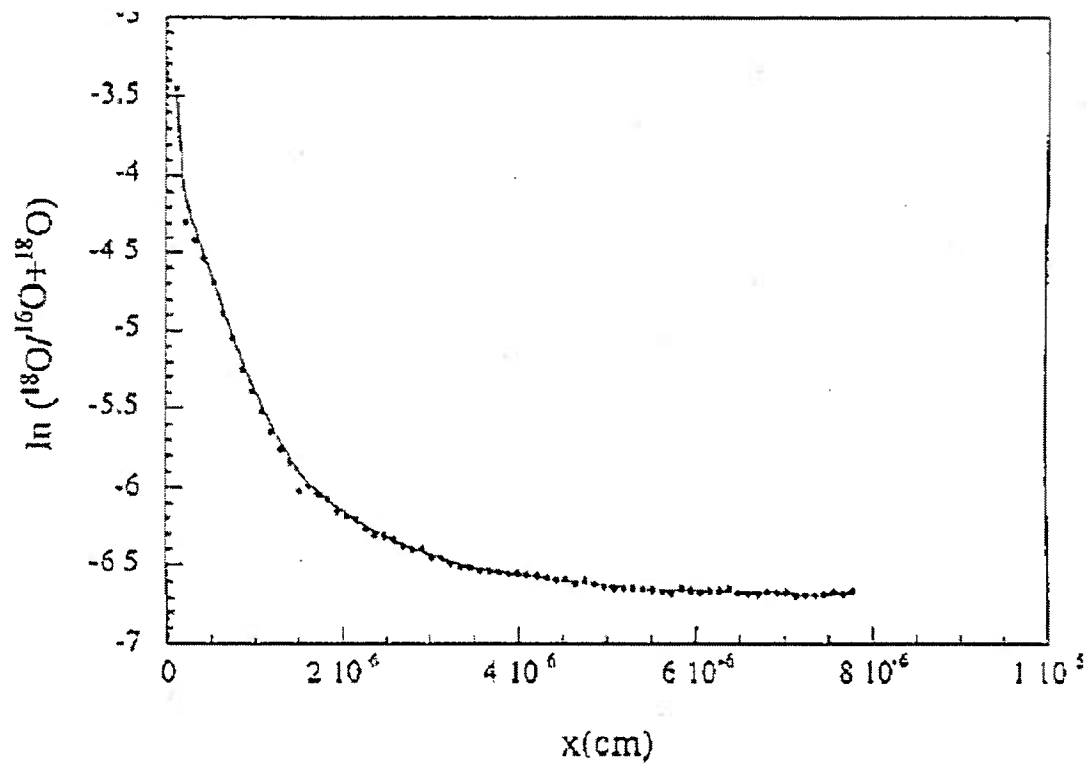


Figure 2.3:  $^{18}\text{O}$  concentration profile plot against depth  $x$  (cm) (68)

### ***2.2.2 Diffusivity Calculation from Gravimetrically Determined Growth***

Besides using the isotope and SIMS, another common method to obtain oxygen grain boundary diffusivity is based on measuring continuous weight change due to oxidation as a function of time, which is also called gravimetric technique. When the alumina formed on the underlying alloy's surface during the oxidation, the sample continuously increased in weight. In most cases, the oxide growth occurs with a continuing decreasing oxidation rate, which is therefore proportional to either weight of oxide formed or the scale thickness. After integration, the parabolic rate constant can be described as below:

$$\left(\frac{\Delta M}{Area}\right) = k_p t$$

(2.5)

Or

$$x^2 = k_c t$$

(2.6)

Where  $\Delta M$  is the increase mass of the sample,  $x$  is the scale thickness,  $t$  is the oxidation time,  $k_p$  ( $\text{g}^2/\text{cm}^4 \cdot \text{s}$ ) and  $k_c$  ( $\text{m}^2/\text{s}$ ) can be converted with each other by following the relationship below:

$$k_c = \left( \frac{M_{Al_2O_3}}{3M_o \rho_{Al_2O_3}} \right) k_p \quad (2.7)$$

According to classic Wagner's theory on oxidation of metals, [113]

$$k_c = \frac{1}{RT} \int_{\mu_o^2}^{\mu_o^1} D_{eff} \cdot d\mu_o \quad (2.8)$$

Where  $\mu_o^1$  and  $\mu_o^2$  are the chemical potential of the gas at the oxide metal interface and oxide/gas interface, respectively, which are related to oxygen partial pressure as well.  $D_{eff}$  stands for the effective diffusion coefficient, which  $\approx (2\delta/r) \cdot D_o$  when the growth of the scale is mainly determined by inward oxygen grain boundary diffusion. Therefore, the value of  $\delta D_o$  can be obtained through:

$$D_o \times \delta = \frac{RT}{2} \cdot \frac{k_c r}{\Delta\mu_o} \quad (2.9)$$

Where  $\delta$  is grain boundary width,  $\Delta\mu_o$  is the oxygen chemical potential gradient across the scale and  $r$  is the grain size. However, the calculated  $k_c$  was generally not in good agreement with experimental values. It should be pointed out that Wagner's theory is valid based on several assumptions such as: The oxide layer

is dense and coherent; the oxidation rate is depending on oxygen partial pressure. Balmain et al (68) suggested that the discrepancy between the experiment and calculation was mainly due to the variation of the diffusion coefficients existing in the thickness of the scale, which was very difficult to measure experimentally. Moreover, whether the oxidation rate depends on the oxygen partial pressure is still under debate. Earlier work by Ramanarayanan et al. [69] suggested the alumina growth rate is independent of the oxygen partial pressure while recent work by the Japanese group [70] showed the oxygen and aluminum grain boundary diffusivity depending on oxygen pressure by conducting oxygen permeation experiments. It is suggested that Wagner's theory for oxidation rate might not apply well to the growth of alumina scales.

### ***2.2.3 Studies of Grain Boundary Diffusion by Other Groups***

Various studies have been conducted to obtain oxygen grain boundary diffusivity in either undoped or doped alumina. However, the lacking of consistence between the prefactor and activation energy is traditionally difficult to understand, as summarized by Heuer [71] in his recent review paper on oxygen and aluminum diffusion in  $\alpha$ - $\text{Al}_2\text{O}_3$ . As shown in the table 2.1, the prefactor and activation energy for oxygen grain boundary diffusion were compared between various studies. It can be seen clearly that the prefactor could vary orders of magnitude difference for undoped alumina although it can be argued that bicrystal is not well representative of polycrystal. The situation became more complicated for Y-doped sample, not only the large difference

in the prefactor, but also the activation energy. Moreover, it was found that the activation energy for oxygen grain boundary diffusion was larger than that for lattice oxygen diffusion, contrary to what is found in metals. He suggested that the enhanced oxygen grain boundary diffusion was due to the glide/climb of the grain boundary dislocation, rather than enhanced diffusive jumping of point defects in the “disordered” regions adjacent grain boundaries. Another explanation is that  $\text{Al}_2\text{O}_3$  may have a different grain boundary structure or chemistry depending on the temperature regime since creep and diffusion experiments usually performed at temperature higher than  $1200^\circ\text{C}$  and oxidation experiments generally conducted at temperature from  $900^\circ\text{C}$  to  $1200^\circ\text{C}$ .

Another interesting work on oxygen grain boundary diffusion was conducted by Nakagawa et al. [72], who measured oxygen diffusion coefficients along five-grain boundaries in alumina bicrystals with controlled geometry by means of isotopic exchange and diffusion depth profiling via SIMS. It should be pointed out that all the five grain boundaries were coincident site lattice boundaries ( $\Sigma 7$ ,  $\Sigma 21$ ,  $\Sigma 31$ ) but combined with different grain boundary planes including  $\{2\ -3\ 1\ 0\}$ ,  $\{4\ -5\ 1\ 0\}$  and  $\{7\ -11\ 4\ 0\}$ . The oxygen diffusivity can vary by a factor of  $10^3$  depending on the grain boundary character. The results also suggested that the correlation between  $\Sigma$  value and diffusivities were slightly, while the correlation between grain boundary plane and diffusivities were much stronger. This relationship was not altogether unexpected since boundaries with same grain boundary plane had similar atomic structures, and therefore, similar oxygen diffusion parameters. This study indicated

that oxygen grain boundary diffusivity is related to grain boundary atomic structures and hence the grain boundary character, especially grain boundary planes. Considering that polycrystals having grain boundaries with different grain boundary character, the oxygen grain boundary diffusivity could vary within individual grain boundaries. This statement has been verified by using  $^{18}\text{O}$  and Time of Flight-SIMS. As shown in Figure 2.5, the bright contrast showed different concentrations of  $^{18}\text{O}$  in the grain boundaries for undoped alumina polycrystal. [114] The results suggested that obtaining activation energy for oxygen grain boundary diffusivity derived from average data at different temperature could be problematic since random grain boundaries may not be equal. Complicating things further, different groups have different experimental conditions such as doping types, doping levels, annealing temperature. Therefore, more detailed and controlled experiments are needed.



Table 2.1 Arrhenius parameters,  $D_0$  and  $Q$ , for diffusive processes in  $\alpha\text{-Al}_2\text{O}_3$  ( $D = D_0 \exp(-Q/RT)$ ) from [71]

| Oxygen Grain Boundary Diffusion, $D_{b\text{-oxy}\delta}$ | $D_0$ ( $\text{m}^2/\text{s}$ ) | $Q$ (kJ/mol) |
|---|---------------------------------|--------------|
| Reddy thesis (undoped)                                    | $5.5 \times 10^1$               | 825          |
| Prot et al. (undoped)                                     | $1.2 \times 10^2$               | 884          |
| Prot et al. (Y-doped)                                     | $1.2 \times 10^{-3}$            | 780          |
| Messaoudi et al. (Y-doped FeCrAl)                         | $2.1 \times 10^1$               | 391          |
| Clemens et al. (Y-doped FeCrAl)                           | $3.5 \times 10^2$               | 310          |
| Nakagawa et al. (undoped bicrystal)                       | $8.4 \times 10^{-6}$            | 627          |
| Nakagawa et al. (Y-doped bicrystal)                       | $6.5 \times 10^{-4}$            | 729          |

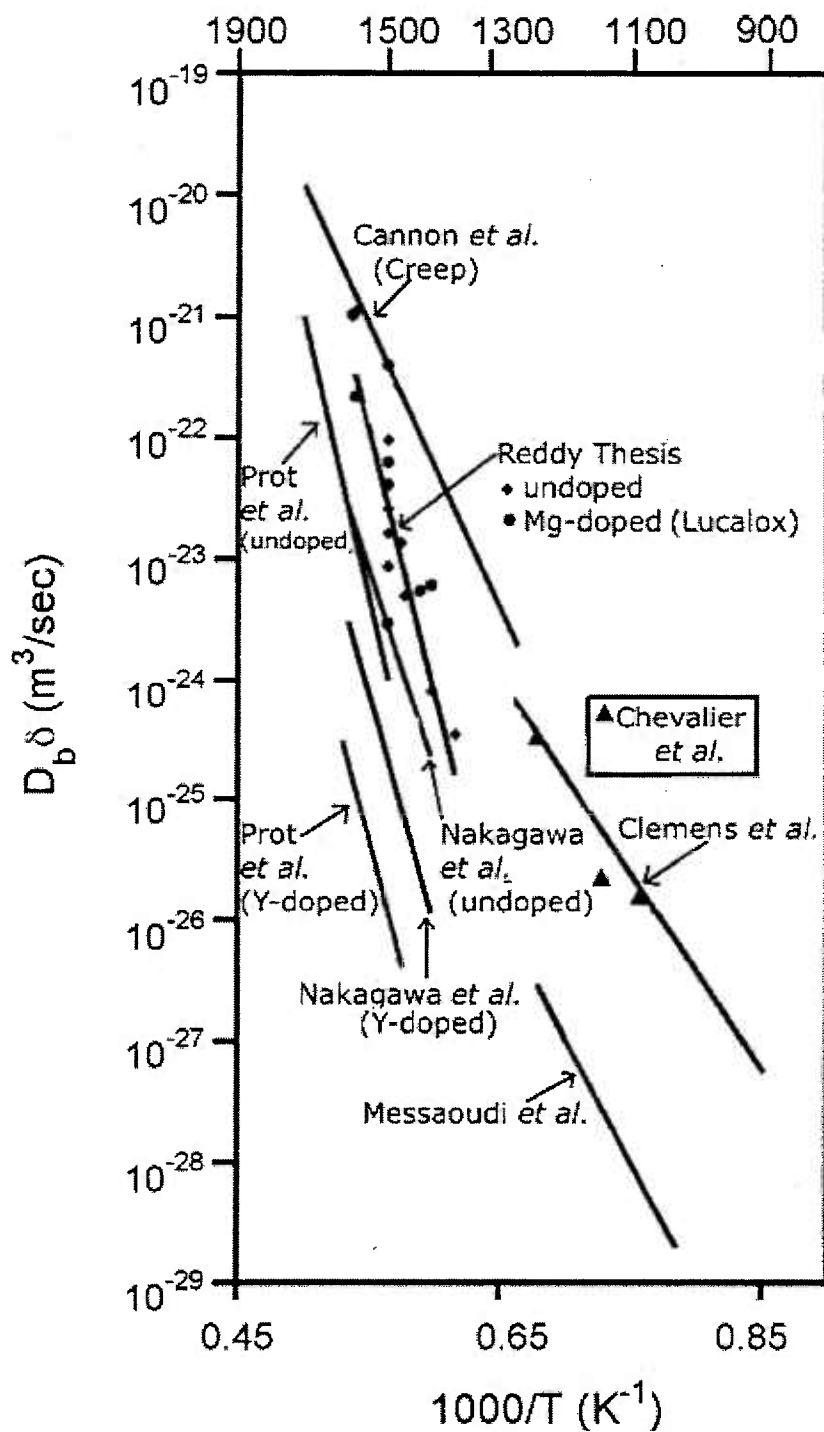


Figure 2.4: Oxygen grain boundary diffusion in  $\alpha\text{-Al}_2\text{O}_3$  summarized by Heuer. [71]

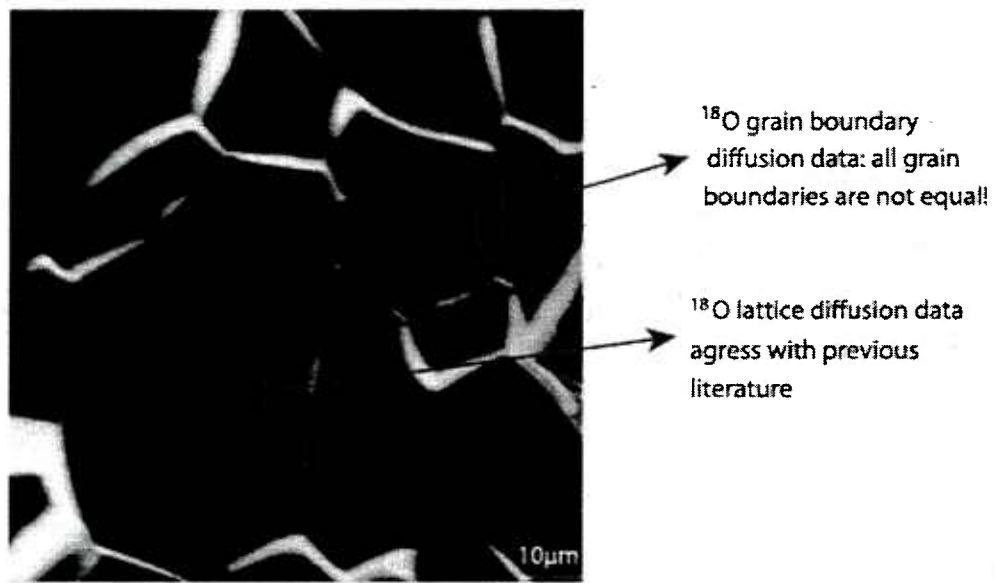


Figure 2.5:  $^{18}\text{O}$  TOF-SIMS image with  $\sim 100\text{nm}$  spatial resolution for fully dense sintered  $\text{Al}_2\text{O}_3$  polycrystal with about  $10\mu\text{m}$  grain size. The contrast is due to differences in grain boundary diffusivities.[114]

## ***2.3 Grain Boundary Complexions***

### ***2.3.1 Definitions of Grain Boundary Complexions***

It is generally believed that the boundaries between the adjacent crystals or grains play a decisive role in determining the properties and processing of engineering materials, especially in metals and ceramics. With the development of high-resolution electron microscopy and other experimental techniques, a new scientific concept to tackle classical problems such as abnormal grain growth has been proposed by Dillon and Harmer [32, 33] based on extensive work to study grain growth kinetics in alumina. They first proposed that grain boundaries exhibit phase-like behavior, in which the structure, chemistry, and properties may change discontinuously at critical values of thermodynamic parameters such as temperature, pressure, and chemical potential. Therefore, contrary to traditional concept that grain boundaries are planar, non-transformable two-dimensional defects that only depend on the crystallographic misorientation across the interface and segregant atoms, grain boundaries can be considered as distinct phases, or “complexions”, which are in thermodynamic equilibrium with its abutting phases. It should be pointed out that a complexion cannot exist independently of the abutting phases and its average composition and structure need not to be the same as the abutting phases.

As shown in Figure 2.6, the grain boundary mobility has been plotted as a function of inverse temperature for undoped and doped alumina. The results suggested that there

are 6 different regimes into which the grain growth kinetics can be categorized. Atomic-scale structures of grain boundaries that correspond to grain boundary mobility can be obtained by using high-angle annular dark field scanning electron transmission electron microscopy (HAADF-STEM), as shown in Figure 2.7, where these six complexions can be distinguished based on solute atoms' thickness: clean complexions with no observation of dopants, monolayer complexions, bilayer complexions, trilayer complexions, nanolayer complexions and wetting layers. The results further indicated that there is generally an increase in grain boundary mobility with an increase in the disorder within the core of the grain boundary, which suggested the observation of abnormal grain growth is due to the coexistence of two or more types of grain boundary complexions, where the drastically different grain boundary motilities lead to bimodal microstructures.

Besides alumina, complexions have been observed in other metals and ceramics as well. [54~59] Recent work by Luo et al [54] investigated ductile metals such as Ni when exposed to liquid metals Bi. By using aberration-corrected scanning transmission electron microscopy, a bilayer Bi interfacial phase in the Ni grain boundaries was observed, as shown in Figure 2.8. Careful analysis showed that the decohesion between the two adsorbed Bi layers that were incoherently and weakly bonded was the root cause of the liquid metal embrittlement. The observation demonstrated that dopants adsorption could induce complexion transitions, resulting in abrupt changes in materials' properties. The above two examples suggested that if a significant fraction of the grain boundaries in a polycrystalline material undergo a

transition, the cumulative effect can be dramatic and macroscopic properties can be greatly influenced.

It is essential to briefly discuss the categorization of complexion transitions since a wide variety of terminology has been used. Cahn first classified the complexion transitions into two groups, which are congruent and non-congruent. The congruent transitions refer to the change of the structure and/or the chemistry of grain boundary core while the morphology of the grain boundary remains invariant. As for non-congruent transitions, besides the change of grain boundary cores, the grain boundary facets into new orientations or a bulk phase completely wetting the original grain boundary creates two new ones. From the experimental view of examining the grain boundary exsitu by using scanning/transmission electron microscopy, it is difficult to conclude that a congruent transition has occurred rather than a non-congruent transition if non-congruent transition occurred quickly enough. Therefore, more practical classification have been proposed and illustrated in detail in Figure 2.9, which were summarized by Cantwell et al. [46]

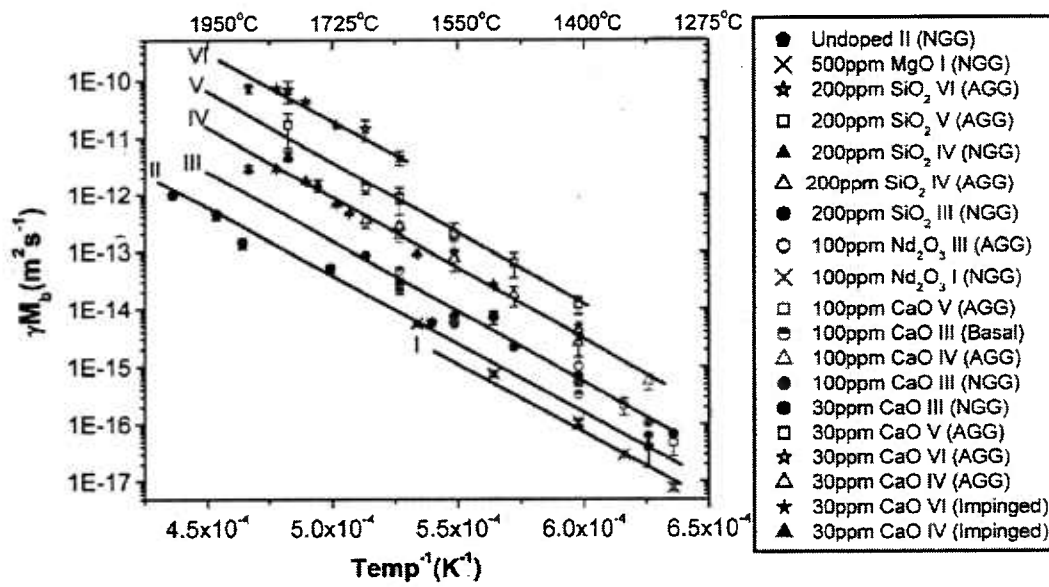


Figure 2.6: Grain boundary mobility as a function of inverse temperature for undoped and doped alumina [32]

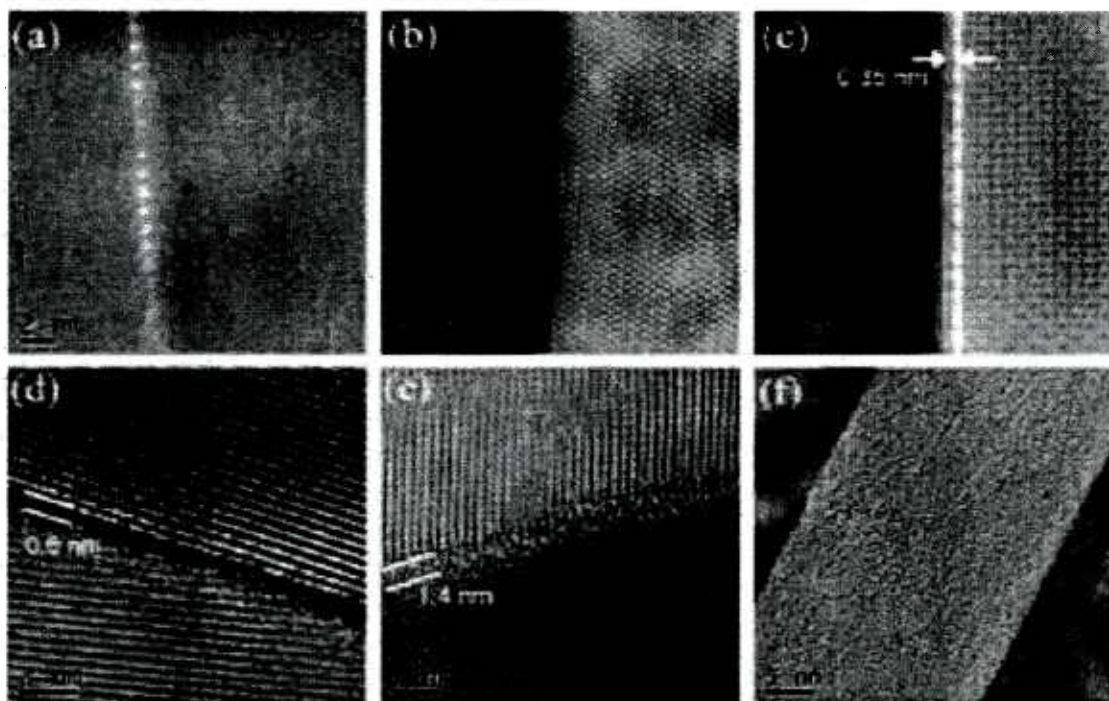


Figure 2.7: High angle annular dark-field scanning transmission electron micrographs of six discrete Dillon-Harmer complexions in undoped and doped alumina (CaO, MgO, SiO<sub>2</sub>, Nd<sub>2</sub>O<sub>3</sub>) (a) Clean. (b) Monolayer. (c) Bilayer. (d) Trilayer. (e) Nanolayer. (f) Wetting. [32]

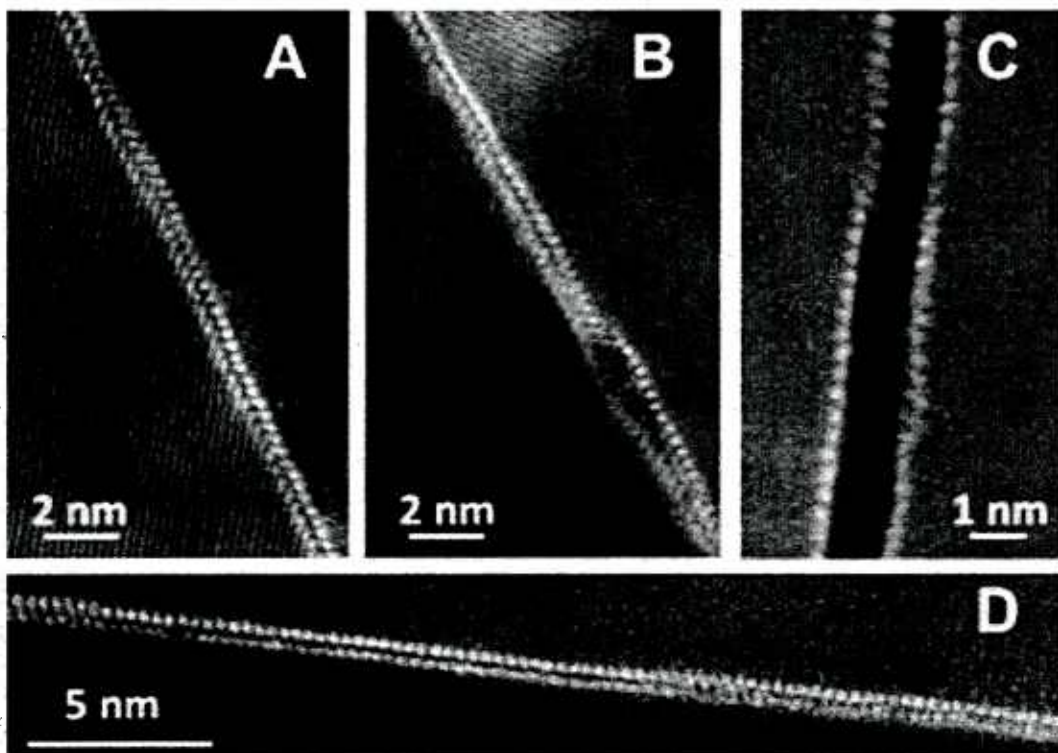




Figure 2.8: STEM HAADF images show 2 layers of Bi absorbed along the general GBs of a Ni polycrystal quenched from 700°C. (C) Weakly bonded Bi atoms could cause the boundaries to easily fracture between layers and thus embrittle the material. Presumably, decohesion of this GB occurred during TEM specimen preparation. (D) A bilayer interfacial phase similar character was observed in specimens quenched from 1100°C. [54]

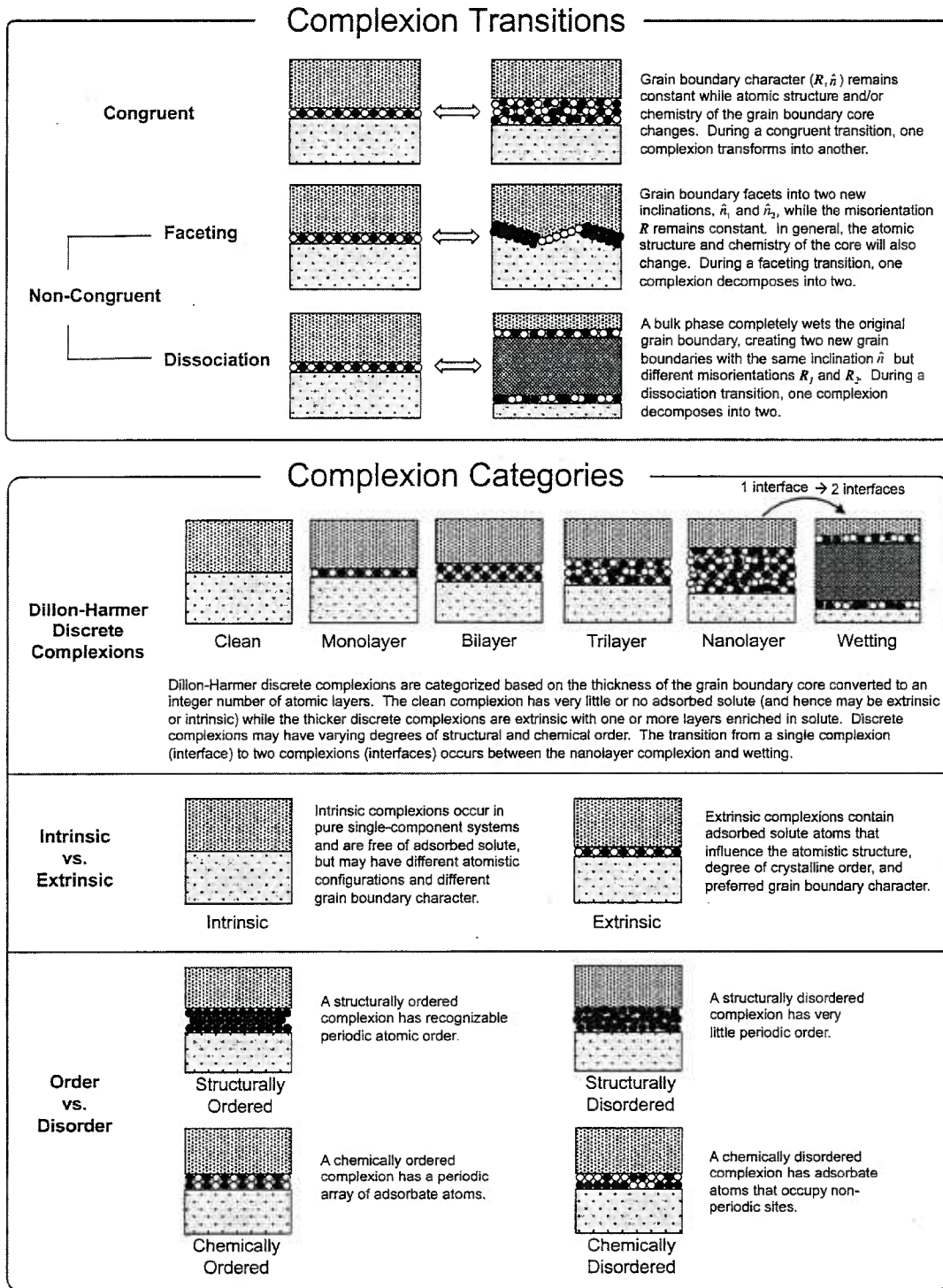


Figure 2.9: Schematic diagrams showing different types of complexion transitions and different ways of categorizing complexions. [46]

### ***2.3.2 Characterization of Complexions***

To characterize the structure and compositions of grain boundary complexions, techniques can be generally classified into two groups: direct method allows visualization of grain boundary structure and knowledge of chemistry and compositions across the grain boundaries, while indirect method measures the properties that depend on grain boundary structure and chemistry. It should be pointed out that the best approach to characterizing complexion transitions is to use a combination of both techniques. Detailed description can be found in Cantwell et al. [46] In the current work, direct method by using Transmission Electron Microscopy (TEM) and indirect method by using Atomic Force Microscopy (AFM) will be introduced.

#### ***2.3.2.1 Direct Characterization of Complexions by using TEM***

TEM has been widely used to characterize the structure and chemistry of the grain boundaries, which can provide atomic-scale images as well as compositional analysis with energy-dispersive X-ray spectroscopy (EDS) or electron energy loss spectroscopy (EELS). Moreover, with the development of aberration-corrected high angle annular dark field scanning transmission electron microscopy (HAADF-STEM), it enables new discoveries of grain boundary complexions. A schematic illustration of HAADF-STEM is shown in Figure 2.10. In STEM, the experimental configuration is similar to TEM but this time the electron beam is scanned over the specimen. By using a HAADF detector with a large inner radius, electrons are

collected which are not Bragg scattered. As such HAADF-images show little or no diffraction effects, and hence the intensity of the signal strongly depends on the average atomic number of the atoms in the sample, which is proportional to  $Z^{1.7}$ . Therefore, grain boundary segregation of high Z elements, compared with general low Z matrix, can be easily identified by using this technique. However, certain experimental conditions are required for a clear grain boundary complexion image. First the grain boundary plane needs to be parallel to the optical axis of TEM, which is called edge-on condition since just  $1.5^\circ$  away from edge-on condition, the grain boundary complexion can be submerged by overlapping from the adjacent grain. Second requirement is that at least one of the grains should align to a low index zone axis for a lattice image, which possibly reveals a disordered or ordered complexion. As suggested by Cantwell et al, [46] due to above restrictions, bicrystals with relatively high symmetry are frequently studied compared with general grain boundaries, which is difficult to achieve an edge on condition while simultaneously aligning the adjacent grain to a low index zone axis. However, since general grain boundaries tend to have higher grain boundary energy and thus are most likely to exhibit complexion transition, study on bicrystals alone could submerge the existence of complexion transition and generate biased results. Considering general grain boundaries have a complicated geometry and HAADF image is a 2 dimensional projection image, it is essential to know the dopant distribution and grain boundary structure parallel to the beam direction. By recording images at different defocus values, it is then possible to “Slice” through the sample in a similar way to that used in confocal optical microscopy. Figure 2.11 shows the basic principle of a though-

focal series imaging technique. The first image is taken with the electron beam focused in one particular plane. Then the focus is changed by a fixed amount and the second image is recorded. By repeating multiple times by changing fixed focus value, the information of samples at different Z height can be obtained, which are essential for a 3 dimensional grain boundary reconstruction. In summary, by using HAADF-STEM imaging combined with through focal series imaging technique, grain boundary adsorption of higher Z elements can be easily identified. It should be emphasized that combining different characterization techniques give a better understanding of the structure and chemistry of the grain boundary complexions, especially with the aid of computer simulations to interpret the TEM results and understand the mechanisms. For detailed theoretical background on HAADF and STEM, please refer to Pennycook et al. [62, 63]

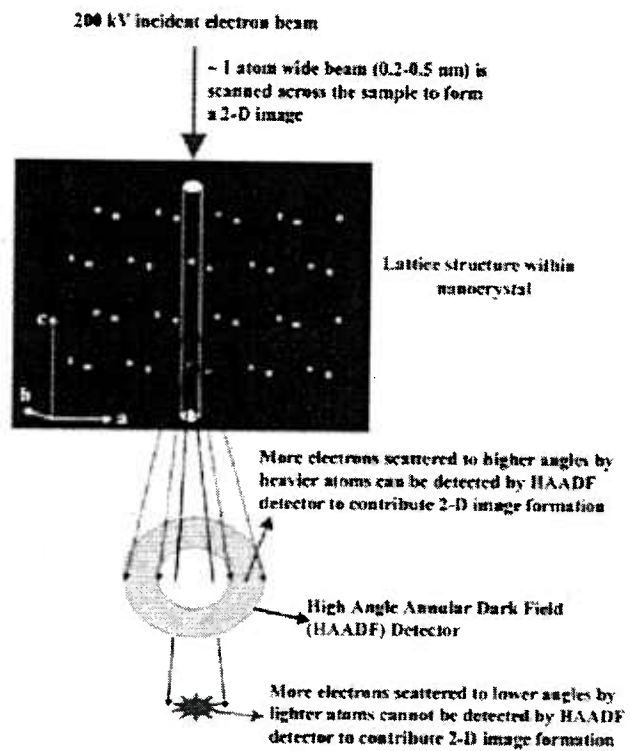


Figure 2.10: Schematic illustrations of HAADF-STEM imaging. [53]

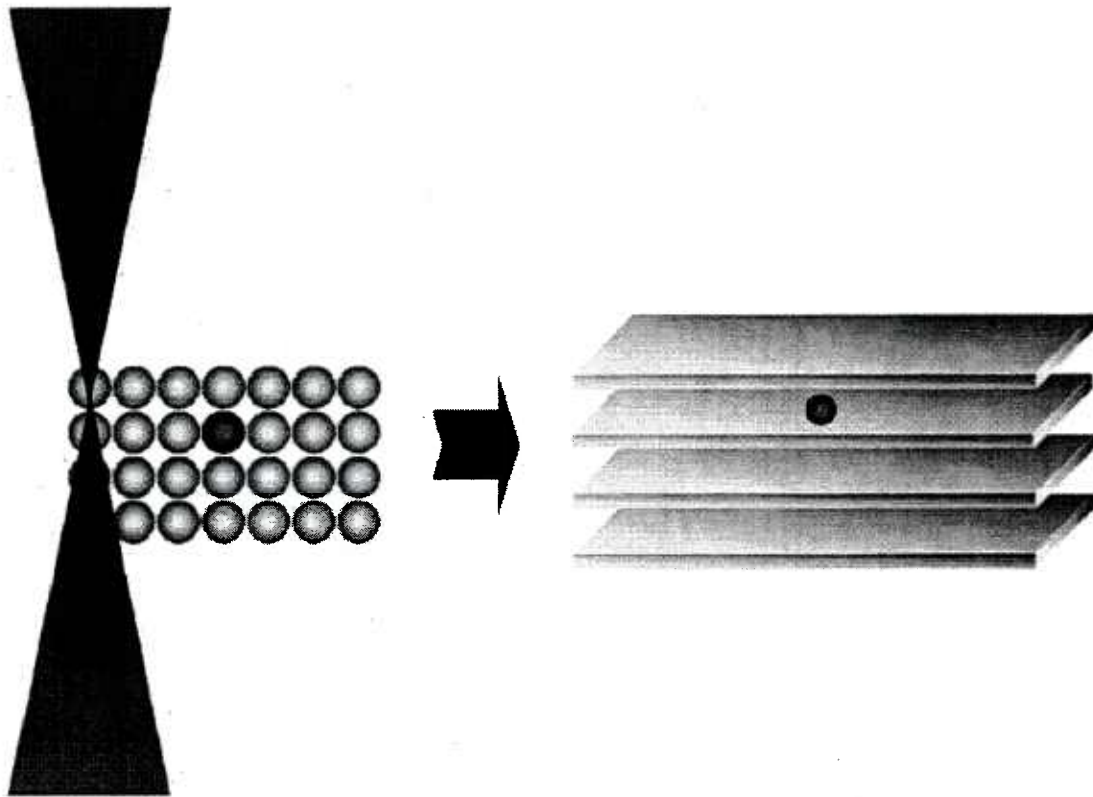


Figure 2.11: Sketch of the basic principle for focal series imaging. [61]

### 2.3.2.2 Indirect Characterization of Complexions by using AFM

It is generally known that a polished polycrystal has a flat surface. At an elevated temperature, the surface grows grooves where the surface meet grain boundaries, as shown in Figure 2.12. Mullins [35] established the model of this grooving process assuming only surface diffusion occurred. Local equilibrium at the triple junction implied that the surface and grain boundary tension balance each other. The relative energy of a grain boundary ( $\gamma_{gb}$ ) to the adjacent grain surface ( $\gamma_s$ ) can be expressed as a function of the dihedral angle ( $\Psi$ ), giving by:

$$\frac{\gamma_{gb}}{\gamma_s} = 2 \cos \frac{\Psi}{2}$$

(2.10)

By using AFM, it is easily to measure the height and width of a thermal groove and solve for the relative interfacial energy of the grain boundary. Moreover, the measurements can be conducted for many grain boundaries to obtain the mean dihedral angle and width of distribution to minimize the deviation from a number of assumptions such as isotropic surface energy and grain boundary is perpendicular to the surface.

Various studies have been shown that complexion transitions are associated with change in the grain boundary energy. [64, 65] Since it is difficult to measure the absolute grain boundary energy, instead, the relative grain boundary energy is measured to characterize the complexion transitions. One of the typical example as shown in Figure 2.13 depicted the relative grain boundary energy distributions for



two groups of grain boundaries in 100ppm Nd-doped alumina, which were normal and abnormal grain growth respectively. For each of the group, about 200 grain boundaries have been measured. The dihedral angle was obtained from thermal grooving measurement based on the equation 2.10. Based on previous studies, it suggested that the grain boundaries growing normally are likely to have a monolayer complexion, while the grain boundaries growing abnormally are likely to have a bilayer complexion. The results clearly indicated that the boundaries with a bilayer complexion have a larger mean dihedral angle, and hence a smaller average energy than that with a monolayer complexion. By comparing the relative energy of grain boundaries measured before and after a transition, the results will provide insights into the relative driving force for complexion transitions. It should be pointed out that the relative grain boundary energy is an average for many grain boundaries, not for a single grain boundary. By combining AFM measurements relying on statistical distribution with TEM that deal with single boundaries, a better characterization of grain boundary complexion is achievable.

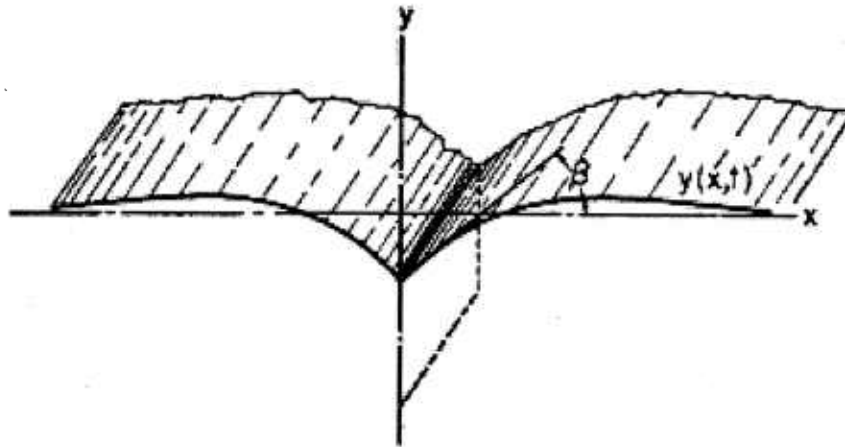


Figure 2.12: Section showing profile of ideal thermal groove (vertical exaggeration~5X) [35]

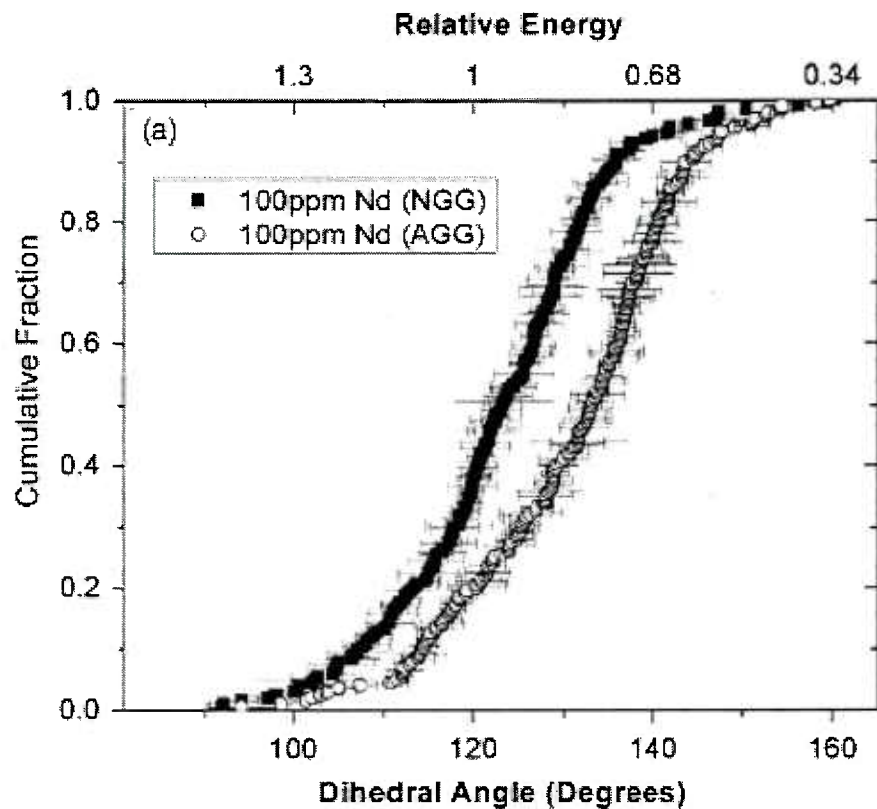


Figure 2.13: Cumulative distribution of dihedral angles in neodymia-doped alumina annealed at 1400°C with normal (monolayer complexions) and abnormal (bilayer complexions) grain boundaries. [64, 65]

### ***Chapter 3. Statement of Purposes***

The growth of protective alumina scales on  $\text{Al}_2\text{O}_3$ -forming alloys can be affected by the addition of reactive elements. While a number of theories concerning the “reactive element effect” have been proposed, a full explanation of this phenomenon is not yet available. The overall objective for this study was to conduct a systematic series of model experiments in order to elucidate the effect of  $\text{HfO}_2$  on oxygen grain boundary transport in alumina. The aim will be to better understand, tailor and control alumina scale growth in alloys.

The goal has been achieved by performing oxygen diffusion experiments on monolithic alumina/Ni composites, which involve the monitoring of spinel formation resulting from the oxidation of Ni marker particles that highlight the penetration of oxygen into a sample. More specifically, by varying  $\text{HfO}_2$  doping concentrations, we hope to better understand any blocking effects associated with dopant segregation to grain boundaries. Moreover, by exploring the effect of oxidizing temperature on oxygen grain boundary diffusion in  $\text{HfO}_2$ -doped alumina, we hope to develop correlation between grain boundary structure and oxygen transport property by using sub-angstrom Cs-corrected HAADF-STEM. This follows from work [32, 33, 46] that alumina can undergo discontinuous changes in interfaces transport properties associated with transitions in grain boundary complexions.

## ***Chapter 4. Experimental Procedure***

### ***4.1 Powder Processing***

The powder processing of alumina with various doping conditions have been performed carefully to reduce the chances of introducing additional impurities into the samples. Procedures such as doping, milling and drying were all performed in a class 1000 clean room. 250ml low-density polyethylene (LDPE) bottles (Fisher Scientific, Pittsburgh, PA) were used as powder containers due to their translucency for better visibility and chemical resistance to organic solvents. 400ml Chemware TFE Teflon dishes (Thomas Scientific, Swedesboro, NJ) were used to dry the powder or powder mixture due to its chemically inert, non-contaminating, heat and cold resistance and easy to clean. Shatter Resistant Infrared Heat Bulb (McMaster-Carr, Dayton, NJ) was used for lamp-drying the powder alcohol solution. Other labware include alumina milling balls ( $\phi=0.3\text{mm}$ , 99.9%, Union Process, OH), strainers, funnels, magnetic stir bars, Saint-Gobain Chemware PTFE fluoropolymer resin policemen (Fisher Scientific, Fairlawn, NJ), alumina tubes, alumina crucibles and alumina rectangular trays (99.8%, Vesuvius McDanel, Beaver Falls, PA). It should be pointed out that different sets of labware for processing powder or powder mixture with different doping types were used to minimize cross-contamination. The procedure to clean the labware is described as following steps:

1. Crucibles and labware were placed inside the LDPE bottles, if the labwares were too large, a barrel was used.
2. The bottles or barrel were degreased by immersing in reagent grade trichloroethylene (Fisher Chemical, Fairlawn, NJ) for 1 hour.
3. The used trichloroethylene should be poured into glass bottle labeled for future waste collection.
4. The bottles or barrel were filled with in grade acetone (Pharmco, Brookfield, CT) to remove the residual trichloroethylene for 1 hour.
5. The used acetone should be poured into glass bottle labeled for future waste collection.
6. The bottles or barrel were finally filled with 190 proof ethanol alcohol (Pharmco, Brookfield, CT) to remove the residual trichloroethylene for 1 hour.
7. The used ethanol alcohol should be poured into sink with the water tap on.
8. The bottles or barrel were then rinsed by deionized water for three times to get rid of residual alcohol.
9. The bottles or barrel were placed under the hood inside the clean room overnight for drying.

#### ***4.1.1 HfO<sub>2</sub>-doped Alumina***

The starting powders were high purity (>99.99%)  $\alpha$ -alumina powder (Sumitomo AKP-HP) supplied by Sumitomo Chemical Co. LTD. (Tokyo, Japan). And high purity (99.998%) nickel oxide powder (NiO) was obtained from Alfar Aesar (Ward Hill, MA). The nickel oxide powder was first wet-milled in semiconductor grade (>99.9%) ethanol (Pharmco, Brookfield, CT) to reduce its particles size. Approximately 30vol% alumina milling balls were added to the bottle. The mixture was then milled for 24h. After milling, a high-density polyethylene (HDPE) strainer was used to separate the milling balls from the slurry. The slurry obtained through the strainer was placed in a Teflon dish along with a PTFE coated magnetic stirring rod. It was stirred under a heat lamp in a laminar flow fume hood in the clean room. The ethanol was allowed to evaporate under the lamp for 24 or 48 hours. The dried powder was then crushed using cleaned policemen or alumina pestle to break up any agglomerates and finally stored in a LDPE bottle for later use.

In the current work, hafnium dinitrate oxide ( $\text{HfO}(\text{NO}_3)_2$ , 99.9% (metals basis excluding Zr), Zr <0.1%, 10% w/v aq. soln.) was used to prepare HfO<sub>2</sub>-doped alumina samples. This liquid was mixed with ultra-pure  $\alpha$ -Al<sub>2</sub>O<sub>3</sub> powder to get various doping levels including 100ppm, 200ppm, 300ppm, 500ppm, and 2000ppm.

(Atomic ratio of [Hf]/[Al]) The mixture was wet-milled in ethanol for 24 hours and dried under the lamp.

The powder was then put in an alumina crucible and calcined at 750°C for 7h in a box furnace in air to decompose the hafnium dinitrate to hafnium oxide and also to remove any residual methanol. After calcinations, 1.5 wt% of the nickel oxide was wet-milled for 24 hours with the powder again to achieve a final volume fraction of 0.5 vol% Ni. The reason for selecting this volume amount of Ni is described in Cheng et al. [15] The slurry was dried, crushed and then put into the graphite die for sintering.

#### ***4.1.2 Other Alumina/Ni Composites***

Lanthanum (III) nitrate hexahydrate ( $\text{La}(\text{NO}_3)_3 \cdot 6\text{H}_2\text{O}$ , 99.999% (REO)) was used to prepare 500ppmHfO<sub>2</sub>-500ppmLa<sub>2</sub>O<sub>3</sub>-codoped alumina samples. These two dopants were selected due to initial results that suggested that Hf-La co-doping reduced Ni outward diffusion to a greater extent than the single dopants. These results are described in Appendix C . The co-doped samples were then prepared through the same procedure and under the same heat-treatment conditions as described in Section 4.1.1.

#### ***4.2 Hot-pressing/ Spark Plasma Sintering***



Hot pressing and spark plasma sintering were applied to obtain fully dense samples from the initial powder mixtures. A water-cooled vacuum furnace (Astro, Thermal Technology Inc., Santa Rosa, CA) that uses graphite elements and contained graphite insulation was used for hot pressing. Different graphite dies (HPD-2) with 1-inch inner diameter and 3 inch outer diameter (Poco Graphite, Decatur, TX) were used for different types of dopants respectively. The powder and die assembly is shown schematically in Dillon's dissertation [48]. Spark plasma sintering (SPS), which is a revolutionary high-speed powder consolidation process, utilizes high amperage pulsed DC current to activate the consolidation and reaction sintering of materials as shown schematically in Figure 4.1. The clear benefit of SPS is the significant savings of time and energy, and the ability to retain nanostructures at relative high temperature. SPS Model 10-4 (Thermal Technology Inc., Santa Rosa, CA) as shown in Figure 4.2 was used in the current study. Graphite dies with 20mm inside diameter and 50 mm outside diameter plus a pyrometer hole were used. (Thermal Technology Inc., Santa Rosa, CA). Due to the great heat loss during the SPS, relative to using a thermocouple, monitoring the temperature by pyrometer is more stable and precise. Note that the working temperature for the pyrometer is greater than 600°C. The operational procedure for hot pressing and spark plasma sintering is very similar and can be summarized as below:

1. The graphite cap was placed upside down on the table in the clean room.
2. The inside of the graphite die was then wrapped with a piece of graphite foil (99.8%, Alfa Aesar, Ward Hill, MA) .

3. A spacer was placed above the cap.
4. A piece of graphite foil was put on top of the spacer.
5. The graphite die was then placed above the spacer and cap.
6. The die was filled with the proper amount of dried powder. (For SPS, the optimum amount of powder is around 8 grams due to the design of alignment of pyrometer hole. Generally, based on the geometry of the die assembly and density of pure alumina, a desired sample thickness can be roughly calculated based on the amount of powder put into the die. )
7. A second piece of graphite foil was placed on top of powder.
8. Another graphite spacer was put on top of the foil.
9. A graphite punch was pressed flat into the die.
10. 40 MPa was applied by using a uniaxial hydraulic press (Carver, Menomonee Falls, WI) to consolidate the powder.
11. The assembly was then put into the furnace. For hot pressing, it was placed in the furnace between the two pressing rams and tested under the pressure applied while the furnace is open. For SPS, an initial 10MPa pressure was applied to make assembly conductive and adjustment of graphite die position to align the pyrometer hole for monitoring temperature is essential.
12. Program was then set up. (Unit for pressure, temperature and time should be checked before each run)
13. The assembly was first heat treated for 10 hours at 500°C for hot pressing and 3 hours at 650°C for SPS in a flowing 4% H<sub>2</sub>-Ar atmosphere to reduce the NiO to metallic Ni particles. The chamber pressure was less than 60 millitorr

for hot pressing or less than 6 millitorr for SPS. After reducing, all the samples were then hot pressed at 1400°C for 3h or SPSed at 1400°C for 20 minutes.

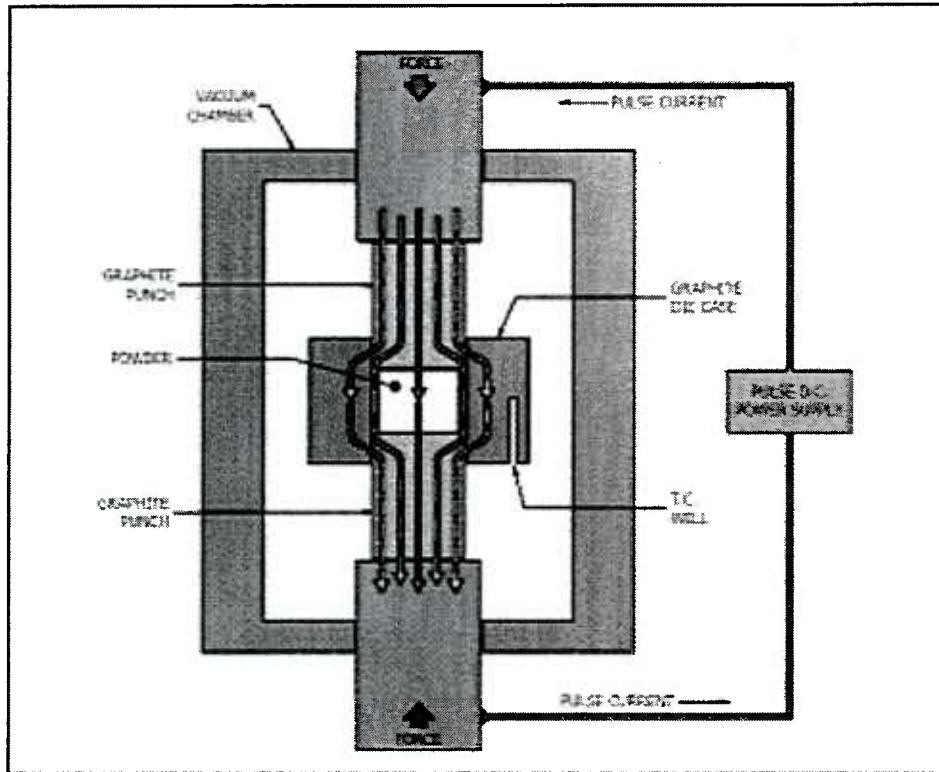


Figure 4.1: Basic configuration of a Spark Plasma Sintering (SPS) Machine [49]

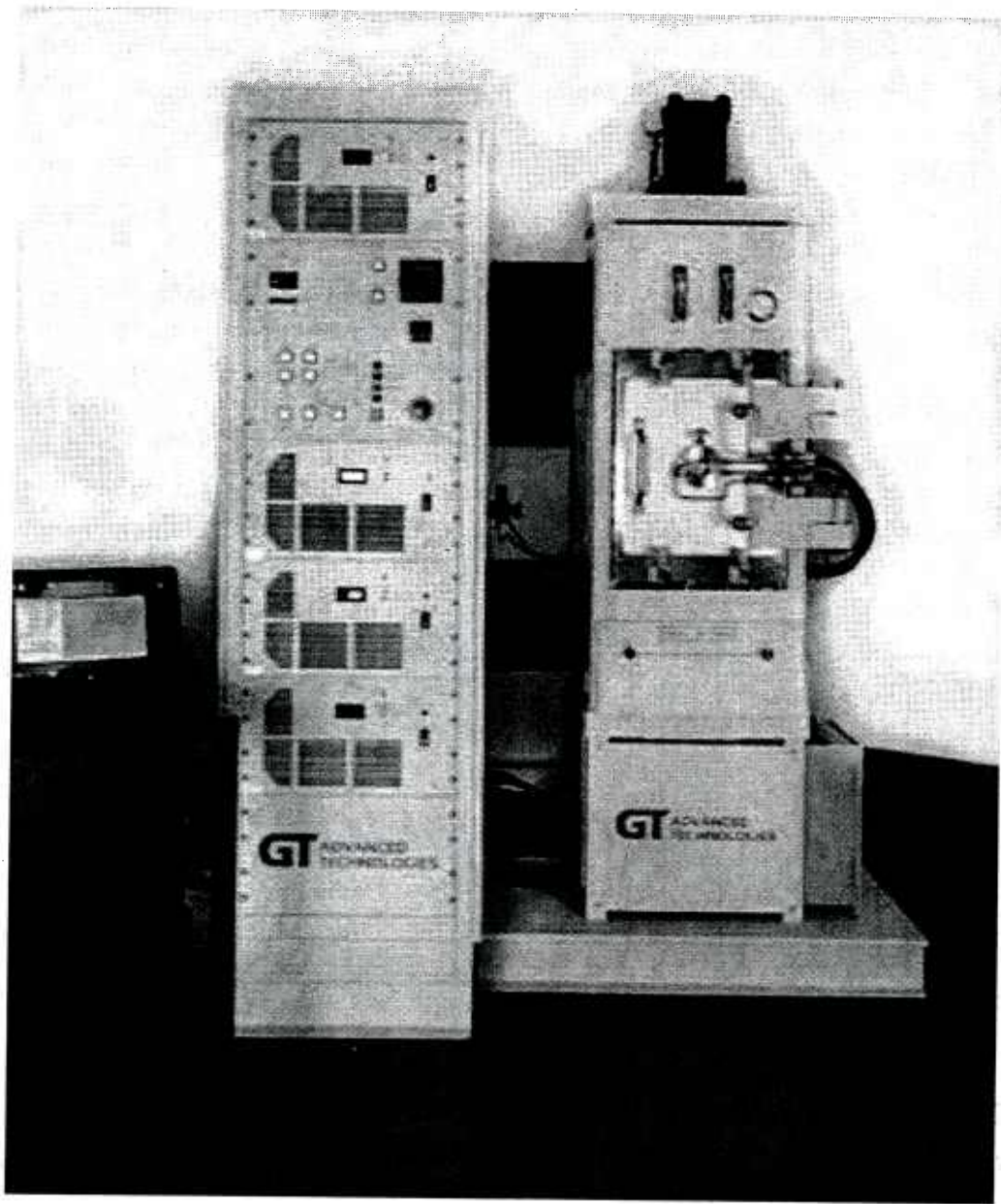


Figure 4.2: Spark Plasma Sintering (SPS) Model 10-4 used in the current study  
[50]

### ***4.3 Sample-cutting***

The as-hot-pressed and as-SPSed samples were cut into smaller pieces for later oxidation experiments. Cutting was performed using a high-speed saw (Accutom 5, Struers, Westlake, OH) fitted with a diamond-coated blade (Smart Cut, Westlake OH). A layer approximately 2mm thickness was removed from the sides and top and bottom to minimize the effect of any carbon contamination. Then the samples were cut into smaller rectangular pieces, with sizes around  $4 \times 4 \times 2\text{mm}^3$  depending on the experimental conditions.

### ***4.4 Sample-polishing***

Samples were mechanically polished using an automatic polisher, either Abrapol (Struers Inc., Cleveland, OH) or mainly Sapphire 550 (Mager Scientific Inc., Dexter, MI) depending on their availability. The detailed procedure is listed below:

1. The samples were mounted by using epoxy, which usually is made of the mixture of 10 parts of Epoxicure Resin and 1 part of Hardener by weight, (Buehler, Lake Bluff, IL).
2. The samples were then placed in a hood for 24h to make sure the mounts are hard enough before polishing. If not, the mounts should be put in an oven for 2h at  $65^\circ\text{C}$  and then allowed to cool down to room temperature in the hood.

3. Sample edges were chamfered using a 240-grit SiC paper. This reduces the likelihood of damage to the polishing cloth during subsequent polishing.
4. Samples were first ground using a 400-grit SiC paper to remove the residual epoxy on the surface. The duration should be kept less than 10 seconds and the force applied per sample is around 25 Newton. Too long time and/or too large force can greatly damage the sample's surface, which is generally never back to flat any more. It is also noteworthy that three or six samples can be used one time to achieve a balanced load of the polishing machine head.
5. After grinding, the samples were polished on a no nap woven polyester polishing cloth (MD-Plan) (Struers, Bellerup, Denmark) with 15  $\mu\text{m}$  diamond paste, followed by 9  $\mu\text{m}$  diamond paste. A 40 Newton load per sample and 3 minute polishing time for each abrasive size is a safe choice. Switching to the next (smaller) abrasive size is undertaken when there are no signs of improvement in the surface quality under an optical microscope. After each step, the samples need to be cleaned under running water using cotton to prevent cross contamination between different abrasives.
6. Samples were continuously polished on a woven satin polishing cloth (MD-DAC) (Struers, Bellerup, Denmark) with 3  $\mu\text{m}$ , followed by 1  $\mu\text{m}$  diamond paste.
7. Finally, samples were put in a vibratory polisher, Vibromet I (Buehler, Lake Bluff, IL) that contains 0.05  $\mu\text{m}$  colloidal silica slurry for about 1 hour. The vibrating polisher is essential to remove the surface damage created by previous polishing steps.

8. and achieve the high surface quality needed for EBSD with minimum

After polishing, the next step is getting the samples out of the epoxy without damaging the flat surfaces. The most effective way was to heat the mount containing the sample immersed in the deionised water on a hot plate until the epoxy just becomes soft. By carefully using tweezers without touching the finished surfaces, samples can be separated from the epoxy.

#### ***4.5 Sample-cleaning***

The polished samples were ultra-sonically cleaned using acetone and then ethanol for 30 minutes. And then they were rinsed with D.I. water and dried in the Isotemp oven with temperature 100°C for 30 minutes. Clean samples were stored in desiccators for later use.

#### ***4.6 Oxidation of Samples***

HfO<sub>2</sub>-doped alumina/Ni composites were placed in an alumina rectangular tray, which was then put into the tube furnace. The temperature was calibrated using a Type B thermal couple (Omega Engineering, Inc., Stanford, CT). Oxidation of the samples was carried out in an oxygen-flow environment (Oxygen Compressed, Ultra High Purified Grade, Airgas, Pennsylvania) in the temperature range of 1150°C to 1400°C for a specified period of time with a fixed flow rate around 200 cm<sup>3</sup>/Min.

#### ***4.7 TEM Sample Preparation***

Thin foil TEM samples were prepared by using a focused ion beam (FIB) (DB235, FEI company, Hillsboro, OR). The ion beam applied was 30 kV and the electron beam was 5 kV. The basic procedure is described as follows:

1. A bulk sample was sputter coated (E5100, Polaron Equipment Limited, Hertfordshire, England) with gold-palladium for 1 min to minimize charging effect.
2. A 2  $\mu\text{m}$  thick platinum layer was deposited on an area of interest to protect the underlying grain boundary area from ion bombardment. A series of trench making and cleaning procedures were carried out on both sides of the sample. Before lifting out, edges of the sample were cut off, although a small connection was left on one edge. Images depicting the sample at different steps of the thinning process are shown in Figure 4.3.
3. The thin section sample was then cut and attached to a tungsten internal manipulator (Omniprober 100.7, Omniprobe Inc., Dallas, TX). With careful adjustment of the manipulator, the sample was removed from the bulk and attached to a Mo grid (Omniprobe Lift-Out Grids, Mo with 3 posts, Ted Pella, Inc.) by depositing a layer of platinum that connected the sample and the grid. Mo grids are used rather than conventional Cu grids because the Hf  $\text{Mo}\alpha$  peak



overlaps with Cu K $\alpha$  peak. Figure 4.4 shows the sample lifted out by manipulator ready to be attached to the Mo grid by using Pt deposition.

4. The sample was continuously thinned under a progressively lower Ga ion current from 500pA, 300pA, and 100pA with  $52^{\circ} \pm 1^{\circ}$  angles. The optimum thickness of the sample should be less than 100nm. In most cases, the thinning process was terminated when the sample showed signs of bending, and/or the platinum protective layer was removed. To remove the residual damage caused by the high-energy (20keV) Ga beam, ultra-low energy ion beam milling was conducted. With this low energy ion source (Fischione Model 1040 NanoMill, Fischione, Export, PA), as shown in Figure 4.5, sample surface amorphization, and ion implantation or redeposition could be minimized. The general rule of selecting proper parameters can be described as follows: If the starting thickness of the sample is around 100-200nm thick, use 1500eV/130pA on Faraday Cup with +9 degree in a  $15\mu\text{m} \times 15\mu\text{m}$  raster for 20 minutes for initial thinning. Repeat this cycle with -9 degree; check the sample and image quality in the TEM. When an improvement such as better contrast and/or less amorphous area is observed, repeat these steps at 900eV to continually improve sample quality.
5. Before examining by the TEM, the sample was cleaned by plasma of argon and oxygen in plasma cleaner (Model 1020 Plasma Cleaner, Fischione, Export, PA) for 10 min.

It should be emphasized that a high-quality TEM sample with minimum surface damage layer and thickness less than 100nm is essential for advanced TEM imaging and analysis.

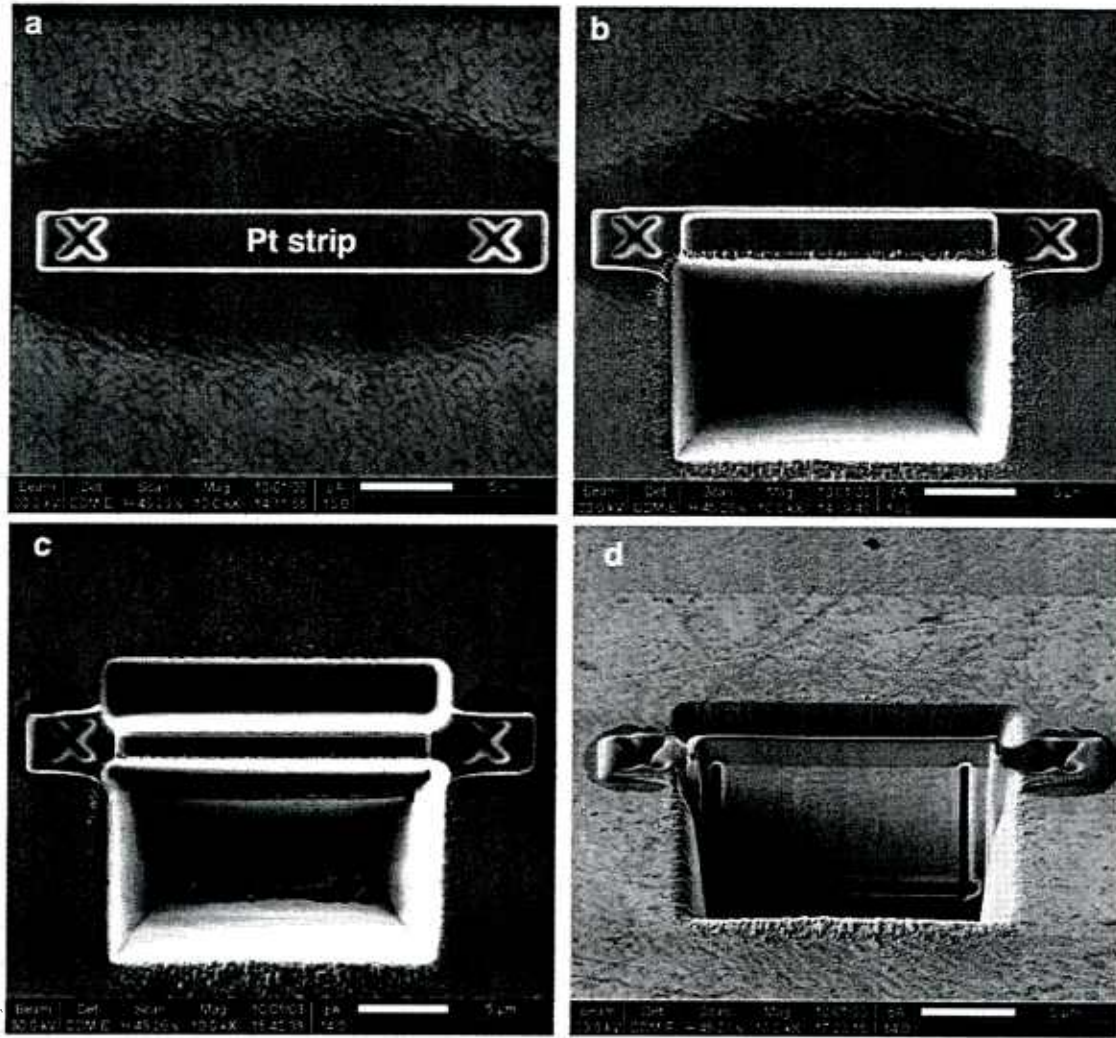


Figure 4.3: FIB image at different steps: a) Pt layer deposition b) Trench on one side c) Trench one the other side d) Edges cut off and small connections with the bulk sample remained [51]

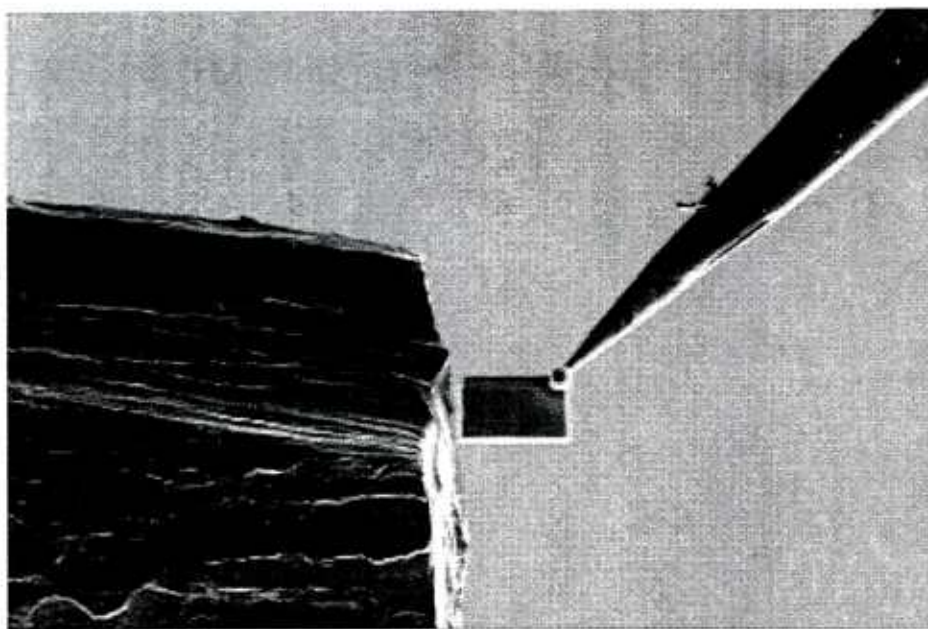


Figure 4.4: Alumina sample lifted out by manipulator before attachment to the middle column of the Mo grid

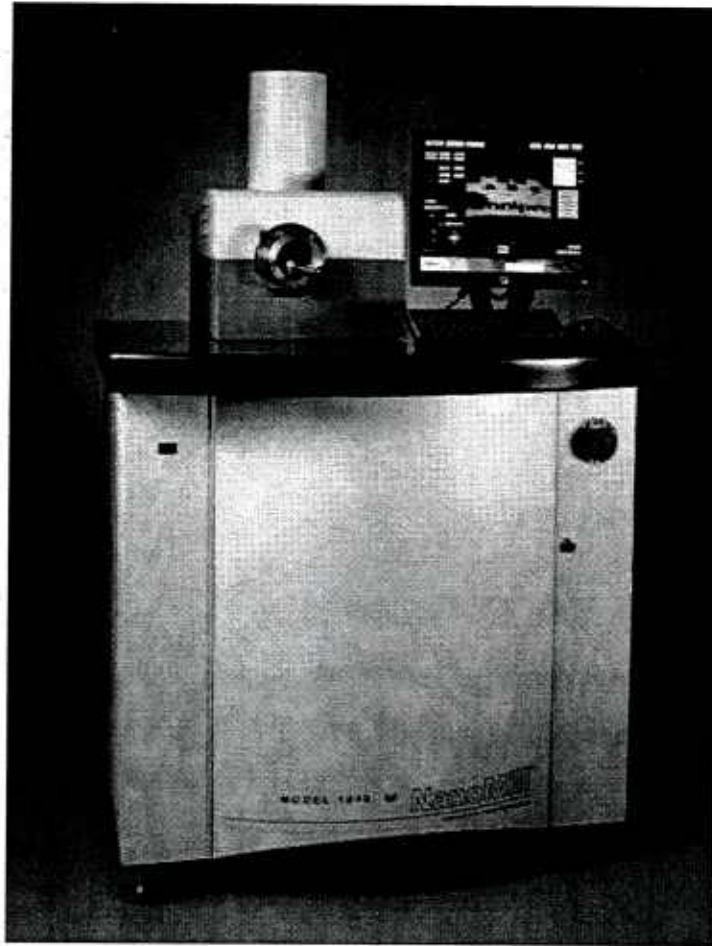


Figure 4.5: Fischione's Model 1040 NanoMill TEM specimen preparation system  
[52]

#### 4.8 Grain Size Measurement

After polishing and oxidation, the average grain size was determined by using the linear intercept method. [45] Measurements were carried out using a transparent mask containing 10 random lines with fixed 10cm length overlaid onto an image of a microstructure as shown in Figure 4.6. The mean linear intercept length is the average length of a line segment that crosses a certain number of grains, which is proportional to the equivalent diameter of a spherical grain. For each sample condition, around 600 to 800 grains were counted for statistic consideration. The average grain size,  $\bar{G}$ , and the standard deviation,  $\Delta G$ , were calculated as follows:

$$\bar{G} = \frac{1}{10n} \sum_{i=1}^{10n} G = \frac{1}{10n} \sum_{i=1}^{10n} \frac{1.5L}{N_i \times M} \quad (4.1)$$

$$\Delta G = \sqrt{\frac{\sum (G - \bar{G})^2}{10n - 1}} \quad (4.2)$$

Where L is the length of the random line drawn in the mask (L=10cm in this work),  $N_i$  is the number of grains, M is the magnification and n is the number of the images taken. For n is greater than 10, the error of the standard deviation will be about 10% at a 95% confidence level. 1.5 is a conversion factor for 3 dimensional grain size obtained from 2 dimensional grain intercept size since in random sections, the grains appear smaller than their maximum dimension.

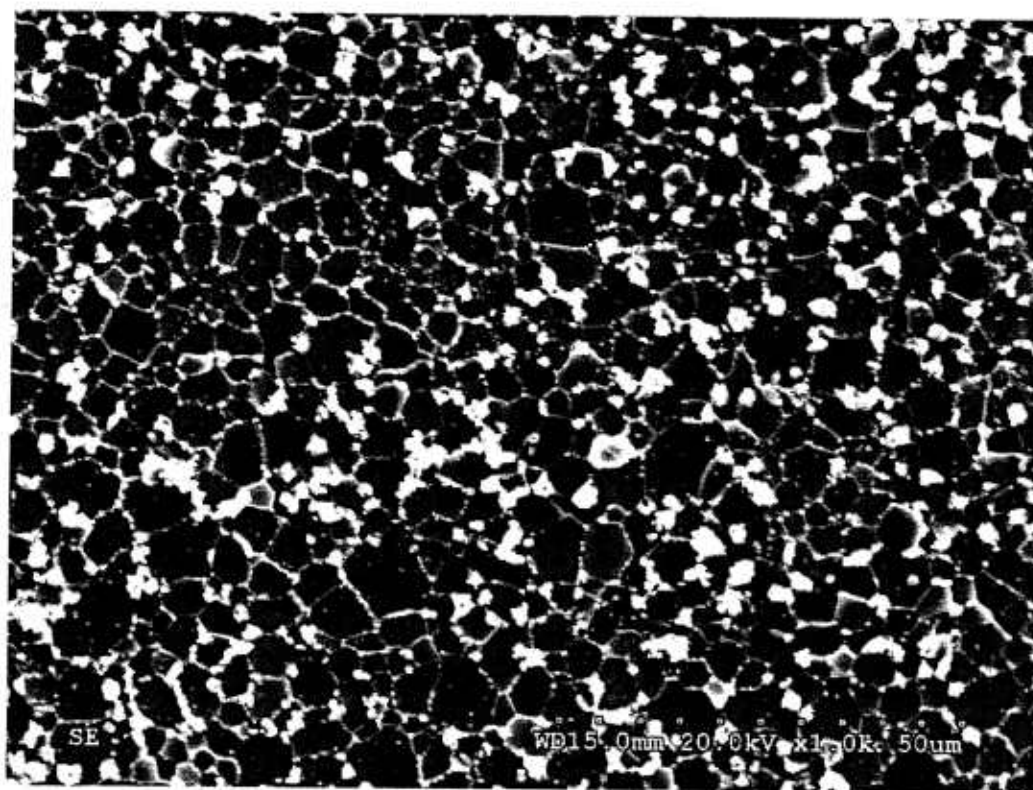


Figure 4.6: Free surface of 500ppm HfO<sub>2</sub> doped alumina/Ni oxidized at 1400 for 5h

#### ***4.9 Diffusion Depth Measurement***

The depth of oxygen transport front in alumina was measured from Scanning Electron Microscopy (SEM) images by using backscattered electrons (BSE) of the cross sections of the oxidized samples. The detailed procedure used to measure the penetration depth will be discussed in Chapter 5. The microscope used in the current work was mainly a Schottky-field emission source Hitachi S4300 N (Hitachi High Technologies America, Inc., Peabody, MA) with an accelerating voltage of 20kV. In order to prevent charging, the samples were coated with Iridium for 15 seconds (EMS 575 Turbo Sputter Coater, EMS, Hatfield, PA). The thickness of the coating is less than 5nm.

#### ***4.10 Texture Analysis***

The in-plane orientation and grain boundary misorientation analysis between different samples were conducted by using Electron Backscatter Diffraction (EBSD). For typical EBSD measurement, a flat/polished crystalline specimen after vibratory polishing is placed inside the SEM chamber (Hitachi S4300 N, Hitachi High Technologies America, Inc., Peabody, MA) at a highly tilted angle ( $\sim 70^\circ$  from horizontal) towards the diffraction camera to increase the signal in the resultant EBSD pattern. A very thin Ir coating (less than 5 seconds (1nm)) has been applied on the surface to reduce the charging. Since the EBSD signal is generated from the near

surface, too thick a coating would result in a degraded signal. Moreover, a high accelerating voltage, large aperture and condenser lens were also chosen to obtain an EBSD pattern with good signal to background ratio.

#### ***4.11 Grain Boundary Characterization by Using TEM***

Transmission electron microscopy (TEM) was performed using a 200kV JEOL 2000FX (2000FX, JEOL USA Inc., Peabody, MA) with a lanthanum hexaboride source. The 2000FX was mainly used for checking the sample quality after nanomilling. High-resolution images were obtained using either the JEM-2200FS or JEM-ARM200CF. JEM-ARM200CF is an atomic resolution transmission electron microscope operating at a maximum accelerating potential of 200kV that features a cold-field emission source. A third-order aberration corrector near the sample allows higher beam currents to be focused with the best resolution of 0.08nm. High-angle annular dark-field scanning electron transmission microscopy imaging (HAADF-STEM), which is sensitive to variations in atomic number, has been performed to characterize  $\text{Hf}^{4+}$  ions segregating in the alumina grain boundaries, (the atomic number of Hf is 72 and that of Al is 13). In order to obtain clear grain boundary structure images, it is essential to have the grain boundary aligned closed edge on and tilt one grain to a low index zone to minimize the effect of overlapping from the adjacent grains and show a better lattice fringe contrast. Moreover, simulation of HAADF-STEM images was implemented by the fast Fourier transform multi-slice method, using the xHREM software suite.



#### ***4.12 Thermal Grooving Measurement by Using AFM***

To study whether doping affects the grain boundary energy, thermal grooving experiments were performed where the groove profiles were measured by AFM. An analysis due to Mullins was then used to infer the distribution of relative boundary energies in both undoped and doped samples. In the current study, undoped, 500ppm HfO<sub>2</sub>-doped, 500ppm Y<sub>2</sub>O<sub>3</sub>-doped and 500ppm La<sub>2</sub>O<sub>3</sub>-doped alumina have been prepared by following the same powder processing methods described previously. It should be pointed out that no nickel was added in these samples since the presence of nickel second phase particles on the free surface results in rapid blunting of the AFM tips. All the samples have been hot pressed at 1400°C for 3 hours at 45MPa. The samples were then cut into small cubes with 1mm length and polished up to 0.05μm colloidal silica. The samples were then annealed at 1500°C for 3 hours in the tube furnace in vacuum. The polished free surface after annealing has been measured in Dimension 3000 (Veeco, Plainview, NY) operating in tapping mode. The tips are BudgetSensors Tap3000 cantilever (Innovatie Solutions Bulgaria Ltd., Sofia, Bulgaria), which are micromachined monolithic silicon and have a tip height around 17μm and tip radius smaller than 10nm. To minimize the error due to tip wear, the tip was replaced after collecting 10 images for each sample. The width and height of thermal groove were measured by using WSxM software (Nanotec Electronica, Tres Cantos, Spain). 200 grain boundaries were randomly selected for relative grain boundary energy measurement. One of the typical images obtained by AFM for undoped alumina is shown in Figure 4.7. Line profile can be drawn normal to the

selected grain boundary to measure the groove height  $W$  and depth  $d_1$  and  $d_2$  on each side. The dihedral angle  $\Psi_s$  can be calculated giving by:

$$\Psi_s = 180^\circ - \tan^{-1}\left(\frac{4.73 \times d_1}{W}\right) - \tan^{-1}\left(\frac{4.73 \times d_2}{W}\right)$$

(4.3)

Then the cumulative distributions of dihedral angle and energy were obtained.

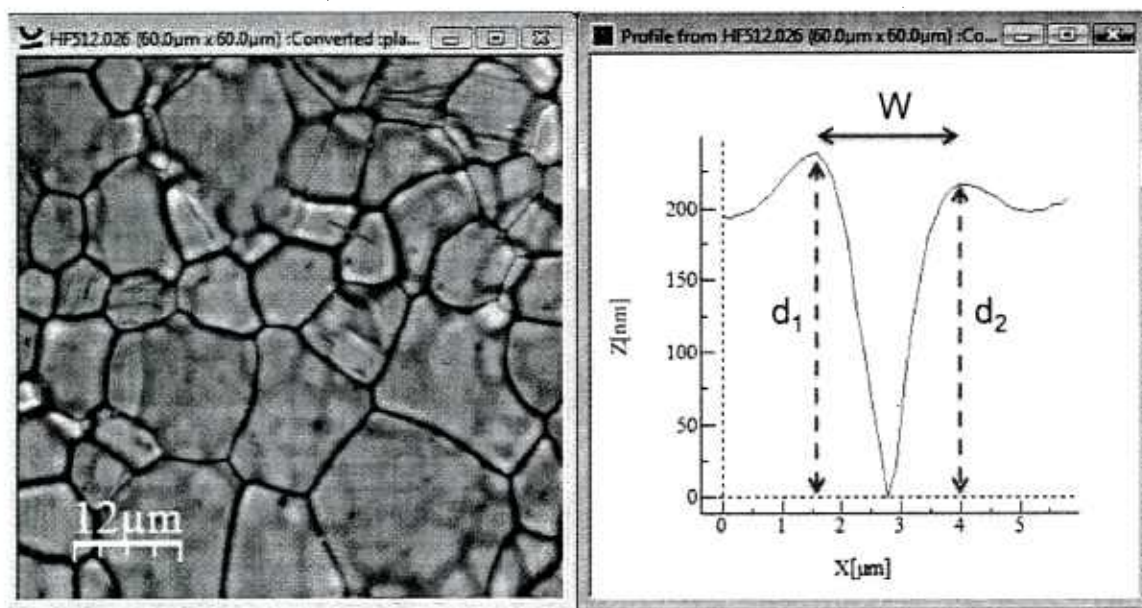


Figure 4.7: AFM image showing surface topography of undoped alumina sample annealed for 3 h at 1500°C (LHS). Depth profile for selected grain boundary section as indicated by green arrow (RHS).

## ***Chapter 5. Results and Discussions***

This chapter summarizes the results of diffusion studies in HfO<sub>2</sub>-doped alumina/Ni composites, in particular the role of doping levels and oxidation temperature.

### ***5.1 The Effect of HfO<sub>2</sub> Doping Concentration***

#### ***5.1.1 Microstructure***

Fig 5.1 represents a typical SEM image of a polished cross section of 500ppm HfO<sub>2</sub>-doped alumina oxidized at 1400°C for 60 hours. By using BSE imaging and EDS analysis, several phases can be seen clearly in the microstructure. The BSE signal scales with atomic number, hence the dark matrix is Al<sub>2</sub>O<sub>3</sub>, the metallic Ni particles exhibits the brightest contrast and the gray phase is NiAl<sub>2</sub>O<sub>4</sub>. The extent of the oxidation zone, as delineated by the presence of spinel second phase was visually well defined. All the phases have been further verified by using Transmission Electron Microscopy. Microstructurally, the appearance of the oxidized and non-oxidized regions was similar for all the samples, however the presence of HfO<sub>2</sub> second phase particles depended on the doping level.

Figure 5.2 (a) ~ (e) shows representative microstructures (taken from within the oxidized layer) of samples oxidized at 1400°C with doping levels ranging from 100ppm to 2000ppm. For 100ppm, there are no HfO<sub>2</sub> second phase particles.. For

doping levels of 500 ppm and higher, numerous  $\text{HfO}_2$  particles can be observed clearly. For the 200ppm and 300ppm samples, the number density of  $\text{HfO}_2$  particles is much lower. The composition of the  $\text{HfO}_2$  phase was verified by both EDS and TEM. From the microstructure, it is noteworthy that 300ppm has fewer  $\text{HfO}_2$  particles than 200ppm, which is unexpected. We believe the main reason is due to a grain size effect, which is to be addressed later. The current results suggest that the solubility limit for  $\text{HfO}_2$  in  $\text{Al}_2\text{O}_3$  is somewhere between 100ppm and 200ppm. The low solubility of  $\text{HfO}_2$  can be rationalized with the degree of size mismatch with  $\text{Al}^{3+}$  and different charge.

It is also noteworthy that voids have been observed inside the oxidized region, which we believe is correlated with Ni outward diffusion. The voids cannot be attributed to the spinel formation, since oxidation of Ni particles to spinel leads to a volume expansion. All the samples exhibited  $\text{NiAl}_2\text{O}_4$  spinel on the free surfaces, which formed presumably by the oxidation of Ni that had already existed and/or had diffused outward to the surface. Free surfaces for 500ppm  $\text{HfO}_2$  doped and undoped samples at  $1300^\circ\text{C}$  have been shown in Figure 5.3. For undoped samples, the spinel formed initially at the alumina grain boundaries and then developed into a continuous network. Previous work by Cheng et al. [15] compared the behavior of samples both with and without the spinel layer, and verified that the surface spinel layer did not have a measurable effect on the thickness of the oxidized region. For the 500ppm  $\text{HfO}_2$  doped sample, the volume fraction of surface spinel is much less than for the undoped alumina. This suggests that the  $\text{Hf}^{4+}$  ions also retard the outward diffusion of

Ni; whether this in turn affects the thickness of the oxidized region will be discussed later.

From the free surface plot, the average grain size can be obtained by using linear intercept method. In table 5.1, a summary of the grain size of samples with various doping levels oxidized at 1400°C is included. More than 800 grains have been measured for each doping level and oxidizing time, the standard deviation was used as the error. There is no obvious grain size change and abnormal grain growth for each doping levels after long time oxidation. In general, the average grain size is around 3~5 $\mu\text{m}$  except for the 200ppm samples, which has a much larger grain size mainly induced by a higher plasma sintering temperature due to a processing variation. The effect of grain size on the current work will be addressed in the next section.

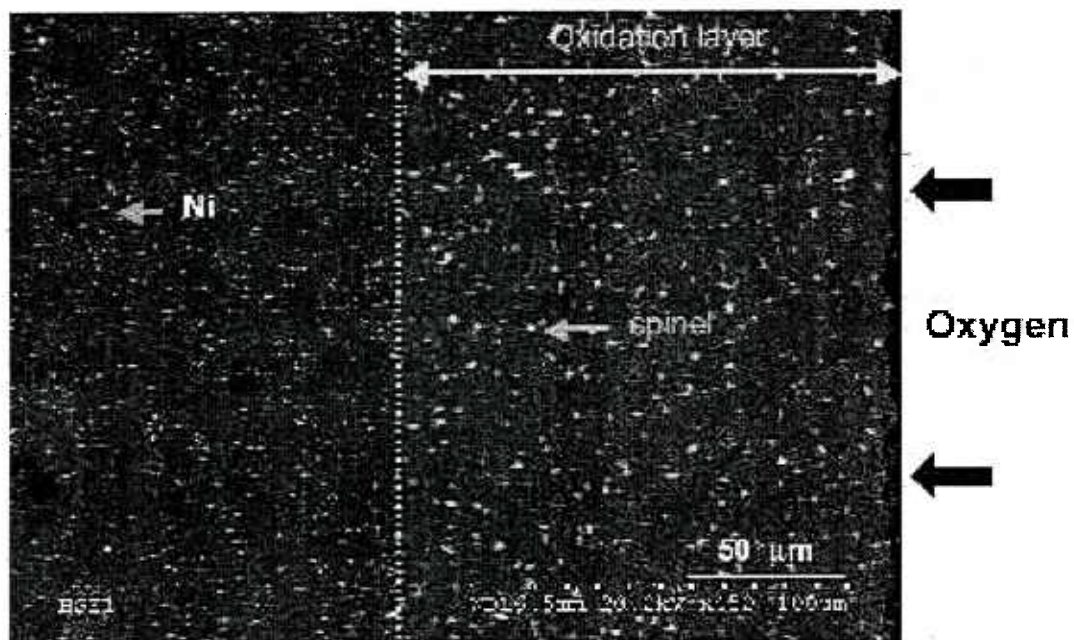


Figure 5.1: Scanning electron micrograph showing the cross section of the 500ppm HfO<sub>2</sub>-doped Alumina with 0.5vol%Ni after oxidation for 60hrs at 1400°C

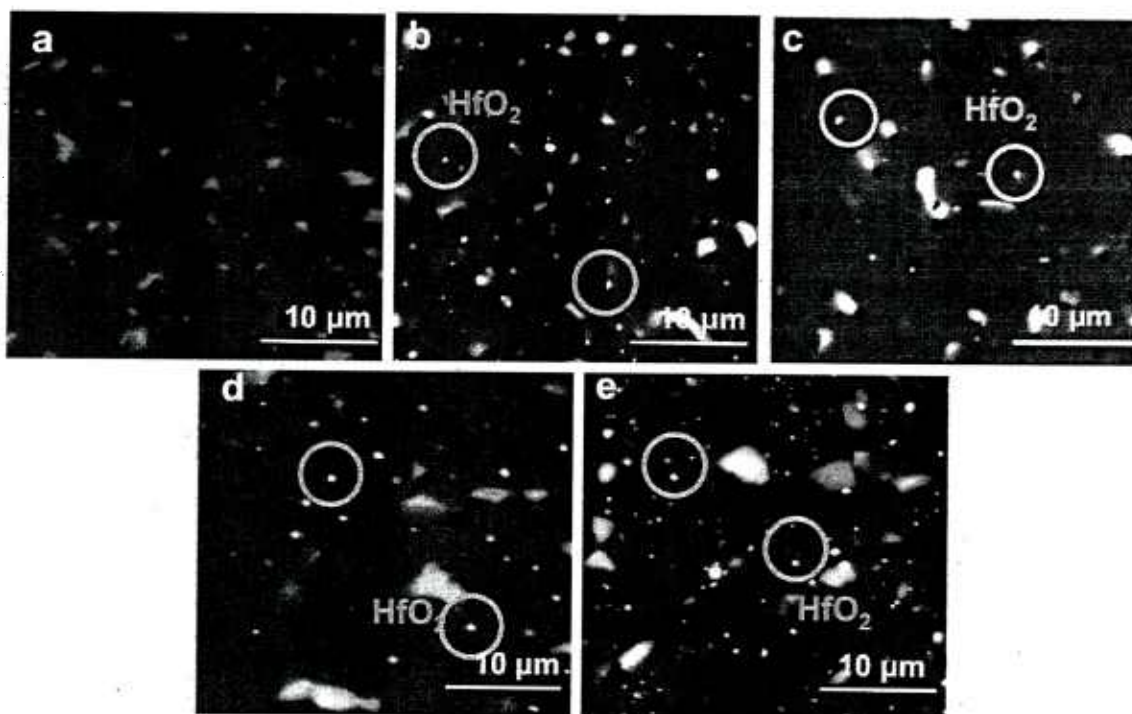


Figure 5.2: SEM micrographs showing representative features of the oxidized region of  $\text{HfO}_2$ -doped Ni/ Alumina oxidized at  $1400^\circ\text{C}$  for various times indicated in parentheses a) 100ppm (5h) b) 200ppm (20h) c) 300ppm (5h) d) 500ppm (5h) e) 2000ppm (20h)



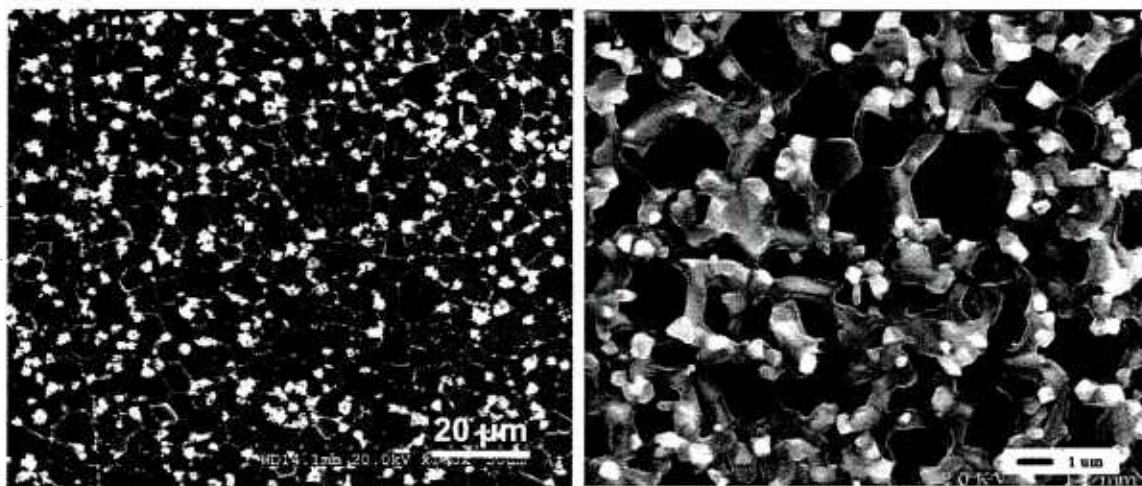


Figure 5.3: Free surface comparison between a) 500ppm Hf doped oxidized at 1300°C for 24h b) undoped alumina oxidized at 1300°C for 6h

Table 5.1: Summary of Grain Size for Samples with Different Hf<sup>4+</sup> Dopant Levels Oxidized at 1400°C

| Samples            | Undoped <sup>15</sup>   |           | 100ppm Hf <sup>4+</sup> |           | 200ppm Hf <sup>4+</sup>  |           |
|--------------------|-------------------------|-----------|-------------------------|-----------|--------------------------|-----------|
|                    | 1400°C                  | d (μm)    | 1400°C                  | d (μm)    | 1400°C                   | d (μm)    |
|                    | 5h                      | 2.05±0.31 | 5h                      | 3.03±0.64 | 20h                      | 9.07±1.36 |
|                    |                         |           | 35h                     | 3.65±0.41 | 50h                      | 9.88±1.85 |
| Average Grain Size |                         | 2.0±0.3   |                         | 3.3±0.5   |                          | 9.5±1.6   |
| Samples            | 300ppm Hf <sup>4+</sup> |           | 500ppm Hf <sup>4+</sup> |           | 2000ppm Hf <sup>4+</sup> |           |
|                    | 1400°C                  | d (μm)    | 1400°C                  | d (μm)    | 1400°C                   | d (μm)    |
|                    | 5h                      | 3.25±0.36 | 5h                      | 4.79±0.64 | 20h                      | 4.71±0.99 |
|                    | 30h                     | 3.09±0.36 | 20h                     | 5.36±0.75 | 50h                      | 5.03±1.05 |
|                    | 60h                     | 3.45±0.48 | 50h                     | 4.69±0.49 |                          |           |
| Average Grain Size |                         | 3.3±0.4   |                         | 4.9±0.6   |                          | 4.9±1.0   |

### 5.1.2 Oxidation Kinetics

From cross section images for each doping level, oxygen penetration depth  $x$  can be identified and measured precisely and reproducibly by following Cheng et al. [15]'s method. Figure 5.4 shows the square of the thickness of the oxidation zone ( $x$ ), as a function of oxidizing time ( $t$ ) for HfO<sub>2</sub> - doped Ni/Al<sub>2</sub>O<sub>3</sub> at 1400°C with different doping levels. Obviously, the growth of the oxidized zone follows a parabolic manner as described below:

$$x^2=kt$$

(1)

Where  $k$  is the parabolic rate constant. For each doping level,  $x$  has been measured from 10 different areas. The average value was taken as a measure of the thickness of the oxidized layer and hence the oxygen penetration depth. It is clear that adding HfO<sub>2</sub> to Ni/Al<sub>2</sub>O<sub>3</sub> results in a smaller parabolic rate constant compared with undoped samples as shown in the dashed line. It suggested that the presence of HfO<sub>2</sub> can slowdown the oxidation rate, but the degree of reduction depends on the doping levels.

As shown in Table 5.2 , an improvement ratio is obtained by dividing the rate constant for undoped samples by that of doped samples. The larger is the ratio, the slower is the oxidation, in other words, the better the oxidation resistance. The error

bar for the rate constant is calculated by obtaining the largest slope and smallest slope which might still reasonably fit the plot first and the uncertainty of the best fit is then taken as half the difference between these two fits. The larger the grain size, the lower the total grain boundary area per unit volume. Accordingly, assuming that oxygen grain boundary transport dominates, when comparing samples at different grain sizes it is necessary to scale the rate constant by multiplying by the inverse of the grain size.

By plotting the corrected  $k$  ratio as a function of doping levels in Figure 5.5, two regions can be defined as below. Region I that encompass doping levels below the solubility limit show a linear relationship between the doping levels and corrected ratio. For region II, however, which corresponds to doping levels exceeding the solubility limit, the corrected ratio is approximately constant.

To better understand the linear relationship in the region I to take into account the different sample grain sizes, we can plot the corrected ratio as a function of the grain boundary coverage ratio ( $f$ ). The coverage ratio was calculated with the following assumptions. The value of  $f$  was calculated from the dopant concentration and the grain size. For the purpose of this calculation, the grain shape was approximated as a tetrakaidecahedron [16], the grain boundary width was taken to be 0.5nm. The volume of a tetrakaidecahedron ( $V$ ) grain that would yield the corresponding measured 2-D grain intercept length ( $d$ ) is given by:

$$V = 0.499 \times d^3$$

The number of moles of Hf per grain ( $n_{Hf}$ ) is then given by:

$$n_{Hf} = V \times C \times 2 \times \rho(\text{Al}_2\text{O}_3)/M(\text{Al}_2\text{O}_3)$$

Where  $C$  is the fractional cation dopant concentration.

The volume of the gb region ( $V_{gb}$ ) is given by:

the mole of Hf ions for a certain doping level  $C$  in the grain boundary if completely segregated can be described by:

$$V_{gb} = 3.344 \times d^2 \times \delta_{gb}$$

Where 3.344 is a numerical factor relating the surface area of the tetrakaidecahedron to the equivalent grain intercept length, and  $d_{gb}$  is the grain boundary width. Since each boundary is shared by 2 grains, the number of moles of Hf in the grain boundary region ( $n_{gbHf}$ ) is:

$$n_{gb}(\text{Hf}) = V_{gb} \times 0.5 \times \rho(\text{Al}_2\text{O}_3)/M(\text{Al}_2\text{O}_3)$$

Knowing the number of moles of  $\text{Al}^{3+}$  in the gb region, and assuming the Hf ions substitute for  $\text{Al}^{3+}$ , the fractional coverage can be calculated.

Therefore, a replot of the data in the region I is shown in Figure 5.6. The results suggested that with increasing grain boundary coverage ratio, the corrected ratio

increases linearly, which means better oxidation-reduction. It is noteworthy that for 200ppm and 300ppm calculations, the small amount of second phase  $\text{HfO}_2$  were subtracted and error bar has been calculated from 10 measurements in the oxidized region. Since both 200ppm and 300ppm doping levels are slightly above the solubility limit, after subtracting the second phase particles, the grain boundary coverage is similar. The reason that 200ppm has a higher density of  $\text{HfO}_2$  second phase particles than 300ppm is due to its relative large grain size.

In Figure 5.7, Arrhenius behavior has been shown by plotting logarithm of the corrected parabolic rate constant versus reciprocal of the absolute temperature from 1250°C to 1400°C., All the data were normalized to a grain size of 2  $\mu\text{m}$  for consistent comparison. Three doping levels have been selected for comparison, which data included in Table 5.3. One is undoped alumina, [15] the other two is 100ppm and 500ppm, which is below and above the solubility limit respectively. The current data can be fitted into expressions as shown below:

$$k_c = 213 \exp[(-463 \text{ kJ/mol/k}^{-1})/RT] \text{ [15] (undoped)} \quad (2)$$

$$k_c = 58 \exp[(-459 \pm 31) \text{ kJ/mol/k}^{-1})/RT] \text{ (100ppm Hf)} \quad (3)$$

$$k_c = 110 \exp[(-480 \pm 22) \text{ kJ/mol/ k}^{-1}/RT] \text{ (500ppm Hf)} \quad (4)$$

Where the gas constant  $R$  equals to  $8.31 \text{ J/mol/K}^{-1}$ . The activation energy for 100ppm (below the solubility limit) and 500ppm  $\text{HfO}_2$  (above the solubility limit) doped samples was  $459 \pm 31$  and  $480 \pm 22 \text{ KJ/mol}$  respectively, which was roughly the same as the undoped alumina. The difference in magnitude of the  $k_c$  values corresponded to differences in the value of the prefactor.

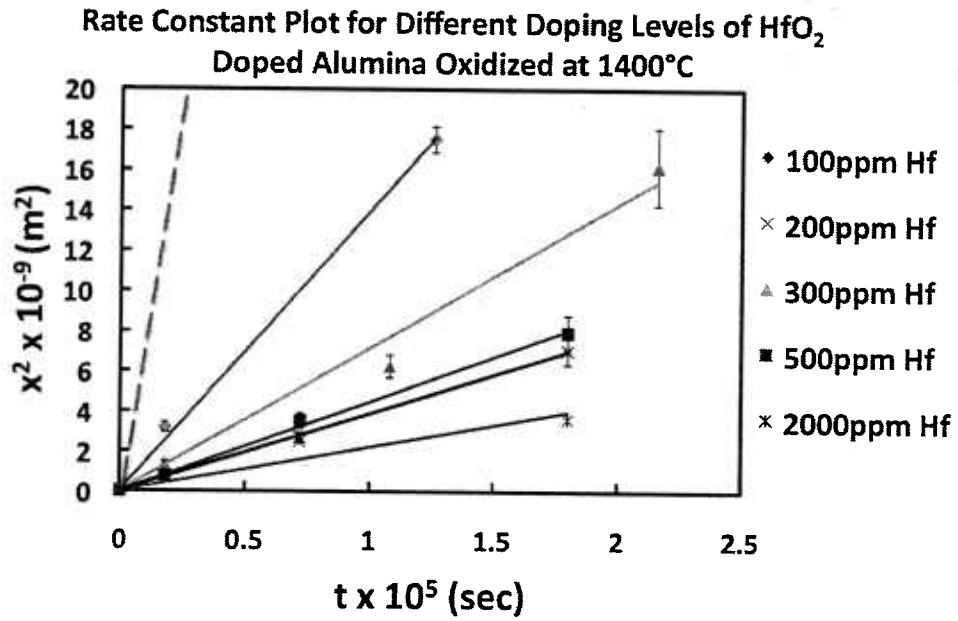


Figure 5.4: Graphs of the average of the square of the thickness of the oxidized layer,  $x^2$ , versus annealing time,  $t$ , for HfO<sub>2</sub> – doped Ni/Alumina oxidized at 1400°C with various doping levels. The results are averaged over 10 areas, with the error bars representing the standard deviation in  $x^2$ . The straight lines are least-square fits to the data for each doping content.



Table 5.2: Comparison between Values of the parabolic rate constants determined for all compositions of HfO<sub>2</sub> – doped alumina oxidized at 1400°C. Data adapted from Cheng et al. [15] for undoped Alumina/Ni also included.

| Composition              | $k(\text{m}^2/\text{s})$          | $k_{undoped}/k_{doped}$<br>(No.g.s.correction) | $k^c_{undoped}/k^c_{doped}$<br>(g.s.corrected) |
|--------------------------|-----------------------------------|--|--|
| Undoped <sup>15</sup>    | $7.77 \times 10^{-13}$            | 1  | 1  |
| 100ppm HfO <sub>2</sub>  | $(1.40 \pm 0.23) \times 10^{-13}$ | $5.5 \pm 0.9$                                  | $3.3 \pm 0.6$                                  |
| 200ppm HfO <sub>2</sub>  | $(2.21 \pm 0.24) \times 10^{-14}$ | $35.1 \pm 1.9$                                 | $7.4 \pm 0.4$                                  |
| 300ppm HfO <sub>2</sub>  | $(7.15 \pm 0.83) \times 10^{-14}$ | $10.9 \pm 1.3$                                 | $6.6 \pm 0.9$                                  |
| 500ppm HfO <sub>2</sub>  | $(4.48 \pm 0.44) \times 10^{-14}$ | $17.3 \pm 1.7$                                 | $7.1 \pm 0.8$                                  |
| 2000ppm HfO <sub>2</sub> | $(3.88 \pm 0.37) \times 10^{-14}$ | $20.0 \pm 1.9$                                 | $8.2 \pm 0.9$                                  |

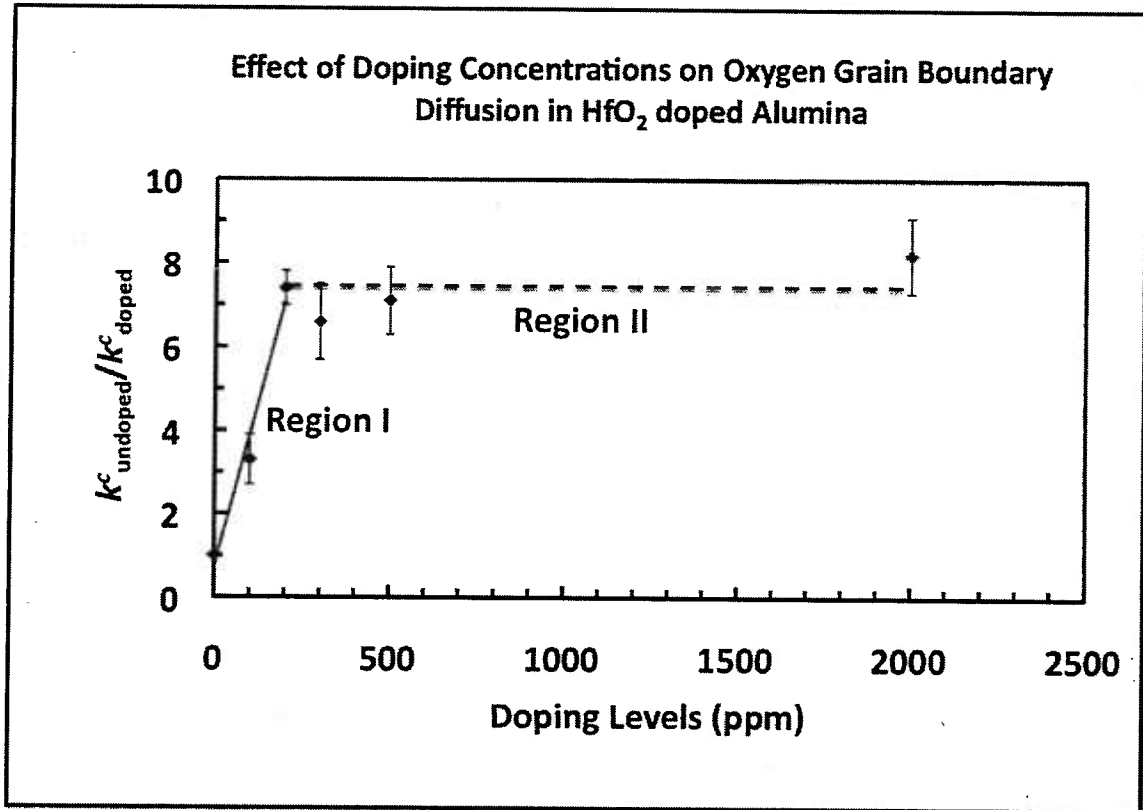


Figure 5.5: Graphs of the ratio after grain size correction ( $k^c_{\text{undoped}}/k^c_{\text{doped}}$ ) as a function of doping levels. Two regions can be identified clearly. The solid straight line is least-square fit to the doping levels including undoped, 100ppm, 200ppm. (Region I) The dashed straight line is an average of the value for doping levels higher than 200ppm. (Region II)

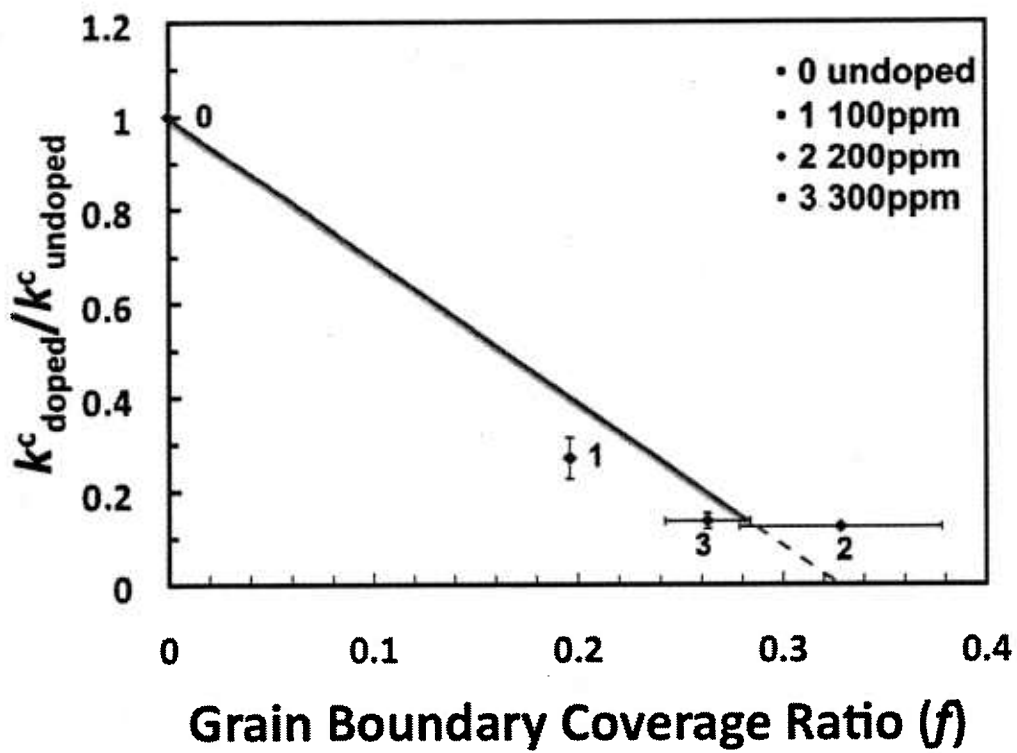


Figure 5.6: Plot of the corrected ratio ( $k^c_{\text{doped}}/k^c_{\text{undoped}}$ ) as a function of grain boundary coverage ratio. The solid straight line is least-square fit to the doping levels including undoped, 100ppm, 200ppm, and 300ppm.

Table 5.3: Comparison between values of the parabolic rate constants determined for 100ppm and 500ppm HfO<sub>2</sub> – doped alumina oxidized at three different temperatures. Average grain size *d* for each sample is also included.

| Composition             | $k(\text{m}^2/\text{s})$ (1400° C) | $k(\text{m}^2/\text{s})$ (1320° C) | $k(\text{m}^2/\text{s})$ (1250° C) |
|-------------------------|------------------------------------|------------------------------------|------------------------------------|
| 100ppm HfO <sub>2</sub> | $(1.40 \pm 0.23) \times 10^{-13}$  | $(8.68 \pm 0.33) \times 10^{-14}$  | $(4.24 \pm 0.22) \times 10^{-15}$  |
| 500ppm HfO <sub>2</sub> | $(4.48 \pm 0.44) \times 10^{-14}$  | $(2.39 \pm 0.27) \times 10^{-14}$  | $(1.69 \pm 0.10) \times 10^{-15}$  |
| Composition             | $d(\mu\text{m})$ (1400° C)         | $d(\mu\text{m})$ (1320° C)         | $d(\mu\text{m})$ (1250° C)         |
| 100ppm HfO <sub>2</sub> | 3.3                                | 1.9                                | 3.8                                |
| 500ppm HfO <sub>2</sub> | 4.9                                | 1.8                                | 4.4                                |

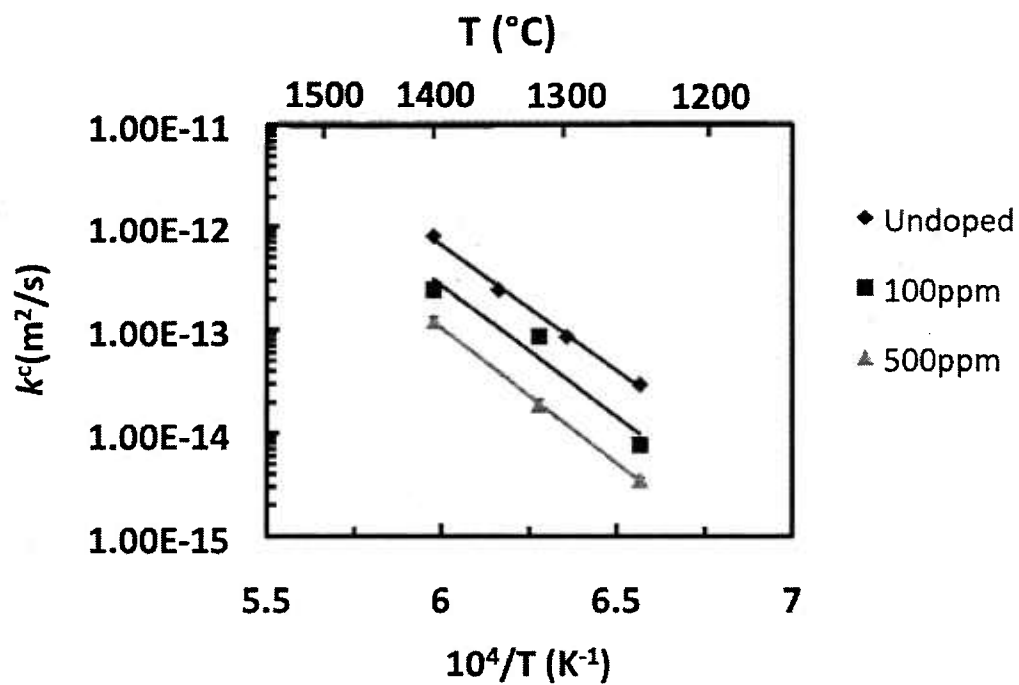


Figure 5.7: The corrected rate constant,  $k_c$ , plotted in logarithm scale versus reciprocal temperature for undoped [15], 100ppm and 500ppm HfO<sub>2</sub> - doped alumina oxidized from 1250°C to 1400°C

## ***5.2 The Effect of Oxidation Temperature***

### ***5.2.1 Microstructure***

In order to study the effect of oxidation temperature on the oxygen grain boundary diffusion in alumina, four oxidation temperatures (1400°C, 1320°C, 1250°C, 1150°C) were studied with doping level fixed at 500ppm. The cross section BSE images of 500ppm samples oxidized at different temperature have the same features that are shown in Figure.5.1 and Figure 5.2d. The oxidized region is mainly consisted of spinel phase, voids and HfO<sub>2</sub> second phase particles, while non-oxidized region is made of metallic nickel.

As described before, from the free surface image, grain sizes information can be obtained by using the linear intercept method, as shown in Table 5.4. No obvious grain growth and/or abnormal grain growth have been observed in each temperature.

### 5.2.2 Oxidation Kinetics

From cross section images for each oxidizing temperature, the oxygen penetration depth  $x$  can be identified as described earlier. Figure 5.8 shows the square of the thickness of the oxidation zone ( $x$ ), as a function of oxidizing time ( $t$ ) for 500ppm HfO<sub>2</sub> - doped Ni/Al<sub>2</sub>O<sub>3</sub> at different temperatures. The growth of the oxidized region follows a parabolic manner. For better visualization and differentiation, temperatures have been divided into two groups, 1320°C-1400°C and 1150°C-1250°C. Remembering the slope of each line is rate constant, therefore, it is clear that the lower oxidation temperature results in a smaller parabolic rate constant.

To obtain the magnitude of improvement (better oxidation resistance), rate constant ratio with grain size correction can be calculated for each temperature by using the method described in section 5.1.2, the results are listed in Table 5.5. For oxidation performed at 1400°C, the rate constant was found 7 times smaller than that of undoped sample. It is interesting that decreasing oxidation temperature from 1400°C to 1250°C only results in a slightly larger rate constant ratio, but at the lowest temperature 1150°C studied, a much larger ratio has been observed. At 1150°C the rate constant is about 40 times smaller than that of undoped sample. This transition like behavior is the main motivation for the following study on characterizing the grain boundary structure.

In Figure 5.7, it is already shown that Arrhenius behavior by plotting logarithm of the corrected parabolic rate constant versus reciprocal of the absolute temperature from 1250°C to 1400°C. It is noteworthy that the Inclusion of the 1150°C result in the Arrhenius plot of Figure 5.7 suggests that this data point is deviated from the othersFigure 5.9. As described earlier, the activation energy for 500ppm Hf doped sample oxidized from 1250°C to 1400°C is  $480 \pm 22$  kJ/mol. When including the 1150°C data, the activation energy increases to  $564 \pm 57$  kJ/mol. Due to only one data point at this lower temperature, by using statistical hypothesis testing, there is no firm conclusion that the difference between these two activation energy is significant. However, evidence from other studies, which will be addressed in the discussion, strongly indicate that the deviation of the 1150°C data is significant and probably due to a grain boundary complexion transition induced by oxidizing temperature.



Table 5.4. Summary of Average Grain Size for 500ppm HfO<sub>2</sub>-doped Alumina/Ni Oxidized at Different Temperatures

|                    | 1400°C | d (μm)    | 1320°C | d (μm)    | 1250°C | d (μm)    |
|--------------------|--------|-----------|--------|-----------|--------|-----------|
|                    | 5h     | 4.79±0.64 | 20h    | 1.77±0.32 | 48h    | 4.38±0.81 |
|                    | 30h    | 5.36±0.75 | 50h    | 1.87±0.40 | 84h    | 4.39±0.75 |
|                    | 60h    | 4.69±0.49 |        |           | 156h   | 4.35±1.06 |
| Average Grain Size |        | 4.9±0.6   |        | 1.8±0.4   |        | 4.3±0.9   |
|                    | 1150°C | d (μm)    |        |           |        |           |
|                    | 600h   | 1.10±0.24 |        |           |        |           |
|                    | 744h   | 1.31±0.12 |        |           |        |           |
| Average Grain Size |        | 1.2±0.2   |        |           |        |           |

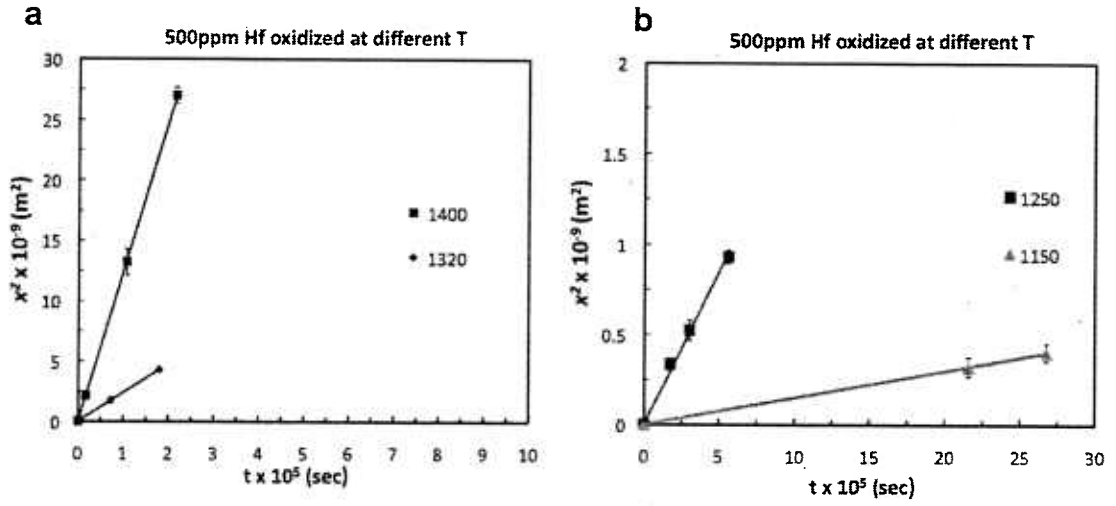


Figure 5.8: Graphs of the average of the square of the thickness of the oxidized layer,  $x^2$ , versus annealing time,  $t$ , for 500ppm HfO<sub>2</sub> – doped Ni/Alumina oxidized at a) 1320 ~1400°C b) 1150 ~1250°C. The results are averaged over 10 areas, with the error bars representing the standard deviation in  $x^2$ . The straight lines are least-square fits to the data at each temperature.

Table 5.5. Comparison between values of the parabolic rate constants determined for 500ppm HfO<sub>2</sub> – doped Alumina/Ni oxidized at different temperature. Rate constant and grain size data for undoped Alumina/Ni can be adapted from Cheng et al. [15]

| Temperature (°C) | $k(\text{m}^2/\text{s})$          | $k_{undoped}/k_{doped}$<br>(No.g.s.correction) | $k^c_{undoped}/k^c_{doped}$<br>(g.s.corrected) |
|------------------|-----------------------------------|--|--|
| 1400             | $(4.48 \pm 0.44) \times 10^{-14}$ | $17.3 \pm 1.7$                                 | $7.1 \pm 0.8$                                  |
| 1320             | $(2.39 \pm 0.27) \times 10^{-14}$ | $5.9 \pm 0.7$                                  | $6.5 \pm 0.8$                                  |
| 1250             | $(1.69 \pm 0.10) \times 10^{-15}$ | $18.3 \pm 1.1$                                 | $8.3 \pm 0.5$                                  |
| 1150             | $(1.50 \pm 0.21) \times 10^{-16}$ | $22.5 \pm 3.2$                                 | $38.4 \pm 5.5$                                 |

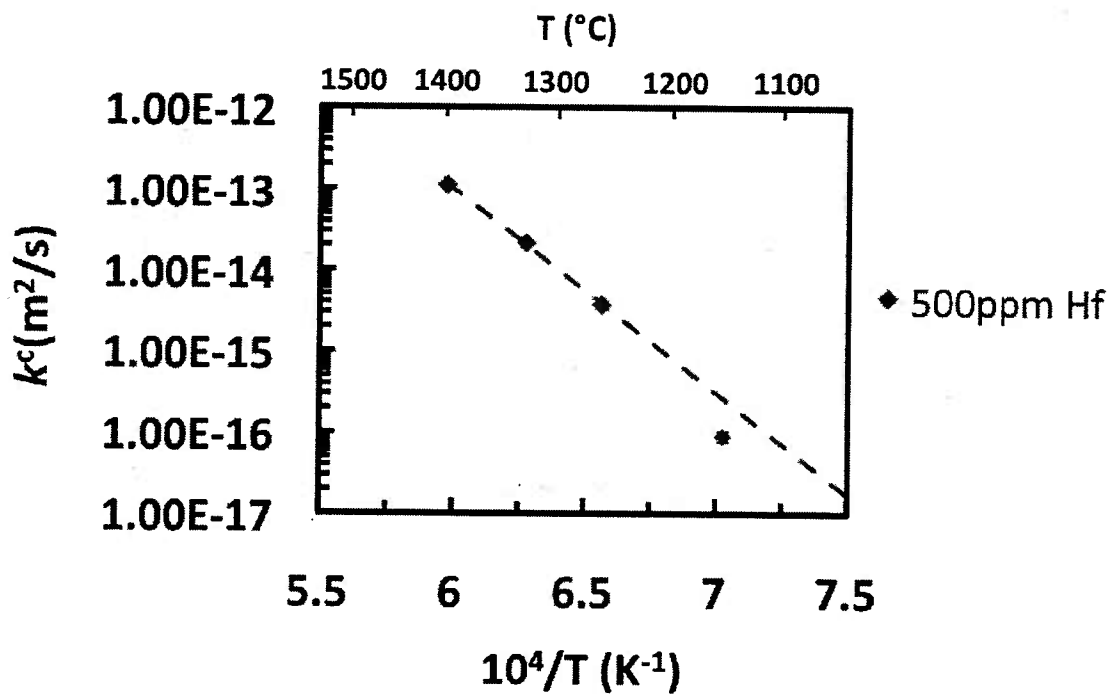


Figure 5.9: The corrected rate constant,  $k_c$ , plotted in logarithm versus reciprocal temperature for 500ppm  $\text{HfO}_2$  - doped alumina oxidized from 1150°C to 1400°C. The dashed line is least-square fit including three temperatures: 1250°C, 1320°C, and 1400°C. The dashed line was extended to show the deviation of the 1150°C data point.

### ***5.2.3 Grain Boundary Characterization by HAADF-STEM***

To investigate the grain boundary structure (complexions) in 500ppm HfO<sub>2</sub> doped alumina/Ni sample at various oxidizing temperature, thin TEM foil samples have been extracted from within the oxidized region or outside the oxidized region. The FIB samples were examined by using an aberration corrected high-angle angular dark field-scanning transmission electron microscopy (HAADF-STEM). The images were acquired at 200keV using a probe having a semi-angle of 20mrad. The relatively large collection angle (70-200mrad) of the HAADF-STEM detector enables the acquisition of atomic structure images with excellent atomic-number (Z) sensitivity, considering the difference between Hf (72), Al (13). Simulation of HAADF images was implemented by the fast Fourier transform multi-slice method, using the xHREM software suite.

#### ***5.2.3.1 Grain Boundaries Oxidized at 1400°C***

One of the FIB samples extracted from the oxidized region is shown in Figure 5.10. Multiple images are combined together to have a full view of the FIB sample. The discontinuity on the edge of the image is due to the artifact of grouping images, not the true grain boundaries. From the image, HfO<sub>2</sub> second phase particles and nickel aluminate spinel were readily identified using EDS. Moreover, brighter contrast existed in the grain boundary region and EDX analysis further confirm Hf segregating

in the alumina grain boundaries. It is noteworthy that the Ni peak was barely discernable above the EDX background, which indicated weak Ni segregating in the grain boundaries. A representative HAADF-STEM image of a general grain boundary is shown in the Figure 5.11. The left-hand side grain was tilted to the  $[0\ 0\ 0\ 1]$  zone axis; the adjacent grain is off-axis and hence exhibits low image contrast. It can be seen that direct imaging of the cation columns at the interface of the left grain has been achieved. For the  $[0\ 0\ 0\ 1]$  projected structure, it can be seen that the Hf ions substitute directly for the Al ions. Several Hf-rich cation layers are well resolved in Figure 5.11, together with lower contrast layer (see red arrow heads). Facet segments parallel to  $\{2\ -1\ -1\ 0\}$  are clearly apparent, as indicated by the dotted blue line. The facet steps correspond to a single cation layer, and appear to be periodic, with a spacing of  $\sim 1.6\text{nm}$ .

Figure 5.12 depicts a series of images for the same grain, taken at different values of defocus after drift correction; hence, successive layers of Hf ions located at different depths parallel to the beam direction are selectively imaged. Comparison between Figure 5.11 and Figure 5.12 reveals that the Hf-rich layers correspond to different depths in the beam direction. Thus, although Figure 5.11 suggests that there are multiple layers of Hf ions, the outer surface of the grain is actually composed of a series of steps, with the height of each step corresponding to a series of steps, with the height of each step corresponding to a single cation layer. For a probe semi-angle of  $20\text{mrad}$ , the depth of focus is  $\sim 10\text{nm}$ . Given that in Figure 5.11, approximately four layers of Hf ions are resolved, it seems reasonable that the depth separation of the

single-atom-width ledges is  $10/4=2.5\text{nm}$ , which is close to double the alumina unit cell dimension in the  $[0\ 0\ 0\ 1]$  direction.

A schematic atomic model illustrating the three-dimensional structure of the grain surface comprising one side of the grain boundary is shown in Figure 5.13. On the outermost cation layer, the segregated Hf ions (shown in blue) substitute directly for the Al ions (shown in pink). The surface exhibits faceting both parallel and perpendicular to the  $[0\ 0\ 0\ 1]$  direction. For clarity and ease of representation, the interval of faceting is contracted relative to the observed structure in both dimensions.

In order to test this model, multislice-based HAADF image simulation was performed. Figure 5.14(a) depicts a contracted atomic model of the proposed structure, with the projected structure along  $[0\ 0\ 0\ 1]$  shown in Figure 5.14(b). The actual step interval modeled was  $\sim 2.6\text{nm}$ . The simulation of the HAADF-STEM images is given in Figure 5.14(c). Note that, for the purposed of computational efficiency, only four steps were considered. It can be seen that the simulation reproduces the features of the experimentally observed images at the corresponding values of defocus. Note that, for step height set to either 1.3 or 5.2nm, the agreement between experimental and simulated images is poor. Interestingly, ongoing density functional theory (DFT) calculations have revealed that, for Hf atoms occupy the original atomic positions of the Al ions, with a minor displacement of  $0.2\text{\AA}$ , which is in good agreement with our experimental work and supports the model in Figure 5.14.

HAADF images have been obtained for at least 10 grain boundaries in both oxidized and non-oxidized region. It is generally agreed that segregation behavior of dopants could vary among grain boundaries depending on misorientation, grain boundary plane or dislocation. But In all cases, the general features with regard to the Hf segregation were similar, which suggest that for grain boundaries in 500ppm HfO<sub>2</sub>-doped samples oxidized at 1400°C, the extensive segregation of Hf ions to the outermost grain layer and the associated faceted structure of that layer maybe a general phenomenon. Moreover, it is noteworthy that the facets in the grain boundaries preferentially parallel to {2 -1 -1 0} and {1 0 -1 2}, which are “a” plane and “r” plane respectively. The HAADF images of other grain boundaries within the oxidized and non-oxidized region are listed in Figure 5.15 and 5.16.



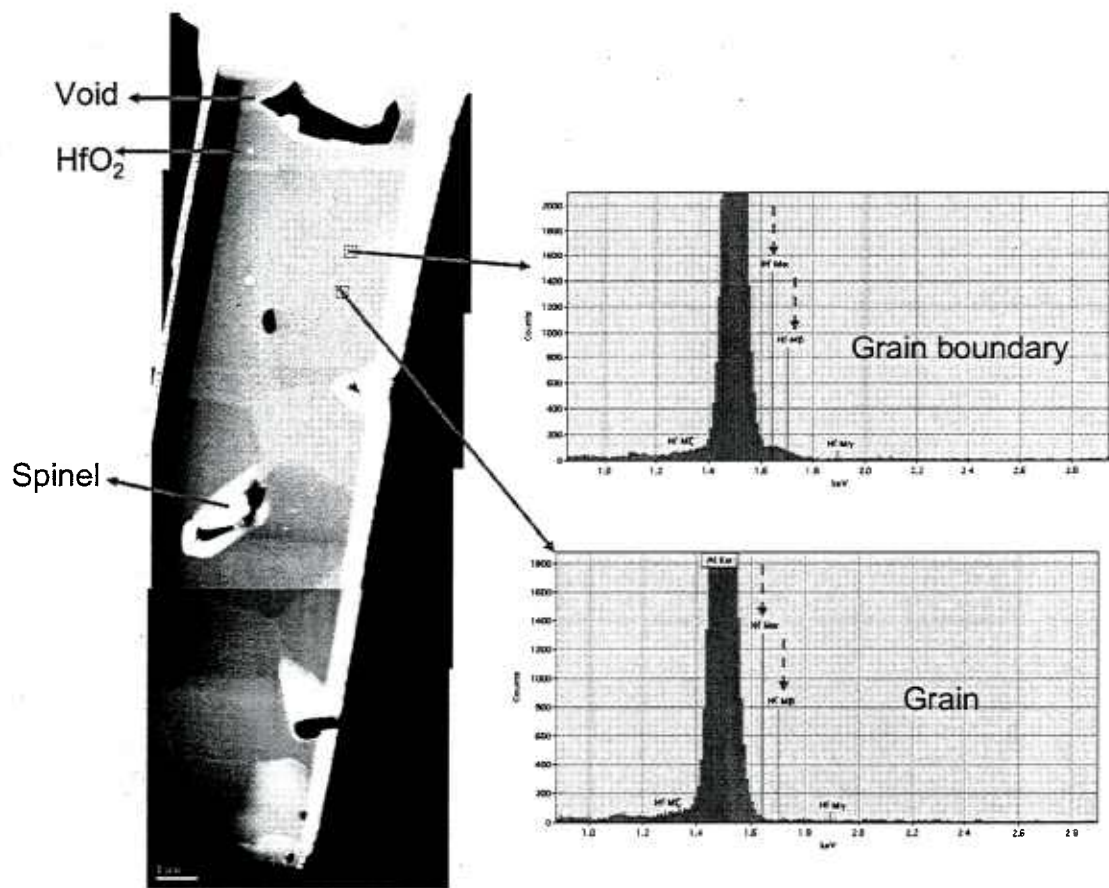


Figure 5.10: Low magnification HAADF image of 500ppm Hf-doped sample oxidized at 1400°C extracted from oxidized region is shown on the left. EDX analysis collected for grain boundary and grain respectively are shown on the right.

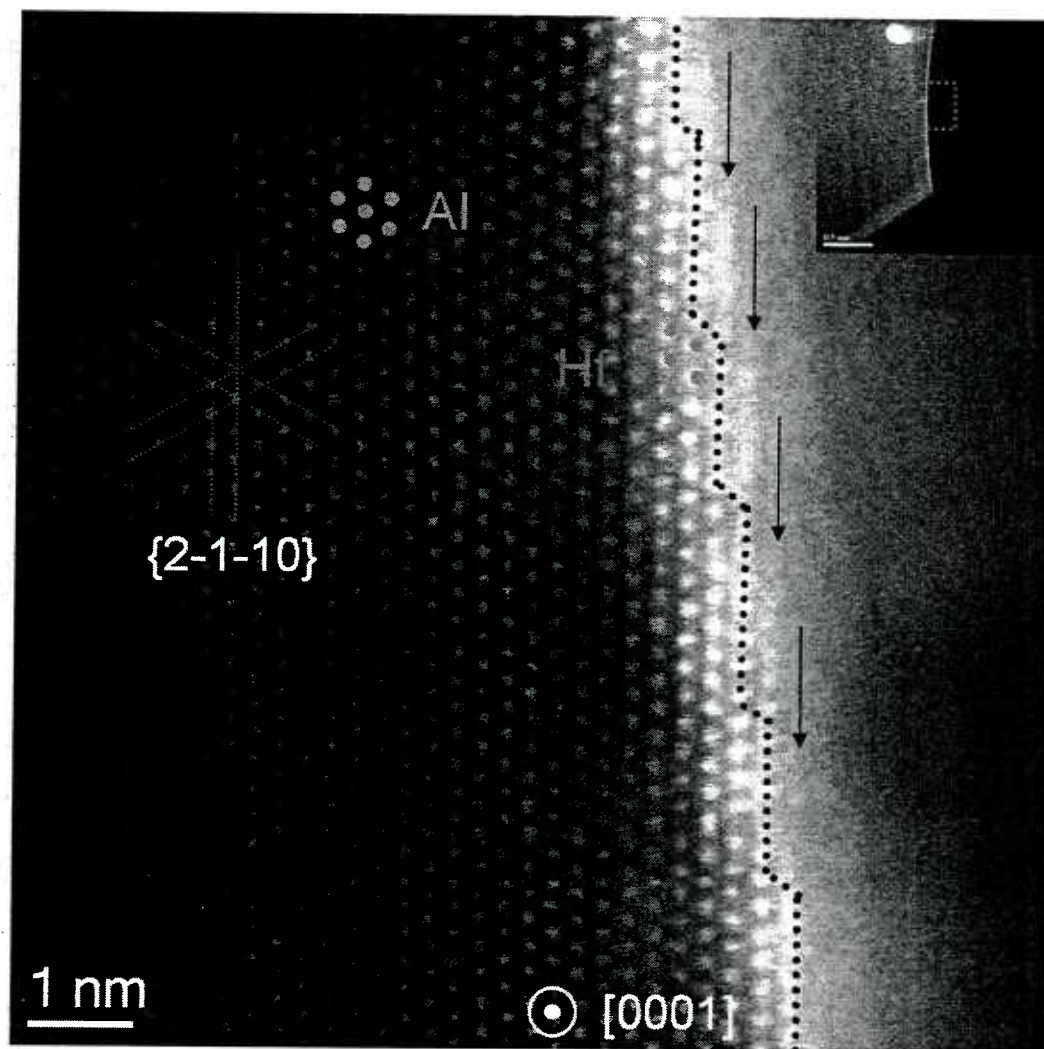


Figure 5.11: Cs-corrected HAADF-STEM image of 500ppm HfO<sub>2</sub>-doped GB oxidized at 1400°C with the left crystal orientated in the [0 0 0 1] direction.

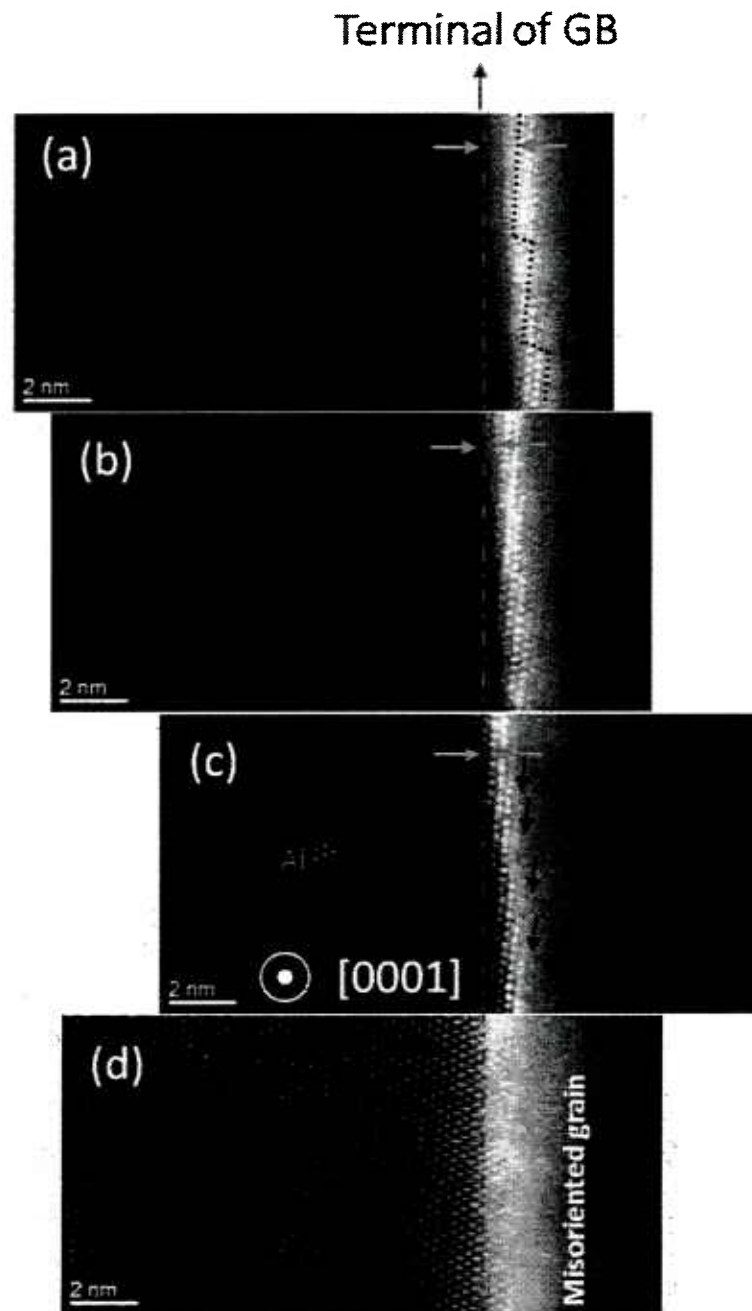


Figure 5.12: Focal series images of the grain boundary in Figure 5.11.

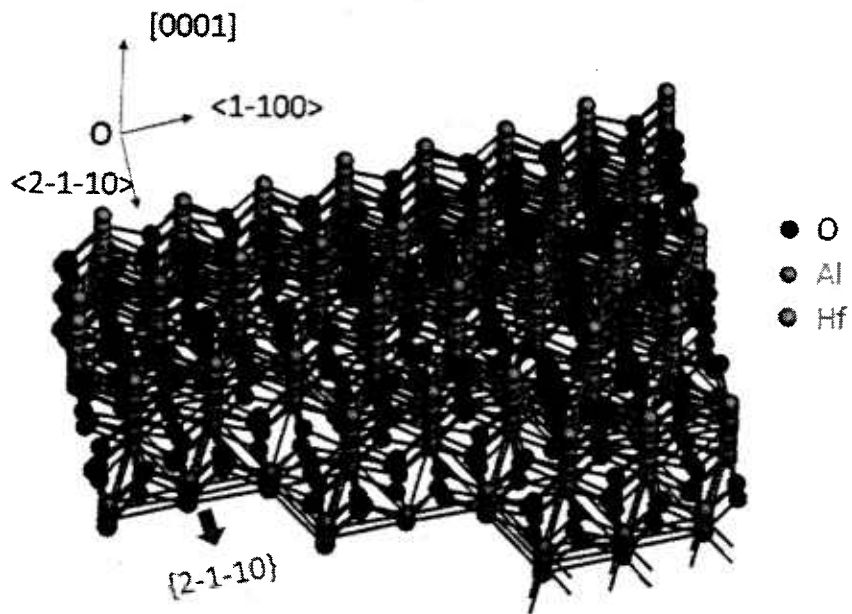


Figure 5.13 A schematic model shows the multi-dimensional steps of single-atom-height decorated with Hf. Note that the interval of faceting in both dimensions has been reduced for easier presentation.

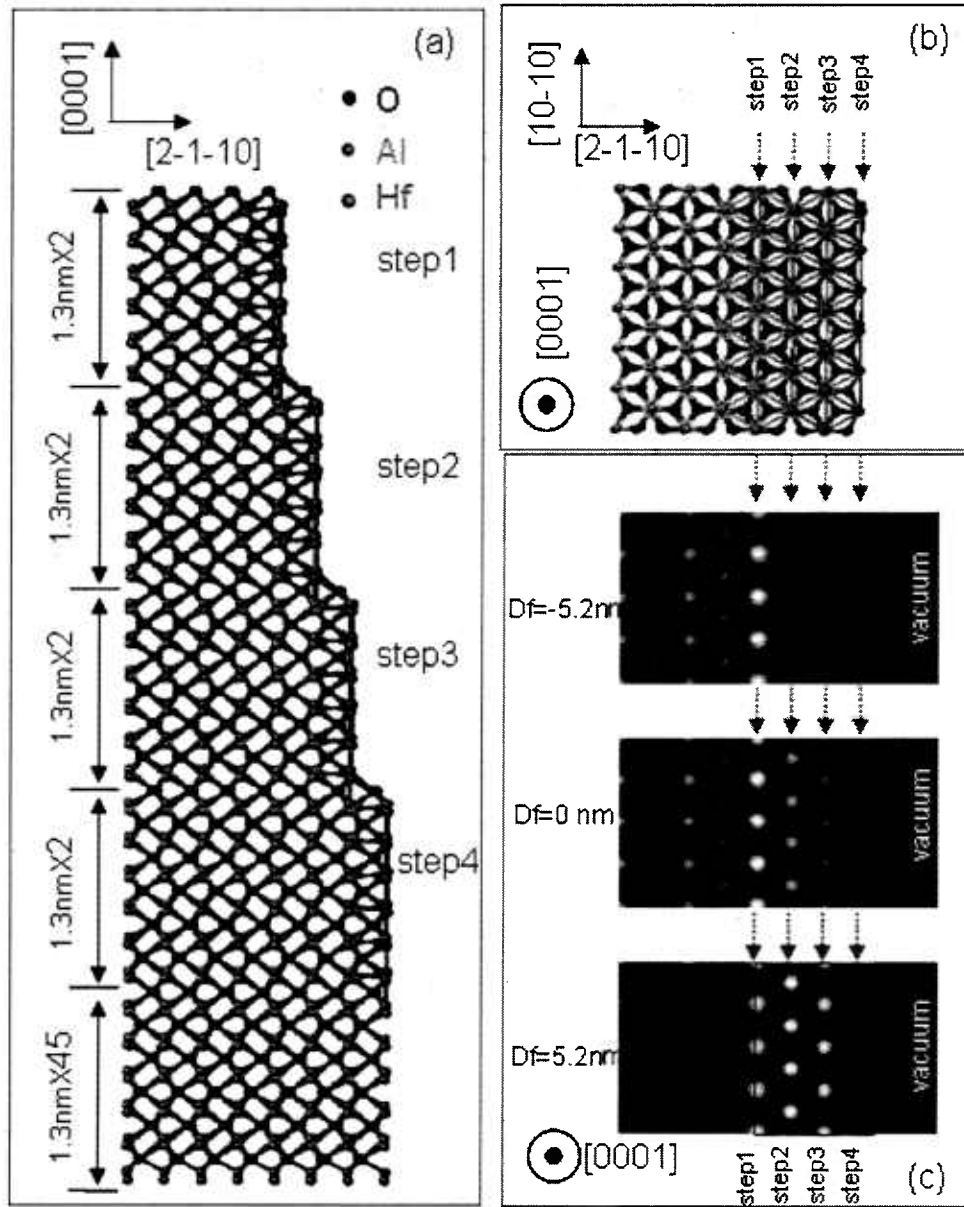


Figure 5.14 (a,b) Side view and plane view atomic model for HAADF simulation to interpret the contrast formation of lower contrast Hf layer. For each layer, the supercells are shown in one unit cell (1.3nm) and the symbol, 'X' denotes the supercells will be extended by the number after the symbol in the image calculation. (c) Simulated HAADF-STEM images reproduce the image contrast observed in the experiment.

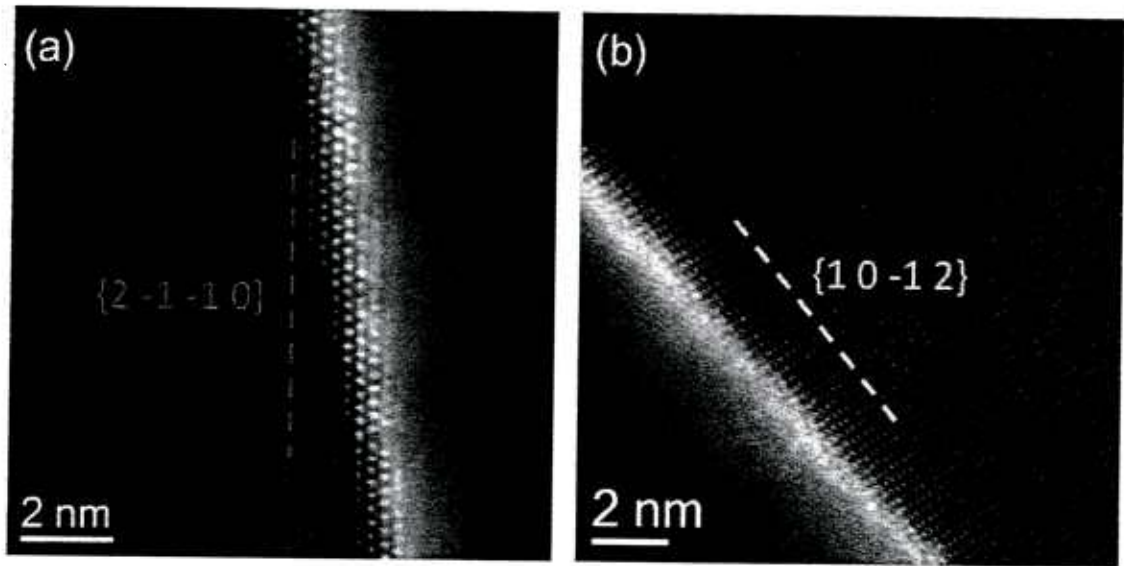


Figure 5.15 HAADF-STEM images of grain boundaries oxidized at 1400°C. Sample was taken from within the oxidized region. (a) blue dotted line shows facets parallel to  $\{2 -1 -1 0\}$  (b) zone axis and yellow dotted line shows facets parallel to  $\{1 0 -1 2\}$

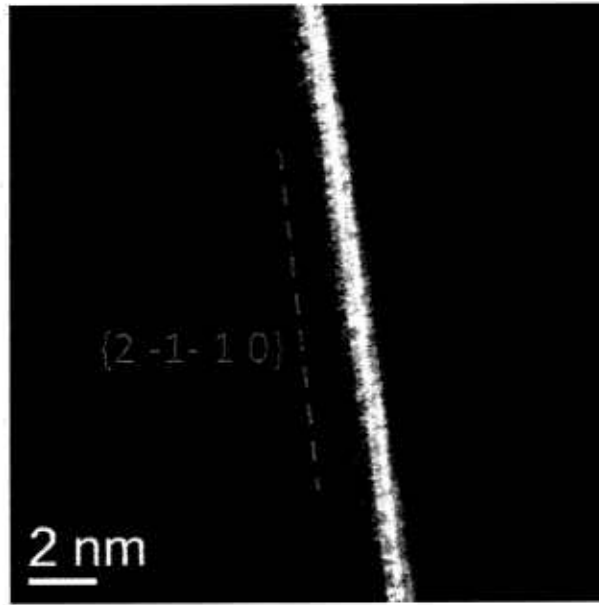


Figure 5.16 HAADF-STEM images of grain boundaries oxidized at 1400°C outside the oxidized region and blue dotted line shows facets parallel to  $\{2\ -1\ -1\ 0\}$

### ***5.2.3.2 Grain Boundaries Oxidized at 1250 °C***

Similar method can be used to study the grain boundary structure of 500ppm HfO<sub>2</sub>-doped samples oxidized at 1250°C. Representative images are shown in Figure 5.17 for grain boundaries within the oxidized region and Figure 5.18 outside the oxidized region respectively. Compared with the grain boundary structures for samples oxidized 1400°C, the 1250°C sample has very similar features. Extensive Hf ions segregation can be found in the alumina grain boundaries and grain boundaries are obviously faceted. More importantly, the facets are parallel to {2 -1 -1 0} and {1 0 -1 2}, which are the same as that of samples oxidized at 1400°C.



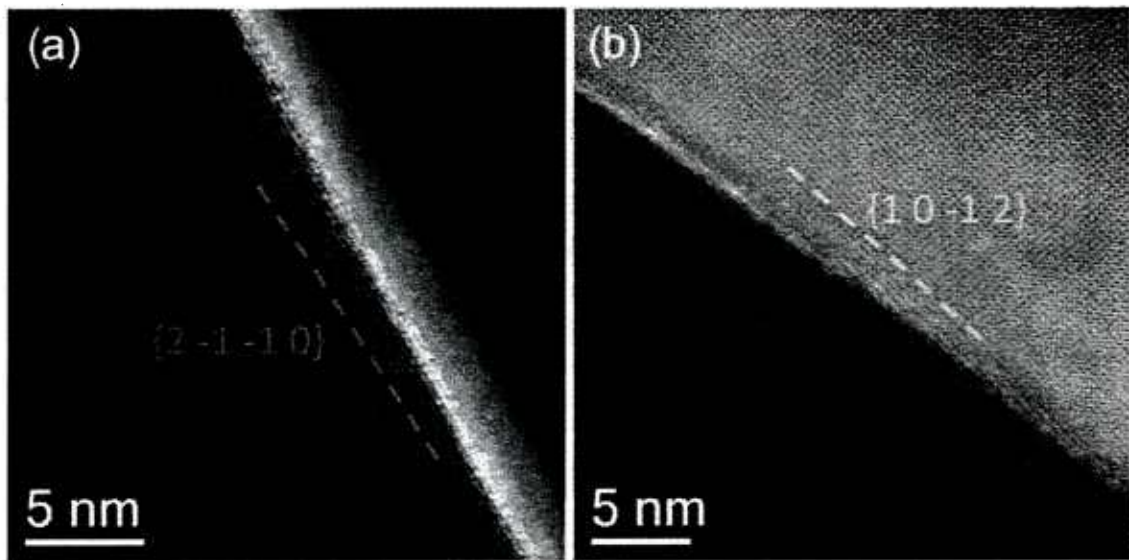


Figure 5.17 HAADF-STEM images of grain boundaries oxidized at 1250°C within the oxidized region. (a) Blue dotted line shows facets parallel to  $\{2 -1 -1 0\}$  (b) Yellow dotted line shows facets parallel to  $\{1 0 -1 2\}$

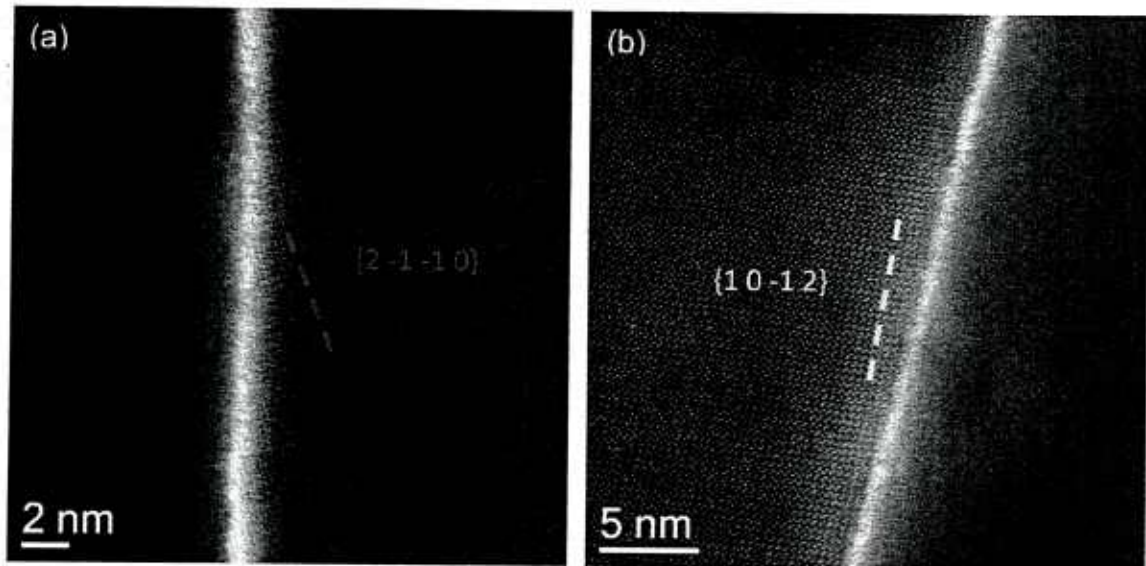


Figure 5.18: HAADF-STEM images of grain boundaries oxidized at 1250°C outside the oxidized region. (a) Blue dotted line shows facets parallel to  $\{2 -1 -1 0\}$  (b) Yellow dotted line shows facets parallel to  $\{1 0 -1 2\}$

### 5.2.3.3 Grain Boundaries Oxidized at 1150°C

Representative HAADF images of 500ppm HfO<sub>2</sub>-doped samples oxidized at 1150°C are shown in Figure 5.19 for grain boundaries within the oxidized region. Compared with samples oxidized at 1250°C and 1400°C, the obvious difference is that the facets tends to parallel to some new planes such as {0 0 0 6} and {2 -1 -1 3} besides the two original {2 -1 -1 0} and {1 0 -1 2} planes. Moreover, the grain boundaries are more atomic rough for samples oxidized at 1150°C while samples oxidized at 1250°C and 1400°C have obvious flat faceting structure. It is essential to know what percentage of the new planes (miscellaneous plane) presented within samples oxidized at 1150°C. Therefore, pie chart for percentage of three groups of planes that facets parallel to at each oxidation temperature is plotted in Figure 5.20. It is clearly shown that 20% facets in the grain boundaries were parallel to miscellaneous planes such as {0 0 0 6} and {2 -1 -1 3}, while at higher oxidation temperature with only {2 -1 -1 0} and {1 0 -1 2}. It should be pointed out that the percentage of each plane is calculated weighted on the facets length. In other words, longer facets mean higher percentage. Whether the additional 20 percent miscellaneous planes had a great effect on the oxidation rate will be discussed in the section 5.4.

#### ***5.2.3.4 Grain Boundaries for as hot-pressed***

As described earlier, the samples have been sintered at 1400°C. Hence, it is essential to reveal the grain boundary structure in order to compare before further oxidation experiments. The representative HAADF images of 500ppm HfO<sub>2</sub>-doped samples sintered at 1400°C are shown in Figure 5.21. It is clearly that the facets are parallel to  $\{2\ -1\ -1\ 0\}$  and  $\{1\ 0\ -1\ 2\}$ . The comparison with grain boundary structures after oxidation will be discussed later.

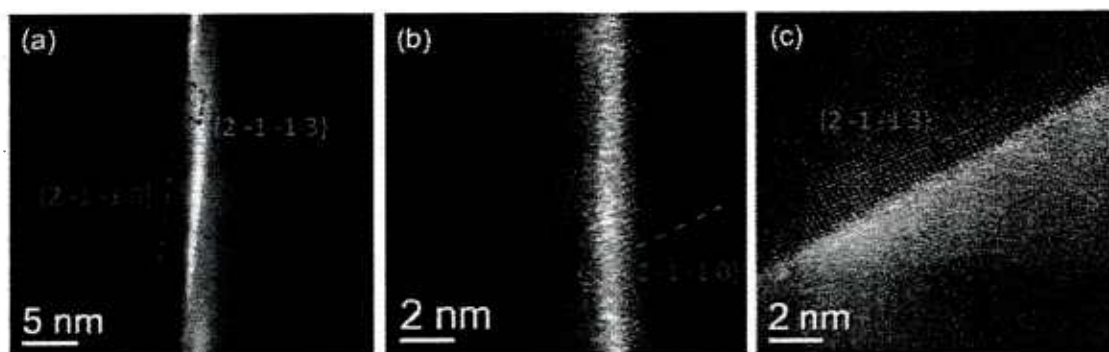


Figure 5.19: HAADF-STEM images of grain boundaries oxidized at 1150°C within the oxidized region. (a) Blue dotted line shows long facets parallel to  $\{2 -1 -1 0\}$  and green dotted line shows short facets parallel to  $\{2 -1 -1 3\}$  (b) Blue dotted line shows part of the facets parallel to  $\{2 -1 -1 0\}$  and red dotted line shows facets parallel to  $\{0 0 0 6\}$  (c) Green dotted line shows the facets parallel to  $\{2 -1 -1 3\}$

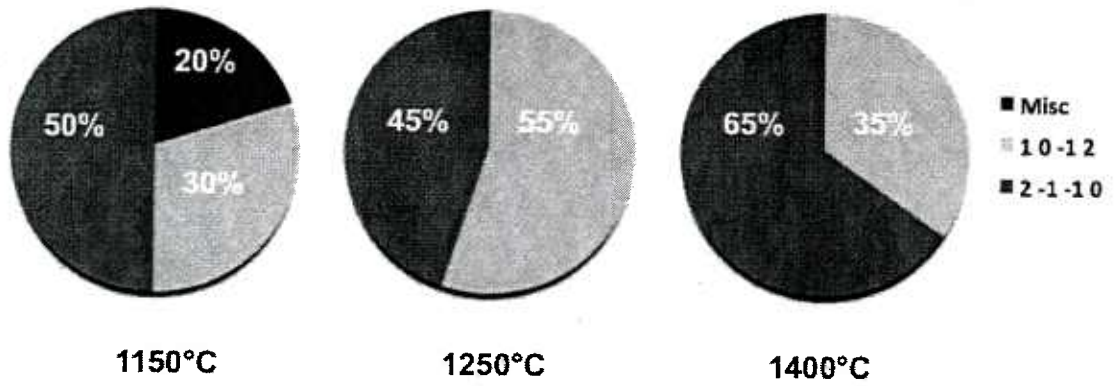


Figure 5.20: Pie chart showing percentage of plane occupied by a given facet for each oxidation temperature. From left to right, the samples are oxidized at 1150°C, 1250°C and 1400°C respectively. Blue portion represents miscellaneous planes including  $\{0\ 0\ 0\ 6\}$  and  $\{2\ -1\ -1\ 3\}$ . Yellow and green portion represents  $\{1\ 0\ -1\ 2\}$  and  $\{2\ -1\ -1\ 0\}$  respectively.

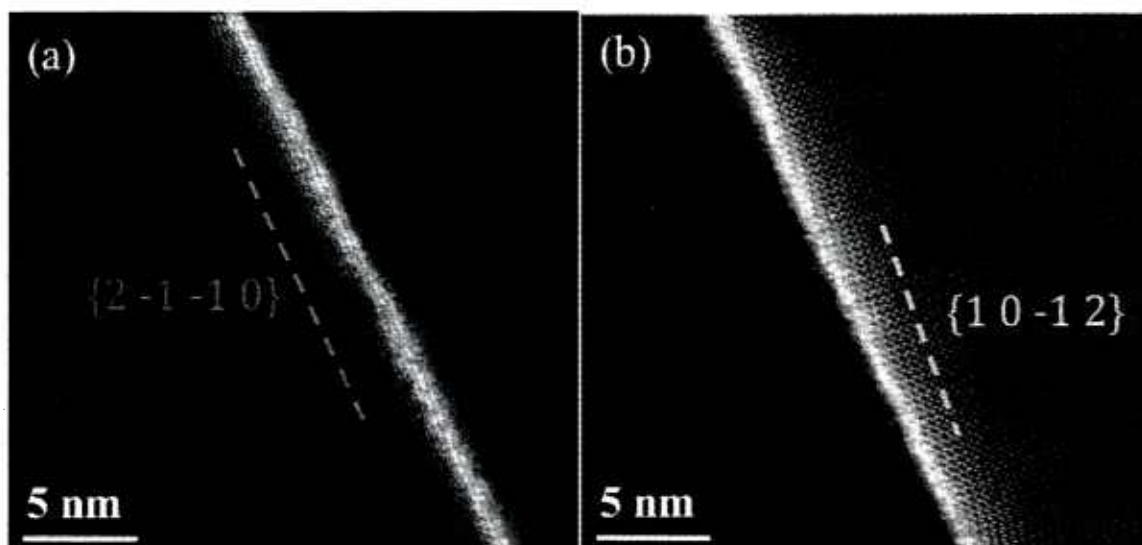


Figure 5.21: HAADF-STEM images of grain boundaries, 500ppmHf- $\text{Al}_2\text{O}_3$ -sintered at 1400°C. (a) Blue dotted line shows facets parallel to  $\{2 -1 -1 0\}$  (b) Yellow dotted line shows facets parallel to  $\{1 0 -1 2\}$

## 5.3 Discussion

### 5.3.1 The Effect of HfO<sub>2</sub> Doping Levels

The present work demonstrates that singly doping Al<sub>2</sub>O<sub>3</sub> with HfO<sub>2</sub> slows down the oxygen grain boundary diffusion. Thus, the benefit of HfO<sub>2</sub> doping is consistent with other REs such as Y<sub>2</sub>O<sub>3</sub> or La<sub>2</sub>O<sub>3</sub>, [1, 15] a result not altogether unexpected given that the ionic radius of Hf<sup>4+</sup> is 0.80Å smaller than Y<sup>3+</sup> (0.9Å) and La<sup>3+</sup> (1.06Å) but larger than Al<sup>3+</sup> (0.56Å). However, the present study was the first in which the HfO<sub>2</sub> dopant concentration was systematically studied.

The results show that the degree of reduction in the ratio of the relative oxidation rate constant  $k_{\text{undoped}}/k_{\text{doped}}$ , when normalized to account for grain size, depends on the HfO<sub>2</sub> content. Because the dopant levels studied spanned the solubility limit, this finding verifies that the effect of HfO<sub>2</sub> on oxygen grain boundary diffusion is primarily a solid-solution effect, which seems to be correlated with the concentration of Hf<sup>4+</sup> ions at the alumina grain boundaries. Various studies already verified that Hf<sup>4+</sup> preferentially segregates at alumina grain boundaries. [20, 21, 22] As shown in Figure 5.6, the rate constant ratio linearly increases with increasing Hf<sup>4+</sup> grain boundary coverage as a result of being more effective as obstacles to oxygen grain boundary diffusion. Once above the solubility limit, there is an upper limit to further



slowing down the oxygen grain boundary diffusion due to saturation of  $\text{Hf}^{4+}$  in the grain boundary.

Based on the experimental observations and calculations, it was determined that the maximum coverage of Hf is  $\sim 0.3$  monolayer. It is helpful to compare this value with the result of other studies, however, to the best of author's knowledge, there are very limited studies on the solubility limit of  $\text{HfO}_2$  in the alumina grain boundaries. Carter et al. [13] investigated the structure of  $\alpha$ -alumina  $\Sigma 11$  tilt grain boundary segregated with Hf by using periodic density-function theory calculations. They found that the saturation coverage of Hf is roughly 2 Hf atoms/unit cell (0.33 monolayer), which is consistent with the current study.

Previous works by Pint et al. [4, 5, 6] also showed that if the Hf content is too low (less than 100ppm), little or no benefit on the oxidation resistance was observed, whereas Hf levels such as 3000ppm higher than optimum will accelerate the alumina scale growth rate by oxidizing internally and forming  $\text{HfO}_2$  pegs, which can transport oxygen rapidly. Compared with our present results, the behavior of region I is consistent with that for dilute-doping levels where little effect has been observed on the reduction of oxidation rate. Once approaching and just above the solubility limit, the optimum effect has been achieved. However, with increasing  $\text{HfO}_2$  doping levels in Region II well above the solubility limit, it has no obvious effect, which indicates that the  $\text{HfO}_2$  second phase particles do not play an important role in reducing oxygen diffusion. The discrepancy between the current study and Pint's work is not well

understood. A possible explanation is that the 2000ppm doping level is not high enough to form continuous  $\text{HfO}_2$  particles network or pegs that can provide fast oxygen diffusion path. As seen in Fig 2,  $\text{HfO}_2$  particles with sub micron size are isolated and separated by microns' distance. Naumenko et al. [9] studied the effect of 300ppm Hf in FeCrAlY. The results showed that the alumina scale growth rate is not accelerated by the presence of Hf-containing phases due to the assumption that the Hf internal oxidation and incorporation into the scale occurred at a slower rate compared with Zr, which has an opposite effect. Further experiments on doping levels well above the solubility limit are needed to study the effect of  $\text{HfO}_2$  second phase particles.

The linear relationship in Figure 5.6 between grain boundary coverage and inverse rate constant ratio can be rationalized by previous work by Saxton [23], who did extensive studies on obstructed diffusion in biophysical systems. The results shown in Figure 5.22 indicated that the ratio between the value of the obstructed and unobstructed diffusion coefficient,  $D^*$  is linearly related to the obstacle concentration  $C$  under various lattice geometries described by  $D^*=1-C/C_p$ , where  $C_p$  is the percolation threshold. Note that this is the same functional relationship observed in the present study, since  $D^*$  scales with the inverse of rate constant. The consistence of this result with the simulation prediction suggests  $\text{HfO}_2$  act as an atomic scale obstacle for oxygen diffusion and with increasing obstacle concentration, the available site density for oxygen diffusion is decreased.

Evidence to support this general mechanism can be also found in the Arrhenius plot and other REs' studies. Cho et al [24] studied the effect of REs concentration on creep properties of  $\text{Y}_2\text{O}_3$  or  $\text{La}_2\text{O}_3$  doped alumina. They found that as the dopant content exceeded the solubility limit, there is no further improvement in the creep resistance. Moreover, the activation energy for dopant levels below and above the solubility limit was approximately the same, which indicates that the mechanism for reducing oxygen grain boundary diffusion at doping levels below and above the solubility limit is the same. Wang et al [25] studied the influence of dopant concentration on creep properties of  $\text{Nd}_2\text{O}_3$ -doped alumina. The major difference is that the apparent creep activation energy increased with increased dopant concentration and then saturated at dopant levels exceeding the solubility limit. Their work suggested that the initial increase of the activation energy was attributed to interaction between Nd-occupied sites. Compared with the current results from the Arrhenius plot based on the rate constant, the activation energies for 500ppm and 100ppm doped samples are  $459 \pm 31$  kJ/mol and  $480 \pm 22$  kJ/mol respectively, which are not significantly different to the value of 463 kJ/mol for undoped alumina. The similar activation energies suggest that the improved oxidation resistance at different doping levels is mainly due to the same mechanism. Moreover, it was qualitatively inferred that doping  $\text{HfO}_2$  in the alumina decreases the prefactor compared with that of undoped alumina. Since it is reasonable to correlated the rate constant with oxygen grain boundary diffusivity, the prefactor obtained in the current study cd be a proportion to the jump frequency of oxygen, in other words, the sites available for oxygen diffusion. Therefore, the larger the prefactor, the more available sites are for

oxygen diffusion, which means faster oxygen grain boundary diffusion. When doped with  $\text{HfO}_2$ , the reduced number of available sites for oxygen diffusion results in a better oxidation resistance. It may be argued about why the prefactor for 500ppm is larger than that for 100ppm. One possible explanation could be the interaction between Hf ions in the grain boundaries leading to a slightly larger activation energy, which weighted more than the prefactor. An alternate explanation is that the variance of the activation energy obscured the change of the prefactor, which suggested that more data points are needed in the current temperature range to obtain the activation energy with much smaller error.

In summary, the current results demonstrate clearly that the presence of  $\text{Hf}^{4+}$  slows down oxygen grain boundary transport in alumina by a factor of from 8 to 3 oxidized at  $1400^\circ\text{C}$  with various doping levels. It is useful to compare the results with alloy oxidation studies. As summarized by Hou [1] and Pint [6,7], for Ni- and Fe- based alloys oxidized at  $1200^\circ\text{C}$ , the addition of Hf could reduce the oxidation rate constant by a factor of 10. We may speculate that in the case of the alloy oxidation studies, the better oxidation resistance is due to  $\text{Hf}^{4+}$  not only slowing down the inward oxygen diffusion, but also the outward aluminum ion diffusion [18].

Last but not the least, it was inferred from the current study that reduced oxygen grain boundary diffusion is attributed mainly to a solid solution effect of  $\text{HfO}_2$  segregated at alumina grain boundaries acting as obstacles, which defines the optimum composition for maximizing its benefit on reducing oxygen grain boundary diffusion.

We recognize that other beneficial mechanisms may also participate in the oxidation behavior. As for the mechanism of grain boundary strengthening [12, 13], the local bonding environment has been predicted to change due to REs segregation. The stronger REs-O bonding compared to Al-O bonding could be another reason for reducing oxygen grain boundary diffusion. If this is true, it is reasonable to speculate that the activation energy may increase for  $\text{HfO}_2$ -doped compared with undoped alumina. From the Arrhenius plot, it seems that there is no significant increase for  $\text{HfO}_2$ -doped sample, from which infer that the improved oxidation resistance due to grain boundary strengthening might not be the dominant mechanism. Recently, a new mechanism has been proposed by Heuer[14, 31] in which the segregation of Y or Hf to the grain boundaries results in a modification of the near-band edge grain – boundary defect states for the improved oxidation resistance. It is also suggested that the transport is mediated by migration of grain boundary disconnections containing charged jogs other than point defects. However, the defect chemistry mechanism and whether the grain boundary disconnections affect the oxidation procedure are highly speculative and still under debate. In conclusion, the solid solution model fits better with the current physical-based mechanism that segregation of  $\text{HfO}_2$  in the grain boundary blocks oxygen fast diffusion path, which result in improved oxidation resistance.

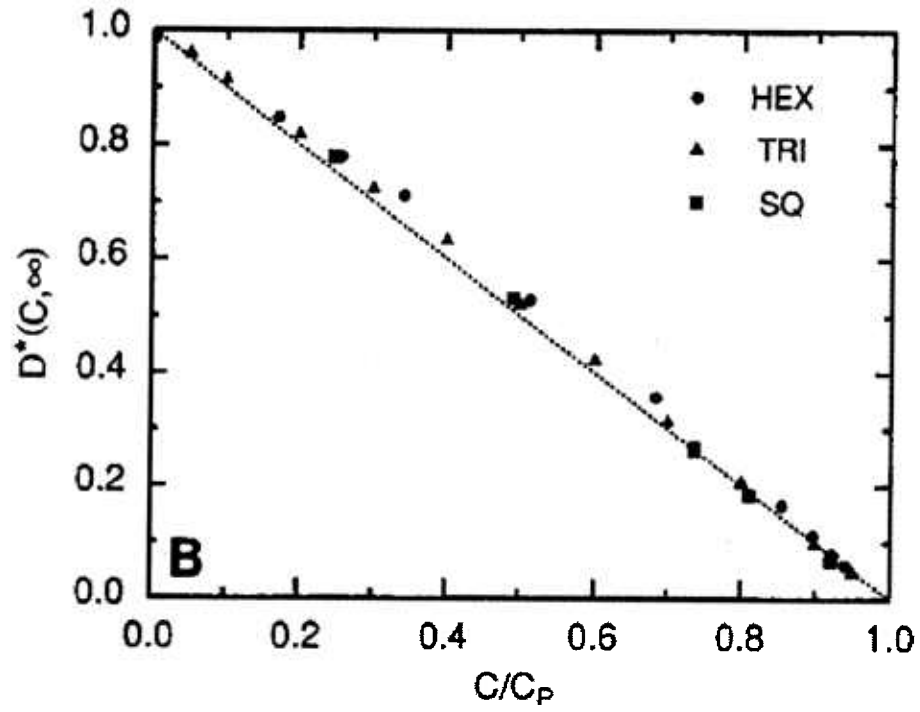


Figure 5.22: Diffusion coefficients  $D^*(C, \infty)$  as a function of  $C/C_p$  for three different geometries: hexagonal obstacles of unit radius on the triangular lattice (HEX), point obstacles on the triangular lattice (TRI), and point obstacles on the square lattice (SQ).

Table 5.6. Comparison of values of activation energy derived from different transport-related experiments in alumina.

| Author            | Type of Experiment  | Materials   | Temperature   | Q (kJ mol <sup>-1</sup> ) |
|-------------------|---|---|---------------|---------------------------|
| Hindam et al [29] | Oxidation   | Alumina forming alloys                                  | 1200°- 1300°C | 128                       |
| Wright et al [30] | Oxidation   | Alumina forming alloys                                  | 1000°- 1200°C | 274                       |
| Wada et al [28]   | Oxygen Permeation   | 0.2mol%HfO <sub>2</sub> +Al <sub>2</sub> O <sub>3</sub> | 1500°- 1700°C | 380                       |
|                   | PO <sub>2</sub> (II)/ PO <sub>2</sub> (I)=1Pa/10 <sup>-8</sup> Pa |   |               |                           |
|                   | Oxygen Permeation   | 0.2mol%HfO <sub>2</sub> +Al <sub>2</sub> O <sub>3</sub> | 1500°- 1700°C | 515                       |
|                   | PO <sub>2</sub> (II)/ PO <sub>2</sub> (I)=1Pa/10 <sup>-4</sup> Pa |   |               |                           |
| Cho et al [11]    | Creep   | Undoped Al <sub>2</sub> O <sub>3</sub>                  | 1200°- 1350°C | 483                       |
|                   |   | 1000ppmY+Al <sub>2</sub> O <sub>3</sub>                 |               | 685                       |
| Wakai et al [25]  | Creep   | 100ppm Zr+ Al <sub>2</sub> O <sub>3</sub>               | 1250°- 1400°C | 670                       |
|                   |   | 1000ppmZr+Al <sub>2</sub> O <sub>3</sub>                |               | 760                       |
| Cheng et al [15]  | Oxidation   | Undoped Al <sub>2</sub> O <sub>3</sub>                  | 1100°- 1500°C | 430                       |
|                   |   | 500ppmY+Al <sub>2</sub> O <sub>3</sub>                  |               | 497                       |
| Current Work      | Oxidation   | 100ppmHf +Al <sub>2</sub> O <sub>3</sub>                | 1250°- 1400°C | 459                       |
|                   |   | 500ppmHf +Al <sub>2</sub> O <sub>3</sub>                | 1250°- 1400°C | 480                       |
|                   |   | 500ppmHf +Al <sub>2</sub> O <sub>3</sub>                | 1150°- 1400°C | 564                       |

### 5.3.2 *The Effect of Nickel*

It is noteworthy to address the influence of nickel on oxygen transport. Previous work by Cheng et al. [26] showed that nickel doping increases the oxygen grain boundary transport in alumina by a factor of about 2 in the temperature range from 1250°C to 1400°C. From the point view of defect chemistry, the incorporation of divalent  $\text{Ni}^{2+}$  ions on  $\text{Al}^{3+}$  sites could result in the creation of oxygen vacancies, which would enhance oxygen grain boundary diffusion. However, with the presence of  $\text{Y}_2\text{O}_3$ , the effect of Ni on enhancing oxygen transport is negated, and the net result is that of  $\text{Y}_2\text{O}_3$  alone. Similar studies have also been found by Drahus et al, where co-doping with  $\text{Y}^{3+}$  and  $\text{Fe}^{3+}$  produced the same densification rate of alumina to that of  $\text{Y}_2\text{O}_3$ -doping alone. [27] It was speculated that the preferential segregation of the larger  $\text{Y}^{3+}$  ions to the alumina grain boundaries displaced the  $\text{Fe}^{3+}$  ions from the near boundary region; hence the influence of the  $\text{Y}_2\text{O}_3$ -doping predominated. A recent work by Yu et al [22] provided striking visual imaging of the  $\text{Hf}^{4+}$  distribution within the grain boundaries in the same alumina/Ni composites using aberration-corrected high-angle annular dark-field imaging. It was demonstrated that there was extensive substitution of the  $\text{Al}^{3+}$  ions by  $\text{Hf}^{4+}$  ions near the grain surface and the Hf-rich segregation layer contained multidirectional steps/facets. EDS analysis also indicated that the amount of Ni inside the alumina grain boundaries is below the detection limit. The strong preferential segregation of  $\text{Hf}^{4+}$  inside the alumina grain boundaries suggests a minor effect of Ni on the oxygen grain boundary diffusion.



Further evidence comes from examining the microstructure. As seen in Figure 1, there are voids inside the oxidized region, the formation of which has been suggested by various authors [16, 17] as being due to nickel outward diffusion. If nickel outward diffusion is much faster than oxidation, then a thin  $\text{NiAl}_2\text{O}_4$  layer will form on the free surface. Compared with undoped alumina/Ni, doping with  $\text{HfO}_2$  results in a much lower coverage of  $\text{NiAl}_2\text{O}_4$  on the free surface as shown in Figure 4.6. To answer the question that whether Ni outward diffusion influences the oxidation rate constant, a simplified calculation has been carried out. Details of the calculation method are given in Appendix A. The procedure starts with obtaining the amount of nickel that has been diffused out based on the area fraction of  $\text{NiAl}_2\text{O}_4$  on the free surface. Assuming that the total amount of nickel has been uniformly distributed in the matrix, the extra amount of Ni diffusing out can be converted to an equivalent oxidation penetration depth, which can be considered as an error on the oxidation depth measurement. The effect of equivalent length on the rate constant was found to be within 10 percent for  $\text{HfO}_2$  doped samples; the presence of  $\text{HfO}_2$  greatly suppresses the Ni outward diffusion. Moreover, the effect on the undoped sample was found to be even smaller than doped samples due to the larger penetration depth, although the surface area fraction is higher than doped samples. Therefore, it is suggested that nickel outward diffusion has a minor effect on the oxygen grain boundary diffusion in the current study, and therefore can be neglected.

### *5.3.3 The Effect of Oxidizing Temperature*

As described earlier, the 500ppm HfO<sub>2</sub> doped samples oxidized at 1150°C had about an order of magnitude higher corrected rate constant ratio compared with other three temperatures. This anomalously large improvement on the oxidation resistance motivated a detailed analysis on the effect of oxidation temperature.

From the Arrhenius plot in Figure 5.9, the 1150°C data point seems obviously deviated from the others. By conducting a statistical hypothesis testing, we found that the activation energy obtained from three data points and four data points was not significantly different. However, the activation energy obtained for four data points were found to be 560 kJ/Mol, which was significantly higher than that obtained in other oxidation studies as shown in Table 5.6. This much larger activation energy leads us to question on the method of direct fitting using all four data points.

The other explanation was motivated by Behera's work (34) on the kinetics of grain growth in 100ppm ZrO<sub>2</sub>-doped alumina, where a discontinuity in the grain boundary mobility was observed as shown in Figure 5.23. Two distinct regimes of grain growth were observed as described below: At temperatures <1550°C, the boundary mobility of 100ppm ZrO<sub>2</sub>-doped alumina is reduced as compared to undoped alumina, whereas it is higher than undoped alumina above 1600°C. The results suggested that the

100ppm  $\text{ZrO}_2$  induced a structural transition at the grain boundaries, although verification by direct grain boundary characterization was not conducted. By applying the same idea to the current study, it is suggested that the  $1150^\circ\text{C}$  data point lies in a complexion transition region, which plays the same role as the  $1600^\circ\text{C}$  data point for the 100ppm  $\text{ZrO}_2$  and other temperatures belonging to the same group. Moreover, from the 100ppm  $\text{ZrO}_2$  study, it is clear that obtaining activation energy values could be misleading depending on how many temperature points obtained. For example, the activation energy including data points higher than  $1550^\circ\text{C}$  was obviously higher than that of data points higher than  $1600^\circ\text{C}$ . Without the data points below  $1550^\circ\text{C}$ , the transition behavior would be missed. Due to the much lower temperature range studied in the current work, it is really not efficient to get measurable oxidation penetration depth at temperatures lower than  $1150^\circ\text{C}$ , which might take several months to obtain a single data point. Considering the statistical variation, other evidence is needed to verify the existence of a complexion transition induced by the oxidation temperature.

The large improvement of the rate constant ratio is also observed from other studies. In Figure 5.24, rate constant ratio's have been calculated and summarized from various studies for 500ppm  $\text{HfO}_2$  and 500ppm  $\text{Y}_2\text{O}_3$ . For consistent comparison, other doping levels are not considered. As a larger rate constant means better oxidation resistance, it is clear that at temperatures lower than  $1150^\circ\text{C}$ , 500ppm  $\text{HfO}_2$  has a much larger rate constant ratio than that for 500ppm  $\text{Y}_2\text{O}_3$ , while in the high temperature regime, the effect of  $\text{HfO}_2$  is similar to  $\text{Y}_2\text{O}_3$ .

Recent work by Wada et al. [28] conducted oxygen permeation experiments on Y- and Hf-doped alumina wafers under steep oxygen potential gradients at very high temperature above 1500°C. They found that Y-doping suppressed mainly the oxygen mobility and had no significant effect on aluminum mobility, while Hf-doping had the opposite effect. Based on the data, Y-doping reduced the oxygen permeation by a similar extent to that of Hf-doping for aluminum permeation, which seems to be consistent with current results that at higher temperature, the net effect of HfO<sub>2</sub> is no better than Y<sub>2</sub>O<sub>3</sub>-doping.

Grain boundary grooving experiments were conducted to compare the effect of Y and Hf on grain boundary energies in alumina. AFM was revealed to investigate the geometry of grooves where grain boundaries intersect a free surface, and then using an analysis due to Mullins [35] to infer the distribution of relative boundary energies in both undoped and doped samples (HfO<sub>2</sub> or Y<sub>2</sub>O<sub>3</sub>). Since these dopants are found to segregate preferentially to grain boundaries, it is clearly of interest to ascertain whether grain-boundary segregants alter boundary structure and energetics and, thereby, boundary transport. Figure 5.25 and Figure 5.26 show the cumulative distribution of boundary dihedral angles for undoped, 500ppm HfO<sub>2</sub> and 500ppm Y<sub>2</sub>O<sub>3</sub> doped alumina heat-treated at 1500°C based on grain populations of about 200 grains for each system. It can be seen that both HfO<sub>2</sub> and Y<sub>2</sub>O<sub>3</sub> lead to a similar qualitative shift in the distribution to smaller dihedral angles, which means larger relative boundary energy, compared with undoped alumina. The result is unexpected

since dopant segregation generally results in lower grain boundary energy. Moreover, the values of the means for the dihedral angle measurements were determined to be as follows: 500ppm Hf-doped alumina ( $138.1 \pm 6.3$  deg.), 500ppm Y-doped alumina ( $135.6 \pm 8.3$  deg.), undoped alumina ( $142.6 \pm 10.0$  deg.). The AFM measurements suggested that at 1500°C, 500ppm HfO<sub>2</sub> has a similar effect on the relative grain boundary energy as 500ppm Y<sub>2</sub>O<sub>3</sub>. Therefore, it is reasonable to speculate that at such high temperature, HfO<sub>2</sub> has a similar grain boundary structure (complexion) as 500ppm Y<sub>2</sub>O<sub>3</sub>, which resulted in a similar oxidation resistance. The slight difference in the rate constant ratio could be due to a difference in segregation amount or ionic size. Summarizing the above results, the similar effect of HfO<sub>2</sub> and Y<sub>2</sub>O<sub>3</sub> on the rate constant ratio at higher temperature is correlated with a similar effect on the grain boundary energy ratio, presumably due to a similar segregation behavior and grain boundary structure.

At temperatures lower than 1200°C, a great improvement in the rate constant ratio has been observed for HfO<sub>2</sub> doping, while only a slightly improvement was observed for Y<sub>2</sub>O<sub>3</sub> doping. This transition like behavior for HfO<sub>2</sub> doping suggested that the oxidation temperature induces a complexion transition, while not for Y<sub>2</sub>O<sub>3</sub> doping. In order to verify the existence of complexion transitions, comparison between grain boundary structures and chemistry for 500ppm HfO<sub>2</sub> doped samples oxidized at high and low temperature is essential. As shown in Section 5.2.3.1, by using Cs-corrected HAADF-STEM combined with through focal imaging technique, a detailed general grain boundary structure characterization is achievable. These results highlighted that

for grain boundaries in 500ppm HfO<sub>2</sub>-doped alumina oxidized at 1400°C or 1250°C, the extensive segregation of Hf ions to the outermost grain layer and the associated faceted structure of that layer is a general phenomenon, which indicates a significant modification in the alumina grain boundary structure that would be consistent with either the bonding or site-blocking models for rationalizing the slower oxygen grain boundary transport. More importantly, the grain boundary facets are preferentially parallel to  $\{2\ -1\ -1\ 0\}$  and  $\{1\ 0\ -1\ 2\}$ . The above findings differ from the results of Tatlock et al. [21], who reported a more diffuse segregation region for grain boundaries in Hf and Y codoped Fe-20Cr-5Al oxidized at 1250°C. It should be stated, however, that a direct comparison between the two studies is difficult because of the difference in imaging conditions, as well as discrepancies in the dopant concentration and processing history of the alumina samples.

For grain boundaries oxidized at 1150°C, the major differences can be described as follows: About 20% of the grain boundary facets, which are weighted by the facet length were parallel to some new planes such as  $\{0\ 0\ 0\ 6\}$  and  $\{2\ -1\ -1\ 3\}$ ; The grain boundaries also seem to be more atomically rough than those oxidized at higher temperature. Therefore, a non-congruent transition [46] or a defaceting transition was induced by lowering the oxidation temperature. The following discussion will be focused on whether the occurrence of the new planes and defaceting transition can greatly improve the oxidation resistance, as observed in the current study.

Extensive TEM/EDX studies have been performed by Swiatnicki[37] in Mg and Ti doped commercial grade alumina to study the relationship between intergranular segregation and grain boundary crystallography. The results suggested that Si segregates preferentially on boundary planes lying parallel to the basal plane  $\{0\ 0\ 0\ 1\}$  in one grain, while Ti segregates on the rhombohedral plane  $\{0\ 1\ -1\ 2\}$  and planes with a low atomic density. Therefore, it was concluded that the type of grain boundary plane determines the segregation level of a particular dopant, other than misorientation. Moreover, similar studies by Pang et al. [36] using Auger measurements to study grain boundary segregation of Nb-doped TiO showed a strong dependence of segregation level on grain boundary plane orientation, where high levels of segregation occurred along regions of grain boundary plane orientation space estimated to correspond to high grain boundary energy, while low levels of segregation occur along regions corresponding to low grain boundary energy. This trend appeared to be consistent with qualitative arguments that there is greater potential for reduction of the total interfacial energy of a polycrystal if segregation occurs most strongly on high-energy grain boundaries.

It should be pointed out that the planes the facets form parallel to in the current study is not exactly the same as the grain boundary planes described above. However, the micro facets observed in the current study, which are difficult to be revealed without using Cs-corrected HAADF-STEM, provides a more accurate description of the grain boundary plane. The relationship between the planes and the facets and grain boundary energies for different temperatures has been analyzed. For the case of

alumina, a rough estimation of grain boundary energy can be obtained based on surface energies of the grain planes of the adjoining crystals, which can be described as  $\gamma_{GB} = 2\gamma_s - E_B$ , (44) where  $\gamma_{GB}$  is the grain boundary energy,  $2\gamma_s$  is the energy to create two surfaces, and  $E_B$  is a binding energy. In the case of a high angle grain boundary, the binding energy can be approximately considered as a constant. Therefore, the surface energy of the grain boundary plane could be a good indication of the grain boundary energy. Earlier experimental work by Kitayama et al. [38] used a lithography-based method to generate planar arrays of intragranular cavities with controlled size, initial shape and spacing to determine the Wulff shape of the undoped alumina. The results suggested that  $\{2 -1 -1 0\}$  and  $\{1 0 -1 2\}$  have a lower surface energy compared with  $\{0 0 0 6\}$  and  $\{2 -1 -1 3\}$ . Similar results by simulation can be also found in [39]. Therefore, as suggested earlier that higher surface energy indicates a higher grain boundary energy, the segregation level of dopants in these high-energy planes may be higher due to a greater potential for energy reduction.

As for the grain boundaries oxidized at 1150°C, with portions of the facets parallel to these high-energy planes, the segregation level of Hf ions could be higher in those regions than the grain boundaries oxidized at higher temperature. As indicated by the HfO<sub>2</sub> doping levels study, we believe the reduced oxygen grain boundary diffusion is mainly due to segregation of Hf ions in the grain boundaries acting as obstacles to block fast diffusion path. Therefore, we can speculate that the great improvement on the rate constant ratio is due to the presence of these high-energy planes with higher Hf ions segregation, which results in a slower oxygen grain boundary diffusion.



Moreover, we believe that these high-energy planes are thermodynamically stable at 1150°C since the facets paralleling planes in the as-hot pressed samples are mainly low energy planes  $\{2\ -1\ -1\ 0\}$  and  $\{1\ 0\ -1\ 2\}$ , which indicated these planes are thermodynamically stable in the 1250°C and 1400°C as well.

However, quantitative analysis on the segregation level at atomic scale is extremely difficult. Conducting diffusion simulation studies as a function of grain boundary character will be useful for future work to verify the correlation between diffusivity, boundary structure, segregation level and effective diffusivity when 20% of the grain boundaries were transformed to lower diffusivity. Moreover, given that  $\text{Hf}^{4+}$  is a quadrivalent ion substituting for trivalent  $\text{Al}^{3+}$ , knowledge of the oxygen ion distribution in the boundary region would clearly be highly pertinent to further understanding the role of the dopant ions. Unfortunately, this information is difficult to access experimentally, and is hence the subject of ongoing investigation using ab initio modeling.

As described earlier, the 1150°C sample has a more atomically rough grain boundary structure than those oxidized at higher temperature. This roughening transition at lower oxidizing temperature is not expected since roughening transitions are traditionally considered to occur from low to high temperature. Yoon et al. [40] did extensive studies on roughening transition of grain boundaries in oxides. One of the results showed that the grain boundaries in high-purity alumina sintered at 1620°C were observed to be smoothly curved and hence rough. When this alumina was heat-

treated again at lower temperature such as 900, 1000, and 1100°C, some grain boundaries developed hill and valley shapes, hence faceted. It is possible that the other grain boundaries remained rough because their roughening temperature was lower than 900°C. One possible explanation for the roughening transition at lower temperature in the current study is a grain size effect. Since samples oxidized at 1150°C had a smaller grain size than those oxidized at higher temperature, the grain boundary tends to be more curved at lower temperature and therefore, atomically rough. The other possible explanation is due to the  $\text{Hf}^{4+}$  segregation, which reversed the roughening transition temperature. More experiments are needed to elucidate this phenomenon such as annealing the 1150°C sample in higher temperature 1400°C to check whether these miscellaneous planes will disappear and the boundary will become more faceted again.

In conclusion, by lowering the oxidation temperature to 1150°C, grain boundary faceting transitions (complexion transitions) were initiated, resulting in a more atomic rough structure containing more high-energy planes, which maybe occupied with a higher Hf segregation level and hence, a much better oxidation resistance. The current results highlight the significant role of complexion transition in the field of oxidation, which is traditionally not considered.

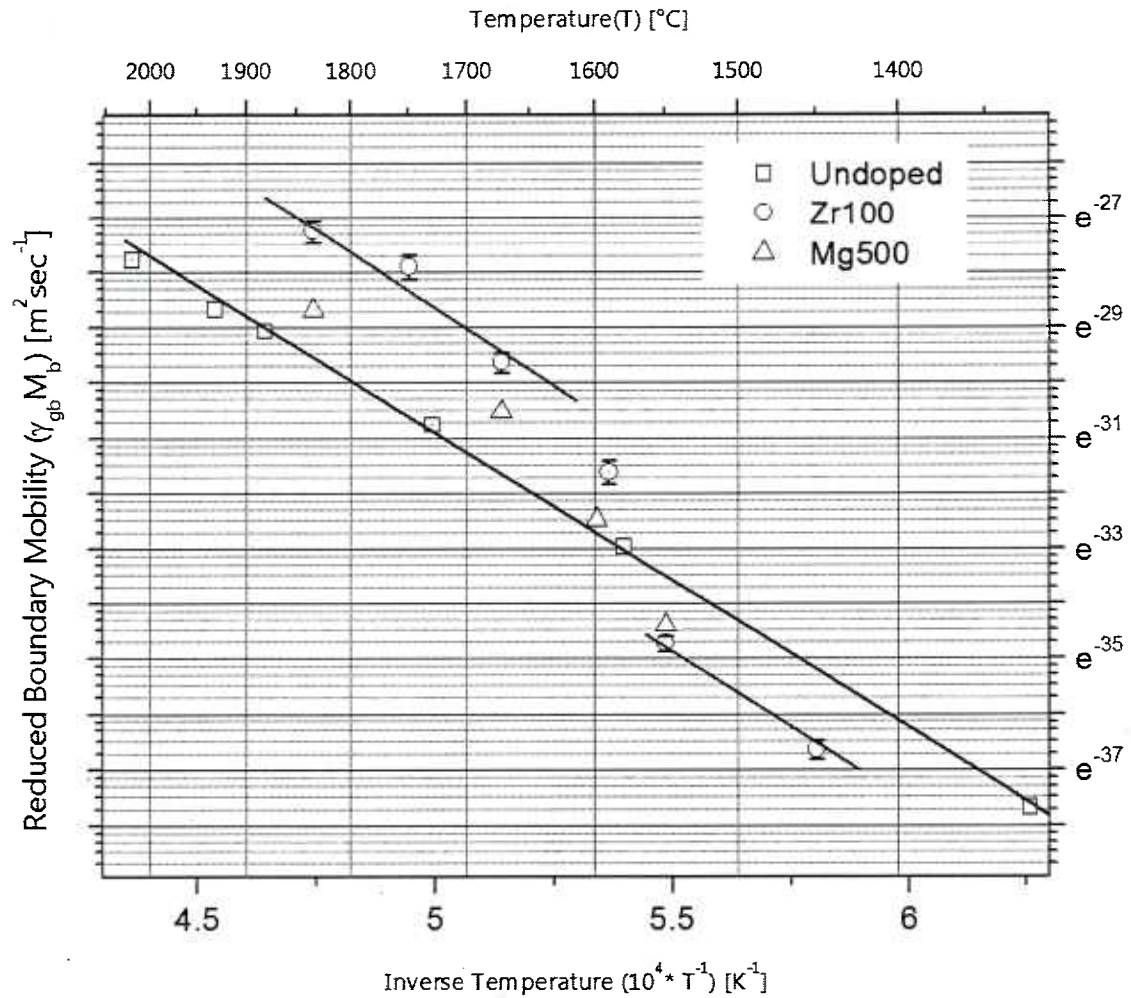


Figure 5.23: Reduced boundary mobility of 100 ppm of Zr doped alumina, indicating two regimes of growth; At temperatures  $<1550^\circ\text{C}$ , it is reduced as compared to undoped alumina, whereas it is higher than undoped alumina above  $1600^\circ\text{C}$ ; Zr-doped data courtesy: Shantanu Behera, PhD Dissertation, 2010, Lehigh University; Mg-doped and undoped data courtesy: Shen Dillon, PhD Dissertation, 2007, Lehigh University.

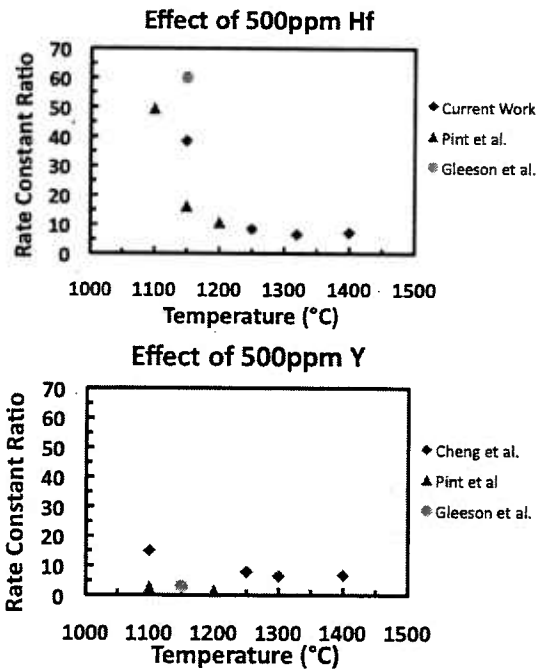


Figure 5.24: Graphs of the rate constant ratio as a function of temperature for (Left) 500ppm Hf doped samples. Two sets of data have been included in the plot besides the current work, which are Pint et al. [7, 42, 43] and Gleeson et al. [41] (Right) 500ppm Y doped samples. Three sets of data have been included in the plot, which are Cheng et al. [15], Pint et al. [7, 42] and Gleeson et al. [41]

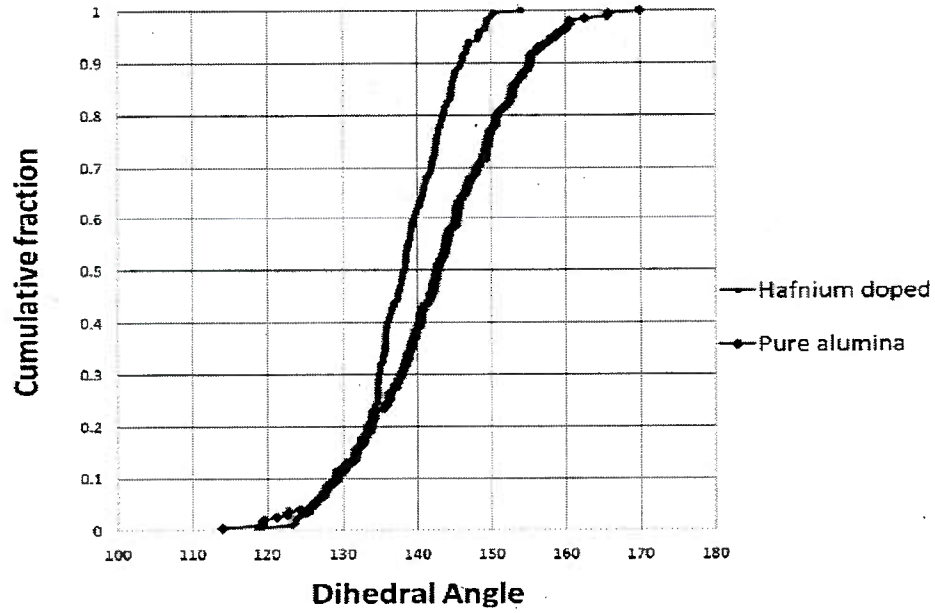


Figure 5.25: Influence of dopant on cumulative grain boundary dihedral angle distribution in alumina: blue line is undoped alumina; red line is 500ppm  $\text{HfO}_2$ -doped

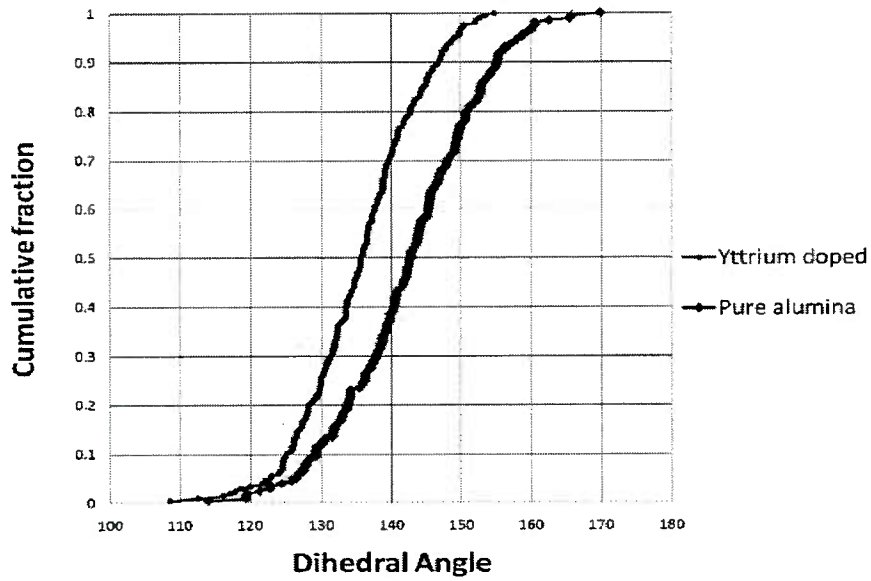


Figure 5.26: Influence of dopant on cumulative grain boundary dihedral angle distribution in alumina: blue line is undoped alumina; purple line is 500ppm  $\text{Y}_2\text{O}_3$ -doped

## ***Chapter 6. Conclusions and Suggested Future Work***

The first part of this work investigated the effect of doping levels of  $\text{HfO}_2$  on oxygen grain boundary transport in alumina, which contains uniformly distributed Ni metallic particles. The doping levels spanned the solubility limit ranging from 100ppm (below the solubility limit) to 2000ppm (well above the solubility limit). The plot of the ratio  $k_{\text{undoped}}/k_{\text{doped}}$  (grain-size corrected) as a function of dopant level clearly shows two behavior regimes: namely a regime I that encompasses doping levels below the solubility limit and a regime II where second-phase  $\text{HfO}_2$  particles were present in the microstructure. A clearer understanding of the influence of  $\text{HfO}_2$  doping on the transport behavior can be achieved by plotting the data with respect to the fractional grain boundary coverage ( $f$ ), as opposed to overall  $\text{HfO}_2$  content. The linear relationship can be rationalized with a site-blocking model, in which the  $\text{Hf}^{4+}$  ions obstruct the diffusive paths at the grain boundary.

The second part of the work is focused on the temperature dependence of the oxidation kinetics in  $\text{HfO}_2$  doped  $\text{Al}_2\text{O}_3$ . The activation energy and rate constant ratio determined from our work and compared with that for alloys studies indicated that multiple diffusion mechanisms might be operative at grain boundaries owing to boundary transitions that modify local structure and chemistry. Results of ARM characterization of samples oxidized at  $1150^\circ\text{C}$  have revealed boundary structures that differ from those observed in samples oxidized at  $1250^\circ\text{C}$  and  $1400^\circ\text{C}$ .

Specifically, new types of boundary structures are present at the lower temperature with a more atomically rough structure, and exhibit high energy facet planes such as  $\{0\ 0\ 0\ 6\}$  and  $\{2\ -1\ -1\ 3\}$  different from relatively low energy facet planes such as  $\{2\ -1\ -1\ 0\}$  and  $\{1\ 0\ -1\ 2\}$  for samples oxidized at higher temperature. These high-energy facet planes may be occupied with higher Hf segregation levels resulting in a much better oxidation resistance. The current results highlight the significant role of complexion transitions in oxidation, which has traditionally been neglected.

To better define the boundary transition temperature, expanding the data set in the lower temperature range will be essential, although it is a challenging proposition given the long time scales involved. By correlating the kinetic data with boundary structure observation, we can better understand the effect of RE dopants in this technologically important temperature regime. Moreover, as described in the earlier chapter, it is difficult to explain the additional benefit of Hf compared with Zr considering their similar ionic radii, charge. Similar temperature dependence studies can be applied to Zr. Zr doped samples might have a different grain boundary transition temperature compared with Hf. And it would also be of interest to carry out a similar study with either a different Hf dopant level or other RE such as Y. Moreover, the assumption that high energy facet planes may have higher Hf segregation level needs to be verified by conducting high spatial resolution EDX studies. An EELS study on the valence state of Hf will be also essential to consider the charge balance in the current system.

The current work has mainly focused on the effect of Hf-doping on the oxygen diffusion kinetics and it is well known that oxidation takes place by a combination of both oxygen inward diffusion and aluminum outward diffusion for many alumina formers. Interesting questions arise concerning the effect of Hf-doping on  $\text{Al}^{3+}$  diffusion. The HAADF-STEM images already demonstrated that extensive  $\text{Hf}^{4+}$  substitutes for  $\text{Al}^{3+}$  at the outer grain surfaces, which may indicate  $\text{Hf}^{4+}$  can block diffusion pathways for  $\text{Al}^{3+}$ . Considering there have been relative few studies of  $\text{Al}^{3+}$  diffusion transport in alumina due to the lack of an appropriate radioactive isotope, Cr was widely used. Previous studies in at Lehigh used a diffusion couple between  $\text{Cr}_2\text{O}_3$  and  $\text{Al}_2\text{O}_3$ , and the Cr concentration profile was measured as a function of annealing time and temperature. It was shown that 100ppm Y-doping retarded cation diffusion in the grain boundary regime by about an order of magnitude relative to undoped alumina, which acted more significantly on the pre-exponential factor.

Another suggestions for future work is to optimize the oxidation resistance by codoping two REs into the alumina. As described in Appendix B, initial screen tests show interesting results on the free surface, where La and Hf resulted in a “denuded” region with less spinel present on the free surface. The results indicate the interaction between La and Hf results in a slower Ni outward diffusion. Although the monolithic experiments with 500ppm Hf and 500ppm La co-doped samples did not present any additional benefit compared with singly doping, we believe over-doping complicated the current results. By examining 250ppm Hf and 250ppm La, or even lower doping levels, combined with HAADF-STEM to reveal the grain boundary structure and



chemistry, we can develop a better strategy to optimize the oxidation resistance of alumina formers.

## ***Chapter 7. Contribution***

Many researchers have sought to better understand the mechanisms by which oxidation is reduced by addition of REs. However, the complex chemistry of commercial high-temperature alloys makes a detailed analysis of these systems rather difficult. By using the Ni marker method, we can simplify the investigation of oxidation kinetics in a more controlled manner to study separate REs' effect. In the current work, firstly, we have successfully determined the dependence of the oxidation rate on dopant composition for  $\text{Hf}^{4+}$ , which is technologically important parameter in the gas turbine industry. The results allowed us to gain insight into the beneficial mechanism of RE doping, which can be used to study other dopant systems or combinations of dopants. Secondly, in analyzing the temperature dependence of the oxidation kinetics, we have seen strong evidence that multiple diffusion mechanisms are operative at grain boundaries owing to complexion transitions induced by temperature that modify the local structure and chemistry. The results highlight the significant role that complexion transitions play in oxidation, which is traditionally neglected from other research groups. More importantly, it builds bridges between alloy groups, who conducted experiments at relative lower temperature ( $< 1200^{\circ}\text{C}$ ) on thermal grown oxide and ceramicists, who performed diffusion study in polycrystalline alumina at relative higher temperature ( $>1400^{\circ}\text{C}$ ).

The results also provided significant insights into the long-term controversy to if and why  $\text{Hf}^{4+}$  has a greater low temperature benefit than  $\text{Y}^{3+}$ .

## *Appendices*

### *Appendix A: Calculating The Effect of Nickel Outward Diffusion on Oxidation Penetration Depth*

Figure A.1 shows a typical SEM image of a free surface for 500ppm Hf doped alumina/Ni oxidized at 1400°C for 5h, where the white phase is  $\text{NiAl}_2\text{O}_4$  spinel and the dark phase is alumina. By using ImageJ [Ref], an 8-bit image with only white and black contrast can be generated by adjusting threshold to convert spinel phase into white phase and alumina phase into dark phase, from which the area fraction of spinel phase  $\text{AF}_{\text{spinel}}$  can be obtained. Assuming the alumina sample has a volume equal to  $A \times L$  and Ni particles form clusters distributed uniformly in the matrix, therefore, the line density of Ni clusters in the sample can be described as:

$$(1) \quad \frac{A \times L \times 0.5\text{Vol}\%}{V_{\text{Ni cluster}}}$$

Where  $V_{\text{Ni cluster}}$  stands for the volume of Ni cluster.

$$(2) \quad \frac{0.15 \times \text{AF}_{\text{spinel}} \times \delta_{\text{spinel}} \times A}{V_{\text{Ni cluster}}}$$

Where 0.15 is the conversion factor for volume of spinel to volume of Ni,  $\delta_{\text{spinel}}$  is the width of spinel on the surface, which is around 0.8  $\mu\text{m}$  measured from the experiment. For Figure A.1, the  $AF_{\text{spinel}}$  is around 13%. By dividing expression (1) with (2), the equivalent length due to extra Ni outward diffusion is around 3  $\mu\text{m}$ . By using this method, equivalent length for all the samples under different heat treatment can be obtained for comparison.

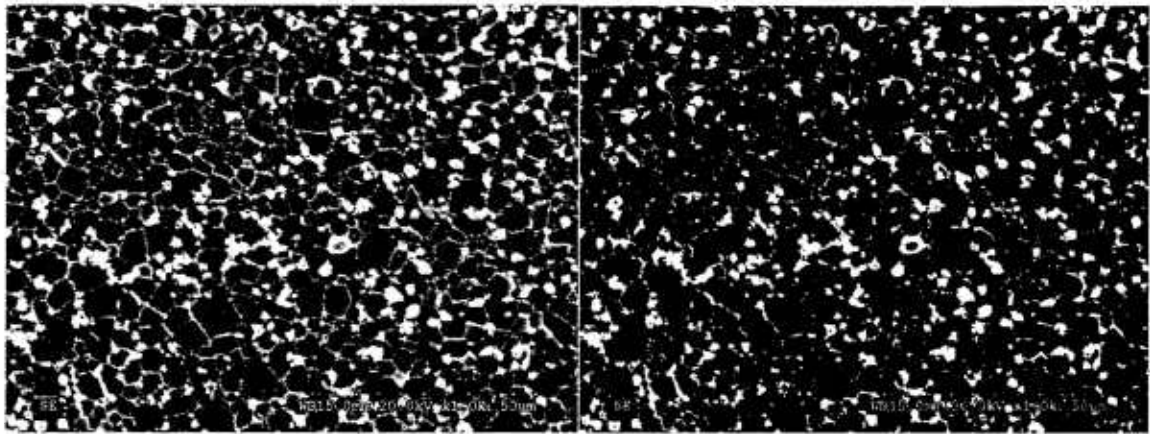


Figure A.1: (Left) Free surface for 500ppm Hf doped oxidized at 1400°C for 5h (right) 8-bit image with white and black contrast created by ImageJ [32]

## ***Appendix B: Hf and La Co-Doped Samples***

### ***B.1 Results***

With the demand for better oxidation resistance performance, strategies such as adding multiple REs are attractive. Many researchers have studied the influence of single RE or multiple REs on the oxidation rate of commercial alloys in order to elucidate the controlling mechanism. Promising data have been found in a combination of Hf and Y [78] or La and Y [79, 80], however, a full explanation of the underlying mechanism is not yet available.

In the case of the co-doped work, a series of screening studies were first conducted to help identify combinations of dopants that were potentially beneficial. In these experiments, composite samples were fabricated composed of (Ni-containing) alumina layers singly doped with different reactive element (RE) ions. The sintered

samples were subjected to annealing in an oxidizing atmosphere, and the degree of surface spinel formation was characterized, as well as the depth of the oxidation layer. Figure B.1 depicts the surface of a bilayer sample composed of 500ppm La-doped alumina bonded to a 500ppm Hf-doped alumina. In the area of the interface, it can be seen that the density of spinel second phase is reduced, suggesting a positive interaction between the dopants. Motivated by these results, it was decided to investigate monolithic samples co-doped with 500 ppm Hf and 500 ppm La. Then the behavior of the co-doped composition was compared with that of samples singly doped with either Hf or La.

Figure B.2 (LHS) shows a typical SEM image of 500ppm Hf and 500ppm La co-doped alumina containing 0.5 vol% Ni after oxidation for 60h at 1400°C with BSE contrast. In the subsurface, metallic Ni particles react with oxygen to form nickel aluminate spinel ( $\text{NiAl}_2\text{O}_4$ ), which is a larger gray phase compared with bright Ni particles. The oxidation zone has been marked in which the nickel particles have been replaced by spinel. A clearer image in the oxidation zone is shown in Figure B.2 (RHS). Besides the expected Ni spinel gray phase, two other phases have also been revealed. One phase is Hf oxide, which is identified as Monolithic  $\text{HfO}_2$ . The other one is a La-containing phase, which was observed both in the oxidized region and non-oxidized regions. Based on the  $\text{La}_2\text{O}_3$ - $\text{Al}_2\text{O}_3$  phase diagram, this La containing phase was most likely lanthanum hexa-aluminate,  $\text{LaAl}_6\text{O}_{13}$  that exhibits the magnetoplumbite structure. [81, 82, 83] The occurrence of many small  $\text{HfO}_2$  particles indicated that the solubility limit of both the bulk and grain boundaries had been

reached. To investigate the co-doped effect on oxygen grain boundary diffusion, a kinetic study measuring the oxidation penetration depth  $x$ , plotting its square  $x^2$  as a function of oxidation time  $t$  has been performed, as shown in Figure B.3. Clearly, the smaller the  $k_c$  is, the slower the oxygen diffusion will be.

## ***B.2 Discussion***

As shown in table B.1, compared with undoped alumina after grain size correction, the co-doped sample behaved similar to the 500ppm Hf doped sample, which can reduce the  $k_c$  by a factor about 7 to 8, while 500ppm La alone can only reduce it slightly. Early studies on creep [Ref] found that the co-doping of RE elements with widely differing values of ionic radii, such as  $Zr^{4+}$  (0.72Å) and  $Nd^{3+}$  (1.00Å), resulted in a lower creep rate than the singly doped compositions. Further, Zr-Nd co-doping was more beneficial than dopant pairs with similar ionic radii, such as  $Sc^{3+}$  (0.73Å) and  $Zr^{4+}$  (0.72Å). Therefore, considering the ionic radius for  $Hf^{4+}$  (0.71Å) and  $La^{3+}$  (1.06Å), it is reasonable to speculate the co-doped sample might result in a lower oxidation rate compared to singly doped samples. However, the results were contrary to our initial expectation. One possible explanation is that not enough La segregated to the grain boundaries due to the formation of the La-rich second phase, which resulted in a high level of Hf in the grain boundaries and hence with a similar reduction rate compared with Hf doped alone. Atomic resolution HAADF-STEM

should be utilized to study the composition and grain boundary structure of codoped and singly doped samples. Another possibility is that compared with La, Hf has a much higher preference to segregate in the grain boundaries. Since the current doping level was already greatly over the solubility limit, reducing the doping level to 250ppm Hf and 250ppm La or even lower total combination might be a good way to reevaluate the co-doped effect, which could also reduce the effect of the extensive presence of Hf-rich and La-rich second phase particles. It is also noteworthy in Figure B.1 that the interaction between Hf and La could result in a decrease in Ni outward diffusion. Could the co-doped of Hf and La result in a much lower cation diffusivity?

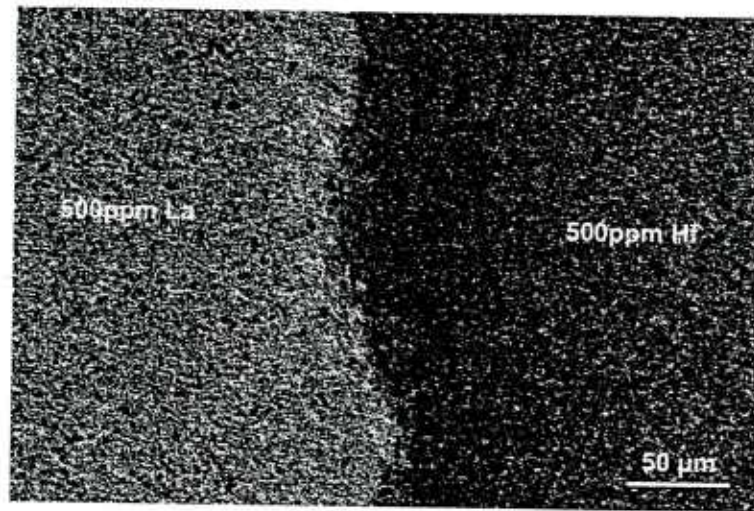


Figure B.1: Free surface of bilayer sample composed of 500 ppm La doped alumina bonded to 500ppm Hf-doped alumina. The sample was subjected to an oxidation heat-treatment of 5h at 1400 °C. The dashed lines designate the interfacial region where the density of spinel is lower. (SEM, secondary electron contrast).



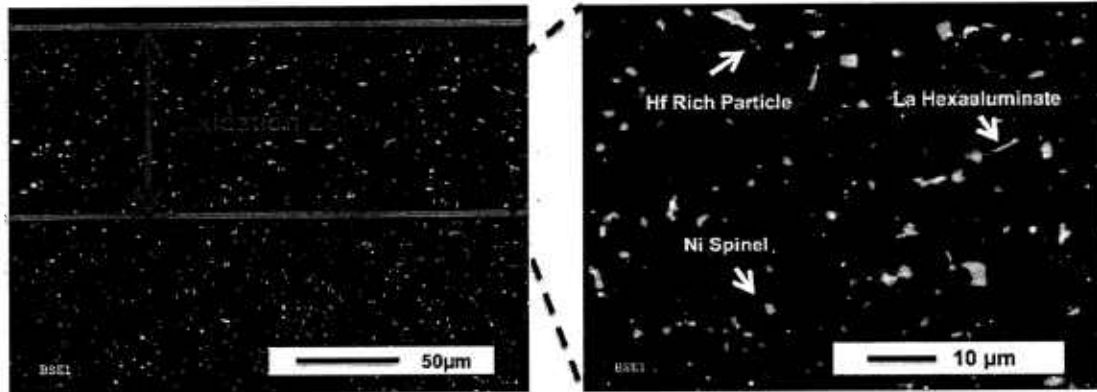


Figure B.2 (LHS) Scanning electron microscope image showing the cross section of 500ppm Hf and 500ppm La co-doped alumina after oxidation for 60h at 1400°C (backscattered electron contrast) (RHS) Enlarged image of dotted box in Figure 1 showing Hf rich particles, nickel aluminate spinel and La hexaaluminates within the oxidation zone (backscattered electron contrast)

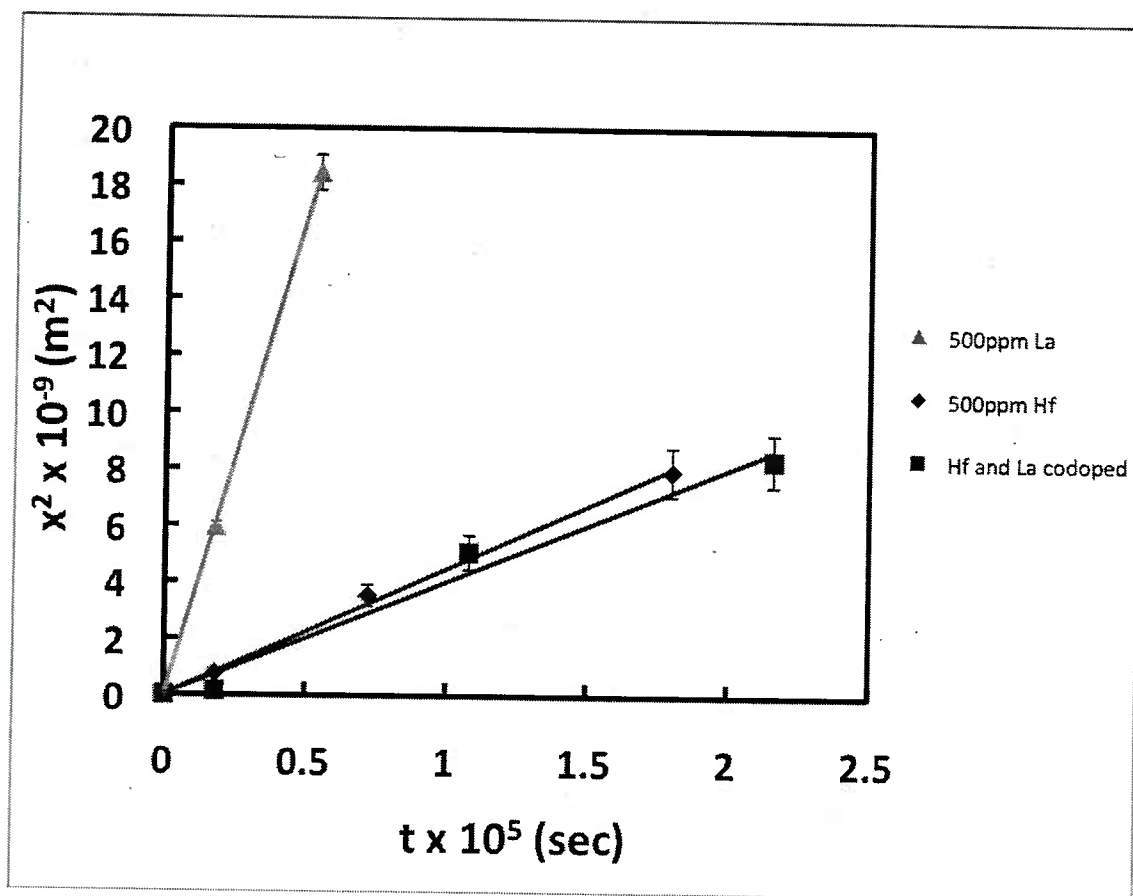


Figure B.3 Graph of the average of the square of the thickness of the oxidized layer,  $x$ , versus oxidation time  $t$  for different samples oxidized at the same temperature  $1400^\circ\text{C}$ , including 500ppm Hf doped, 500ppm La doped, 500ppm Hf and 500ppm La codoped. The results are averaged over 10 areas, with the error bars representing the standard deviation in  $x^2$ . The straight lines are least-squares fits to the data.

Table B.1 Comparison of values of the parabolic rate constants for different samples

| 1400°C            | $k_c$ (m <sup>2</sup> /s)         | $k_{\text{undoped}}/k_{\text{doped}}$ | $k^c_{\text{undoped}}/k^c_{\text{doped}}$ |
|-------------------|-----------------------------------|---------------------------------------|---|
| Undoped           | $7.77 \times 10^{-13}$            |                                       |   |
| 500ppm La         | $(3.33 \pm 0.12) \times 10^{-13}$ | $2.3 \pm 0.1$                         | $1.2 \pm 0.1$                             |
| 500ppm Hf         | $(4.48 \pm 0.44) \times 10^{-14}$ | $17.3 \pm 1.7$                        | $7.1 \pm 0.8$                             |
| Hf and La codoepd | $(4.01 \pm 0.45) \times 10^{-14}$ | $19.4 \pm 2.4$                        | $8.2 \pm 1.0$                             |

## ***Bibliography***

1. P. Y. Hou, "Impurity Effects on Alumina Scale Growth," *J. Am. Ceram. Soc.*, 86 [4] (2003) 660-68
2. B. A. Pint, J. R. DiStefano, I. G. Wright, "Oxidation Resistance: One Barrier to Moving beyond Ni-base Superalloys," *Mater. Sci. Eng., A* 415[1-2] (2006) 255-63
3. N. P. Padture, M. Gell, E. H. Jordan, "Thermal Barrier Coatings for Gas-Turbine Engine Applications," *Science*, 296, (2002) 280-84
4. B. A. Pint, I. G. Wright, W. Y. Lee, Y. Zhang, K. Prubner and K. B. Alexander, "Substrate and Bond Coat Compositions: Factors Affecting Alumina Scale Adhesion," *Mater. Sci. Eng., A* 245 (1998) 201-11
5. B. A. Pint, J. A. Haynes, K. L. More, I. G. Wright and C. Leyens, "Compositional Effects on Aluminide Oxidation Performance: Objectives for Improved Bond Coats," *Superalloys* 629-38 (2000)
6. B. A. Pint, K. L. More, P. F. Tortorelli, W. D. Porter and I. G. Wright, "Optimizing the Imperfect Oxidation Performance of Iron Aluminides," *Mater. Sci. Forum*, 369-372 (2001) 411-8
7. B. A. Pint, K. L. More and I. G. Wright, "Effect of Quaternary Additions on the Oxidation Behavior of Hf-Doped NiAl," *Oxid. Met.*, 59 (2003) 257-79
8. T. Izumi and B. Gleeson, "Oxidation Behavior of Pt+Hf-modified gamma-Ni+gamma'-Ni<sub>3</sub>Al Alloys," *Mater. Sci. Forum*, 522-523 (2006) 221-28
9. D. Naumenko, V. Kochubey, L. Niewolak, A. Dymiaty, J. Mayer, L. Singheiser, W. J. Quadakkers, "Modification of Alumina Scale Formation on FeCrAlY Alloys by Minor Additions of Group IVa Elements," *J. Mater. Sci.*, 43(2008) 4550-560
10. J. Cho, C. M. Wang, H. M. Chan, J. M. Rickman, and M. P. Harmer, "Role of Segregating Dopants on the Improved Creep Resistance of Aluminum Oxide," *Acta Mater.*, 47 [15] (1999) 4197- 207

11. Y. Li, C. M. Wang, H. M. Chan, J. M. Rickman, and M. P. Harmer, "Codoping of Alumina to Enhance Creep Resistance, " J. Am. Ceram. Soc., 82[6] (1999) 1497-504
12. J. P. Buban, K. Matsunaga, J. Chen, N. Shibata, W. Y Ching, T. Yamamoto, and Y. Ikumura, " Grain Boundary Strengthening in Alumina by Rare Earth Impurities," Science, 311 (2005) 3129-35
13. I. Milas, B. Hinnemann, and E. A. Carter, "Structure of and Ion Segregation to an Alumina Grain Boundary: Implications for Growth and Creep," J. Mater. Res., 23 (2008) 1494
14. A. H. Heuer and D. B. Hovis, "Alumina Scale Formation: A New Perspective," J. Am. Ceram. Soc., 94[S1] (2011) S146-53
15. H. K. Cheng, S. J. Dillon, H.S. Caram, J.M. Rickman, H.M. Chan and M.P. Harmer, "The Effect of Yttrium on Oxygen Grain Boundary Transport in Polycrystalline Alumina Measured Using Ni Marker Particles," J. Am. Ceram. Soc., 91 (2008) 2002-2008
16. T. C. Wang, R. Z. Chen and W. H. Tuan, " Oxidation Resistance of Ni-Toughened  $\text{Al}_2\text{O}_3$ ," J. Eur. Ceram. Soc., 23, (2003) 927-34
17. M. Nanko, "High-Temperature Oxidation of Ceramic Matrix Composites Dispersed with Metallic Particles," Sci. Technol. Adv. Mater., 6, (2005) 129-34
18. V. K. Tolpygo, D. R. Clarke, "Microstructural Evidence for Counter Diffusion of Aluminum and Oxygen during the Growth of Alumina Scales," Mater. High Temp., 20 (2003) 261-73
19. B. A. Pint, J. R. Martin, L. W. Hobbs, " $^{18}\text{O}$ / SIMS Characterization of the Growth Mechanisms of Doped and Undoped  $\alpha\text{-Al}_2\text{O}_3$ ," Oxid. Met., 39 (1993) 167-95
20. B. A. Pint, "Experimental Observations in Support of the Dynamic Segregation Theory to Explain the Reactive Element Effect," Oxid. Met., 45, 1-37. (1996)

21. G. Tatlock, D. Ram and P. Wang, "High Spatial Resolution Imaging of the Segregation of Reactive Elements to Oxide Grain Boundaries in Alumina Scales", *Mat. High Temp.*, 26, 293-298 (2009)
22. Z. Yu, Q. Wu, J. M. Rickman, H. M. Chan and M. P. Harmer, "Atomic-Resolution Observation of Hf-doped Alumina Grain Boundaries," *Scripta Mater.*, 68 (9) 2013 703-06
23. M. J. Saxton, "Anomalous Diffusion Due to Obstacles: A Monte Carlo Study," *Biophys. J.*, 66 (1994) 394-401
24. J. Cho, C. M. Wang, H. M. Chan, J. M. Rickman and M. P. Harmer, "Improved Tensile Creep Properties of Yttrium – and Lanthanum –doped Alumina: A Solid Solution Effect," *J. Mater. Res.*, 16[2] (2001) 425-29
25. C. M. Wang, J. Cho, H. M. Chan, J. M. Rickman and M. P. Harmer, "Influence of Dopant Concentration on Creep Properties of Nd<sub>2</sub>O<sub>3</sub>- Doped Alumina," *J. Am. Ceram. Soc.*, 84[5] (2001) 1010-16
26. H. K. Cheng, H. S. Caram, W. E. Schiesser, J. M. Rickman, H. M. Chan and M. P. Harmer, "Oxygen Grain Boundary Transport in Polycrystalline Alumina Using Wedge-geometry Bilayer Samples: Effect of Y-Doping," *Acta Mater.*, [58] (2010) 2442-45
27. M. D. Drahos, H. M. Chan, J. M. Rickman, M. P. Harmer, "Densification and Grain Growth of Fe-doped and Fe/Y codoped Alumina: Effect of Fe Valency," *J. Am. Ceram. Soc.*, 88 (12) (2005) 3369-73
28. T. Matsudaira, M. Wada, S. Kitaoka, "Effect of Dopants on the Distribution of Aluminum and Oxygen Fluxes in Polycrystalline Alumina under Oxygen Potential Gradients at High Temperatures," *J. Am. Ceram. Soc.*, 1-9 (2013)
29. H. M. Hindam, W. W. Smeltzer, "Growth and Microstructure of  $\alpha$ -Al<sub>2</sub>O<sub>3</sub> on  $\beta$ -NiAl," *J. Electrochem. Soc.*, 127, (1980) 1630-5
30. I. G. Wright, B. A. Pint, and P. F. Tortorelli, "High-Temperature Oxidation Behavior of ODS- Fe<sub>3</sub>Al," *Oxid. Met.*, 55 (2001) 333-57
31. A. H. Heuer, T. Nakagawa, M. Z. Azar, D. B. Hovis, J. L. Smialek, B. Gleeson, N. D. M. Hine, H. Guhl, H. -S. Lee, P. Tangney, W. M. C.

- Foulkes, M. W. Finnis, "On the Growth of  $\text{Al}_2\text{O}_3$  Scales," *Acta. Mater.*, 61 (2013) 6670-83
32. S. J. Dillon, M. P. Harmer, "Multiple Grain Boundary Transitions in Ceramics: A Case Study of Alumina," *Acta Mater.*, [55] (2007) 5247-54
  33. S. J. Dillon, M. Tang, W. C. Carter and M. P. Harmer, "Complexion: A New Concept for Kinetic Engineering in Materials Science and Beyond," *Acta Mater.*, [55] (2007) 6208-6218
  34. Shantanu K. Behera. Atomic Structural Features of Dopant Segregated Grain Boundary Complexions in Alumina by EXAFS. PhD thesis, Lehigh University, 2010
  35. W. W. Mullins, "Theory of Thermal Grooving," *J. Appl. Phys.* 28 (1957) 333-39
  36. W. Swiantnicki, S. Lartigue-Korinek and J. Y. Laval, "Grain Boundary Structure and Intergranular Segregation in  $\text{Al}_2\text{O}_3$ ," *Acta Metall. Mater.*, 43[2] (1995) 795-805
  37. Y. Pang and P. Wynblatt, "Correlation Between Grain-Boundary Segregation and Grain-Boundary Plane Orientation in Nb-Doped  $\text{TiO}_2$ ," *J. Am. Ceram. Soc.*, 88[8] (2005) 2286-91
  38. M. Kitayama and A. M. Glaeser, "The Wulff Shape of Alumina: III, Undoped Alumina," *J. Am. Ceram. Soc.*, 85[3] (2002) 611-22
  39. S. Galmarini, U. Aschauer, A. Tewari, Y. Aman, C. Van Gestel, P. Bowen, "Atomistic Modeling of Dopant Segregation in  $\alpha$ -Alumina Ceramics: Coverage Dependent Energy of Segregation and Nominal Dopant Solubility," *J. Eur. Ceram. Soc.*, 31 (2011) 2839-52
  40. D. Y. Yoon and Y. K. Cho, "Roughening Transition of Grain Boundaries in Metals and Oxides," *J. Mater. Sci.*, 40 (2005) 861-70
  41. B. Gleeson, Personnel Communication, (2010)
  42. J. A. Haynes, B. A. Pint, K. L. More, Y. Zhang and I. G. Wright, "Influence of Sulfur, Platinum, and Hafnium on the Oxidation Behavior of CVD NiAl Bond Coatings," *Oxid. Met.*, 58 (2002) 513-44

43. B. A. Pint, "The Oxidation Behavior of Oxide-Dispersed  $\beta$ -NiAl: I. Short-Term Performance at 1200°C," *Oxid. Met.*, 49 (1998) 531-59
44. G. S. Rohrer, "Grain Boundary Energy Anisotropy: A Review," *J. Mater. Sci.* 46 (2011) 5881-95
45. R. M. German and S. J. Park, 2008, *Handbook of Mathematical Relations in Particulate Materials Processing*, Wiley-Interscience, New York.
46. P. R. Cantwell, M. Tang, S. J. Dillon, J. Luo, G. S. Rohrer, M. P. Harmer, "Grain Boundary Complexions," *Acta Mater.*, 62 (2014) 1-48
47. S. A. Bojarski, M. Stuer, Z. Zhao, P. Bowen, and G. S. Rohrer, "Influence of Y and La Additions on Grain Growth and the Grain-Boundary Character Distribution of Alumina," *J. Am. Ceram. Soc.*, 97[2] (2014) 622-30
48. Shen J. Dillon. Relationship between Grain Boundary Complexion and Grain Growth Kinetics in Alumina. PhD thesis, Lehigh University, 2007
49. Basic Configuration of a Spark Plasma Sintering (SPS) Machine, retrieved from <http://www.thermaltechnology.com/spark-plasma-sintering.html>.
50. Spark Plasma Sintering (SPS) Machine Model 10-4, retrieved from <http://www.thermaltechnology.com/spark-plasma-sintering.html>.
51. R. Wirth, "Focused Ion Beam (FIB): A Novel Technology for Advanced Application of Micro- and Nanoanalysis in Geosciences and Applied Mineralogy," *Eur J. Mineral.*, [16] (2004) 863-76
52. NanoMill® TEM specimen preparation system, Model 1040, retrieved from <http://www.fischione.com/products/ion-beam-preparation/model-1040-nanomill®-tem-specimen-preparation-system>
53. R. J. Keyse, A. J. Garratt-Reed, P. J. Goodhew, G. W. Lorimer, "Introduction to Scanning Transmission Electron Microscopy," Springer, New York, Page 50-51.
54. J. Luo, H. K. Cheng, K. M. Asl, C. J. Kiely, M. P. Harmer, "The Role of a Bilayer Interfacial Phase on Liquid Metal Embrittlement," *Science.*, [333] 1730 (2011) 1730-33



55. W. Cao, A. Kundu, Z. Yu, M. P. Harmer, R. P. Vinci, " Direct Correlations between Fracture Toughness and Grain Boundary Segregation Behavior in Ytterbium-doped Magnesium Aluminate Spinel," *Scripta Mater.*, [69] (2013) 81-84
56. K. Tai, L. Feng, S. J. Dillon, "Kinetics and Thermodynamics associated with Bi Adsorption Transitions at Cu and Ni Grain Boundaries," *J. App. Phys.*, [113] 19 (2013) 193507
57. S. Ma, P. R. Cantwell, T. J. Pennycook, N. X. Zhou, M. P. Oxley, D. N. Leonard, S. J. Pennycook, L. Luo, M. P. Harmer, " Grain Boundary Complexion Transitions in WO<sub>3</sub>- and CuO-doped TiO<sub>2</sub> Bicrystals," *Acta Mater.*, [61] 5 (2013) 1691-1704
58. S. A. Bojarski, S. Ma, W. Lenthe, M. P. Harmer, G. S. Rohrer, " Changes in the Grain Boundary Character and Energy Distributions Resulting from a Complexion Transition in Ca-Doped Yttria," *Metall. Mater. Trans. A.*, [43A] 10 (2012) 3532-38
59. S. Ma, K. M. Asl, C. Tansarawiput, P. R. Cantwell, M. Qi, M. P. Harmer, J. Luo, "A Grain Boundary Phase Transition in Si-Au," *Scripta Mater.*, [66] 5 (2012) 203-6
60. L. K. V. Lou, T. E. Mitchell, A. H. Heuer, "Impurity Phases in Hot-Pressed Si<sub>3</sub>N<sub>4</sub>," *J. Am. Ceram. Soc.*, [61] (1978) 392-6
61. K. V. Benthem, A. R. Lupini, M. P. Oxley, S. D. Findlay, L. J. Allen, S. J. Pennycook, " Three-dimensional ADF Imaging of Individual Atoms by Through-Focal Series Scanning Transmission Electron Microscopy, " *Ultramicroscopy*, [106] (2006) 1062-68
62. S. J. Pennycook, " Z-Contrast STEM for Materials Science," *Ultramicroscopy* [30], (1989) 58-69
63. S. J. Pennycook, D. E. Jesson, A. J. McGibbon, P. D. Nellist, " High Angle Dark Field STEM for Advanced Materials," *J. Electron Microsc.* [45], (1996) 36-43

64. S. J. Dillon, M. P. Harmer and G. S. Rohrer, "Influence of Interface Energies on Solute Partitioning Mechanisms in Doped Alumina," *Acta Mater.*, [58] (2010) 5097-5108
65. S. J. Dillon, M. P. Harmer and G. S. Rohrer, "The Relative Energies of Normal and Abnormal Grain Boundaries Displaying Different Complexions," *J. Am. Ceram. Soc.*, [93], (2010) 1796-1802
66. K. B. Amissah, J. M. Rickman, H. M. Chan, and M. P. Harmer, "Grain-Boundary Diffusion of Cr in Pure and Y-Doped Alumina," *J. Am. Ceram. Soc.*, 90[5] (2007) 1551-5
67. B. A. Pint, A. J. Garratt-Reed, and L. W. Hobbs, "Possible Role of the Oxygen Potential Gradient in Enhancing Diffusion of Foreign Ions on  $\alpha$ - $\text{Al}_2\text{O}_3$  Grain Boundaries," *J. Am. Ceram. Soc.*, 81[2] (1998) 305-14
68. J. Blamain, M. K. Loudjani, A. M. Huntz, "Microstructural and Diffusional Aspects of The Growth of Alumina Scales on  $\beta$ -NiAl," *Mater Sci Eng A*, [224] (1997) 87-100
69. T. A. Ramanarayanan, M. Raghavan and R. Petkovic-Luton, "Metallic Yttrium Additions to High Temperature Alloys: Influence on  $\text{Al}_2\text{O}_3$  Scale," *Oxid. Met.* 22 (1984) 83-100
70. T. Matsudaira, M. Wada, T. Saitoh, S. Kitaoka, "The Effect of Lutetium on Oxygen Permeability of Alumina Polycrystals under Oxygen Potential Gradients at Ultra-High Temperatures," *Acta Mater.*, [58] (2010) 1544-53
71. A. H. Heuer, "Oxygen and Aluminum Diffusion in  $\alpha$ - $\text{Al}_2\text{O}_3$ : How Much Do We Really Understand?" *J. Eur. Ceram. Soc.*, 28 (2008) 1495-1507
72. T. Nakagawa, H. Nishimura, I. Sakaguchi, N. Shibata, K. Matsunaga, T. Yamamoto and Y. Ikuhara, "Grain Boundary Character Dependence of Oxygen Grain Boundary Diffusion in  $\alpha$ - $\text{Al}_2\text{O}_3$  Bicrystals," *Scripta Mater.* [65] (2011) 544-47
73. J. Klöwer, "Factors Affecting The Oxidation Behaviour of Thin Fe-Cr-Al Foils Part II: The Effect of Alloying Elements: Overdoping," *Materials and Corrosion*, [51] (2000) 373-85

74. B. A. Pint, I. G. Wright, W. Y. Lee, Y. Zhang, K. Prubner, K. B. Alexander, " Substrate and Bond Coat Compositions: Factors Affecting Alumina Scale Adhesion," *Mater Sci. and Eng. A.*, [245] (1998) 201-11
75. B. A. Pint, J. H. Schneibel, " The Effect of Carbon and Reactive Element Dopants on Oxidation Lifetime of FeAl," *Scripta Mater.*, [52] (2005) 1199-1204
76. D. Naumenko, J. Le-Coze, E. Wessel, W. Fischer, W. J. Quadakkers, "Effect of Trace Amounts of Carbon and Nitrogen on the High Temperature Oxidation Resistance of High Purity FeCrAl Alloys," *Materials Transactions*, [43] (2002) 168-172
77. B. A. Pint, "Progress in Understanding the Reactive Element Effect Since the Whittle and Stringer Literature Review," in *Proc. John Stringer Symposium on High Temperature Corrosion*, P. F. Tortorelli, I. G. Wright, and P. Y. Hou (eds.), ASM International, Materials Park, OH, (2003) 9-19
78. B. A. Pint, " Optimization of Reactive Element Additions to Improve Oxidation Performance of Alumina-forming Alloys," *J. Am. Ceram. Soc.*, 86 [4] 686–95 (2003)
79. K. Harris, J. B. Wahl, " Improved Single Crystal Superalloys, CMSX-4 (SLS) [La+Y] and CMSX-486," *Superalloys 2004*, TMS, Warrendale, PA, 2004 p.45
80. K. A. Unocic, C. M. Parish, B. A. Pint, "Characterization of the Alumina Scale Formed on Coated and Uncoated Doped Superalloys," *Surf. Coat. Technol.*, [206] (2011) 1522-28
81. M. K. Cinibulk, " Thermal Stability of Some Hexaluminates at 1400°C," *J. Mater. Sci. Lett.*, [14] (1995) 651-54
82. P. E. D. Morgan, D. B. Marshall, R. M. Housley, " High Temperature Stability of Monazite-Alumina Composites," *Mater. Sci. Eng., A* [195] (1995) 215-22
83. N. Zahra, W. P. Monika, S. Florian, " Thermal Properties of Homogenous Lanthanum Hexaaluminate/Alumina Composite Ceramics," *J. Eur. Ceram. Soc.*, [30] (2010) 3103-9

84. T. M. Pollock, S. Tin, "Nickel- Based Superalloys for Advanced Turbine Engines: Chemistry, Microstructure, and Properties," J. Propulsion and Power, [22] 2 (2006) 362-74
85. K. A. Marino, B. Hinnemann, E. A. Carter, " Atomic-Scale Insight and Design Principles for Turbine Engine Thermal Barrier Coatings from Theory," PNAS, [108] 14 (2011) 5480-87
86. D. R. Clarke, C. G. Levi, " Materials Design for The Next Generation Thermal Barrier Coatings," Annu. Rev. Mater. Res [33] (2003) 383-417
87. J. C. Zhao, J. H. Westbrook, " Ultrahigh-Temperature Materials for Jet Engines, " MRS bulletin (2003) 622-27
88. R. A. Miller, " Thermal Barrier Coatings for Aircraft Engines: History and Directions, " J. Therm. Spray Technol. 6(1) (1997) 35-42
89. V. Sergo, D. R. Clarke, " Observation of Subcritical Spall Propagation of A Thermal Barrier Coating, " J. Am. Ceram. Soc., 81 (12) (1998) 3237-42
90. T. A. Ramanarayanan, R. Ayer, R. Petkovic-Luton, D. P. Leta, " The influence of Yttrium on Oxide Scale Growth and Adherence," Oxid. Met., 29 (5-6) (1998) 445-72
91. J. Jedlinski, S. Mrowec, " The Influence of Implanted Yttrium on The Oxidation Behaviour of  $\beta$ -NiAl," Mater. Sci. Eng., 87 (1987) 281-87
92. E. W. A. Young, J. H. W. D. Wit, " The Use of An  $^{18}\text{O}$  Tracer and Rutherford Backscattering Spectrometry to Study The Oxidation Mechanism of NiAl, ", Solid State Ionics 16 (1985) 39-46
93. K. P. R. Reddy, J. L. Smialek, A. R. Cooper, "  $^{18}\text{O}$  Tracer Studies of  $\text{Al}_2\text{O}_3$  Scale Formation on NiCrAl Alloys, " Oxid. Met., 17 (1982) 429-49
94. W. J. Quadakkers, H. Holzbrecher, K. G. Bräse, H. Beske, " Difference in Growth Mechanisms of Oxide Scales Formed on ODS and Conventional Wrought Alloys," Oxid. Met., 32 (1989) 67-88
95. D. F. Mitchell, R. Prescott, M. J. Graham, J. Doychak, " SIMS Studies of Oxide Growth on  $\beta$ -NiAl," in: 3<sup>rd</sup> International SAMPE metals conference, 1992

96. E. W. A. Young, H. E. Bishop, J. H. W. D. Wit, "On The Use of Markers and Tracers to Establish The Growth Mechanism of Alumina Scales during High Temperature Oxidation," *Surf. Inter. Analysis* 9 (1986) 163-68
97. J. A. Nychka, D. R. Clarke, "Quantification of Aluminum Outward Diffusion during Oxidation of FeCrAl Alloys," *Oxid. Met.*, 63 (2005) 325-52
98. J. Stringer, "The Reactive Element Effect in High-Temperature Corrosion," *Mater. Sci. Eng. A* 120 (1989) 129-37
99. T. Amano, S. Yajima, Y. Saito, "High-Temperature Oxidation Behavior of Fe-20Cr-4Al Alloys with Small Additions of Cerium," *Transactions of the Japan Institute of Metals* 20 (8) (1979) 431-41
100. J. Nowok, "Formation Mechanisms of Keying or Pegging Yttrium Oxide and Increased Plasticity of Alumina Scale on FeCrAlY," *Oxid. Met.*, 18 (1-2) (1982) 1-17
101. J. D. Kuenzly, D. L. Douglass, "The Oxidation Mechanism of Ni<sub>3</sub>Al Containing Yttrium," *Oxid. Met.*, 8 (3) (1974) 139-77
102. K. B. Amissah, J. M. Rickman, H. M. Chan, M. P. Harmer, "Grain-Boundary Diffusion of Cr in Pure and Y-Doped Alumina," *J. Am. Ceram. Soc.*, 90 [5] (2007) 1551-1555
103. M. L. Gall, B. Lesage, "Self Diffusion in  $\alpha$ -Al<sub>2</sub>O<sub>3</sub> I. Aluminum Diffusion in Single Crystals," *Philosophical Magazine* A70 (5) (1994) 761-73
104. A. E. Paladino, W. D. Kingery, "Aluminum Ion Diffusion in Aluminum Oxide," *J. Chem. Phys.*, 37 (5) (1962) 957-62
105. L. G. Harrison, "Influence of Dislocations on Diffusion Kinetics in Solids with Particular Reference to The Alkali Halides," *Transactions of the Faraday Society* 57 (1961) 1191-99
106. J. C. Fisher, "Calculation of Diffusion Penetration Curves for Surface and Grain Boundary Diffusion," *J. Applied Physics* 22 (1) (1951) 74-77
107. R. T. P. Whipple, "Concentration Contours in Grain Boundary Diffusion," *Philosophical Magazine* 45 (1954) 1225-36

108. A. D. Le Claire, "The Analysis of Grain Boundary Diffusion Measurements," *British Journal of Applied Physics* 14 (1963) 351-56
109. Y. Mishin, C. Herzig, "Grain Boundary Diffusion: Recent Progress and Future Research," *Mater. Sci. Eng. A.*, [260] (1999) 55-71
110. T. Suzuoka, "Lattice and Grain Boundary Diffusion in Polycrystals", *Mater. Trans., JIM*, 2 (1961) 25-32
111. A. Benninghoven, F. G. Rudenauer, H. W. Werner, *Secondary Ion Mass Spectrometry: Basic Concepts, Instrumental Aspects, Applications, and Trends*, John Wiley & Sons, New York, NY, 1989
112. C. M. Barshick, D. C. Duckworth, D. H. Smith (Eds.), *Inorganic Mass Spectrometry: Fundamentals and Applications*, Marcel Dekker, Inc., New York, 2000
113. N. Birks, G. Meier, *Introduction to High Temperature Oxidation of Metals*, Arnold, London, 1993
114. A. H. Heuer, T. Nakagawa, M.Z. Azar, P. B. Hovis, J. L. Smialek, B. Gleeson, N. D. M. Hine, H. Guhl, H. S. Lee, P. Tangney, W. M. C. Foulkes, M. W. Finnis, "On The Growth of  $\text{Al}_2\text{O}_3$  Scales," *Acta Mater.*, [61] 18 (2013) 6670-83

## *Vita*

Qian Wu [REDACTED], to Jinjiang Wu and Yihua Weng. Qian graduated from Fudan University with a Bachelor degree majoring in Optics in 2007. Then he came to Lehigh to start his Ph.D program in the department of materials science and engineering under the guidance of Professor Helen. M. Chan, Jeffery. M. Rickman and Martin P. Harmer. Upon completion of his degree, Qian plans to join the FEI Company as an application engineer focused on the FIB.